Development of a Distributed Test Architecture for Reformed Methanol HT-PEM Fuel Cell Systems

with Real-Time Integration of Simulation and HiL Modules

Johann Thorsteinsson & Malte Krusborg Kristensen

Fuel Cells and Hydrogen Technology, HYTEC4-1012, 2025-05

4th Semester Master Thesis

AAU Energy
Aalborg University
http://www.aau.dk

AALBORG UNIVERSITY
STUDENT REPORT

Title:
Development of a Distributed Test Architecture for Reformed Methanol HT-PEM Fuel Cell Systems

Theme:
Master's Thesis

Project Period:
Spring Semester 2025

Project Group:
HYTEC4-1012

Participants:
Johann Thorsteinsson
Malte Krusborg Kristensen

Supervisors:
Simon Lennart Sahlin
Vincenzo Liso

Number of Pages: 100

Date of Completion:
May 28th - 2025

Abstract:

This thesis presents the development of a distributed test architecture for reformed methanol high-temperature proton exchange membrane fuel cell (HT-PEMFC) systems, aimed at combined heat and power (CHP) applications in microgrids. The system integrates both real-time simulation and hardware-in-the-loop (HiL) components to enable modular, scalable, and realistic testing. A key contribution is the implementation of a physical methanol steam reformer test bench, which provides dynamic gas composition data to a real-time fuel cell model. The fuel cell model, developed using a gray-box approach, simulates electrical and thermal behavior and was validated against experimental data with 8.45% average relative error. A mid-level control layer coordinates the reformer, fuel cell, and thermal modules, and interfaces with a high-level energy management system (EMS). A novel gas composition control strategy was implemented to regulate CO and methanol slip by adjusting reformer temperature. Validation tests demonstrated effective gas shaping under varying flow rates. A full-system test confirmed the architecture's ability to manage dynamic loads, coordinate module behavior, and maintain safety. The results highlight the system's potential for future research in degradation analysis, remote testing, supporting the broader adoption of HT-PEMFC systems in sustainable energy applications.

Summary

This thesis presents the design, implementation, and validation of a modular, distributed test architecture for reformed methanol high-temperature proton exchange membrane fuel cell (HT-PEMFC) systems, with a focus on combined heat and power (CHP) applications in microgrids. Conducted within the framework of the FC-COGEN project, the work addresses the growing need for decentralized, efficient, and renewable energy systems capable of operating under dynamic and realistic conditions. The proposed architecture integrates both physical hardware and digital real-time models through remote communication, enabling flexible and scalable testing of advanced energy systems.

The core motivation for this research lies in the increasing complexity of modern energy systems, particularly in microgrid environments where fluctuating loads, renewable energy sources, and varying fuel qualities demand robust and adaptive control strategies. HT-PEMFCs are well-suited for such applications due to them producing sufficiently high quality thermal energy as a waste product in the production of electrical energy, tolerance to fuel impurities, and compatibility with chemical hydrides like methanol which supports liquid fuel storage solutions. However, the integration of these systems into real-world applications requires extensive testing and validation, which can be costly and time-consuming when relying solely on physical prototypes. To overcome this, the thesis introduces a distributed test architecture (DTA) that combines hardware-in-the-loop (HiL) components with real-time simulation models.

A major contribution of this work is the integration of a physical methanol steam reformer test bench into the DTA using HiL techniques. The reformer module is capable of real-time operation and provides dynamic gas composition data, which is used to inform a gray-box fuel cell model developed in MATLAB. This model simulates the electrical and thermal behavior of the fuel cell stack, including polarization characteristics, temperature dynamics, and efficiency under varying operating conditions. The model was validated against experimental data and achieved an average relative error of 8.45% in power prediction against a validation data set, demonstrating its suitability for real-time system-level simulations.

The reformer test bench was characterized through an experimental investigation, mapping the reformate gas composition across a range of feed flow rates and reformer oil temperatures. These results were used to construct lookup tables for estimating hydrogen, carbon monoxide, carbon dioxide and methanol concentrations in the reformate gas. A novel gas composition control strategy was implemented, allowing the reformer to dynamically adjust its oil temperature to minimize either carbon monoxide or methanol slip while maintaining the other below a specified threshold. Validation tests demonstrated that this strategy could effectively shape the reformate gas composition, with relative errors typically below 5% at medium to high flow rates.

To coordinate the operation of the reformer, fuel cell, and thermal integration modules, a mid-level control layer was developed in LabVIEW. This layer manages control parameters, system startup, shutdown, state transitions, and interfaces with a high-level energy man-

agement system (EMS) developed by the FC-COGEN project. The EMS provides power and heat demand profiles, which are used to drive the system under realistic residential load scenarios. The mid-level controller also includes safety features such as automatic shutdown on communication loss or gas alarm triggers, ensuring safe operation during remote or unattended testing.

A full-system validation test was conducted over a 9-hour period, involving multiple start-up and shutdown cycles, variable power loads, and real-time EMS interaction. The system successfully demonstrated coordinated operation, accurate power tracking, and effective gas composition control. The fuel cell module responded dynamically to EMS commands, while the reformer module adjusted its output to meet hydrogen demand and maintain gas quality. The hot water tank module effectively captured the thermal output of the fuel cell, simulating domestic heat integration.

In conclusion, this thesis demonstrates the feasibility and advantages of a modular, distributed test architecture for HT-PEMFC systems. By combining physical hardware with real-time simulation, the architecture enables realistic, flexible, and cost-effective testing of advanced energy systems. The work contributes valuable tools and insights to the development of sustainable microgrid technologies and lays the foundation for future research in areas such as degradation analysis, remote test bench operation, and digital twin development.

Preface

This master's thesis was written by Johann Thorsteinsson and Malte Krusborg Kristensen, members of project group HYTEC4-1012, under the supervision of Associate Professor Simon Lennart Sahlin and Associate Professor Vincenzo Liso at Aalborg University.

We would like to extend our sincere gratitude to Peilin Xie for valuable discussions regarding the FC-COGEN project and for providing access to the EMS control layer, which was essential for the integration and testing phases of this work.

Special thanks are also due to the technical staff at the AAU workshop for their assistance and support during the laboratory work, which played a crucial role in the successful implementation of the hardware-in-the-loop setup.

We are also grateful to Søren Juhl Andreasen for sharing experimental data and for insightful sparring on the startup and shutdown procedures of the prototype MSR HT-PEMFC system, which significantly informed the modeling and validation efforts in this thesis.

Their contributions and support have been instrumental in the completion of this project.

Reading Guide

The citations have been done using the Harvard method where citations will be shown as [Author(s), year]. The citations follow their references in the bibliography located at the end of the thesis. Chapters, sections, figures, tables and equations are labeled and these will also be references when mentioned in the text. The numbering of these labels is in chronological order and chapter-wise. Throughout the report, the symbols, abbreviations and subscripts can be found in the nomenclature.

The following software has been used in this project:

- Mathworks MATLAB 2024a or above
- Overleaf LaTeX
- Inkscape 1.3
- LabVIEW 2018 or above
- Spyder Python IDE
- Draw.io

Johann Thorsteinsson
jthors20@student.aau.dk

Signature: 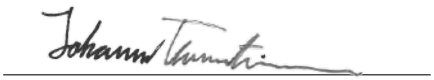

Malte Krusborg Kristensen
mkr20@student.aau.dk

Signature: 

Nomenclature

Standard SI-Units will be used

Symbol	Explanation	Unit
A	Heat Transferring Area	[m^2]
a	activity	[-]
c_p	Specific Heat Capacity at Constant Pressure	[J/(kg K)]
D_h	Hydraulic Diameter	[m]
ΔG°	Standard Gibbs free energy	[J/mol]
ΔH°	Standard Enthalpy of Reaction	[kJ/mol]
Δt	Time Step	[s]
Δt_{res}	Residence Time	[s]
E_{exc}	Activation energy of the current exchange	[J/mol]
E_{pro}	Activation energy of the proton exchange	[J/mol]
F	Faraday's Constant	[C/mol]
h	Depth	[m]
h_{conv}	Convective heat transfer coefficient	[W/(kg K)]
I	Current	[A]
i	Current Density	[A/m^2]
i_0	Exchange Current Density	[A/m^2]
i_L	Limiting Current Density	[A/m^2]
k	Conductivity of the Oil	[W/(m K)]
L	Length	[m]
LHV	Lower Heating Value	[J/kg]
M	Mass	[kg]
$\dot{m}$	Mass Flow Rate	[kg/s]
MW	Molar Weight	[kg/mol]
$\dot{n}$	Molar Flow Rate	[mol/s]
n_{cell}	Number of Cells in Stack	[-]
Nu	Nusselt number	[-]
P	Static Pressure	[Pa]
P_{FC}	Electrical power output of the fuel cell	[W]
p	Partial Pressure	[Pa]
R_{ohm}	Ohmic Resistance	[Ω]
R_u	Universal Gas Constant	[J/(mol K)]
Re	Reynolds Number	[-]
T	Temperature	[K]

Symbol	Explanation	Unit
t_{m}	Thickness of Membrane	[m]
τ	Time Constant	[s]
$\dot{V}$	Volume Flow Rate	[m^3/s]
U_{rev}	Reversible voltage	[V]
V	Voltage	[V]
w	Width	[m]
y	Molar Fraction	[-]
z	Number of transferred electrons	[-]

Greek Letters

Symbol	Explanation	Unit
α	Charge Transfer Coefficient	[-]
ϵ	Overpotential	[V]
η	Energy Efficiency	[-]
η_{FC}	Fuel cell electrical efficiency	[-]
ρ	Density	[kg/m^3]
σ_{ohm}	Electric conductivity of membrane	[S/m]

Subscripts

Symbol	**Explanation**
a	Anode
act	Activation
C	Carbon
cat	Cathode
cell	Cell
ch	Consumption
CO	Carbon Monoxide
CO2	Carbon dioxide
conc	Concentration
cons	Consumption
demand	Demand
dry	Dry Composition
FC	Fuel Cell
gen	Generated
H2	Hydrogen
H2O	Water
HWT	Hot Water Tank
in	Inlet
MeOH	Methanol
new	Next Iteration
O2	Oxygen
ohm	Ohmic
oil	Oil
out	Outlet
prod	Production
ref	Reference
sp	Setpoint
trans	Transferred

Abbreviations

Abbreviation	**Explanation**
ANFIS	Adaptive Neuro-fuzzy Inference System
APU	Auxillary Power Unit
CHP	Combined Heat and Power
DTA	Distributed Test Architecture
ECHA	European Chemical Agency
EMS	Energy Management System
GUI	Graphical User Interface
HT-PEMFC	High Temperature Proton Exchange Membrane Fuel Cell
HWT	Hot Water Tank
MSR	Methanol Steam Reforming
NDIR	Non-Dispersive Infrared
NPSV	Network-Published Shared Variables
P&ID	Piping and Instrumentation Diagram
S/C	Steam-to-Carbon
SOFC	Solid Oxide Fuel Cell
TEG	Triethylene Glycol
UML	Unified Modeling Language

Contents

List of Figures

List of Tables

Chapter 1

Introduction

The global climate crisis has proven to be one of the greatest challenges our civilization faces in the 21st century. The *International Panel on Climate Change* (IPPC) predict that an increase of the global mean temperature of more than 1.5 °C compared to pre-industrial levels will severely impact our ecosystems, increase the frequency of extreme weather phenomena and even increase the spread of vectorborne diseases, such as malaria [IPCC, 2022] [Ebi et al., 2016]. This limit therefore sets the basis for the Paris Agreements goal of keeping the increase in the global mean temperature below 1.5 °C. If the global mean temperature is to be kept under this limit, it requires many of the technologies that were previously relied on for power production and distribution to be rethought in a renewable context. One technology that is currently undergoing this rethinking is the *Combined Heat and Power* (CHP) plant, which traditionally utilized fossil fuels to produce heat and power on city scales, but are now being designed to utilize renewable fuels to provide heat and power for micro-grid systems. However, this increases the complexity of controlling the individual micro-grid systems, since the fluctuations in demand become larger relative to the mean load. As energy systems become increasingly complex, so does the interaction between components. This increases the requirement for effective energy management systems to ensure high efficiency and smooth operation and for system level testing, which is often costly if real components are used [Tripathi and Gonzalez-Longatt, 2023].

1.1 Combined Heat and Power in Micro-Grid Application

A microgrid is a small-scale electricity distribution system consisting of a number of power producers, storage and loads that can be controlled and coordinated as a whole, with either a single connection to the main grid or disconnected from the main grid [Marnay et al., 2015]. This thesis will only concern the grid connected type of microgrid. Figure 1.1 shows a representation of a grid connected microgrid.

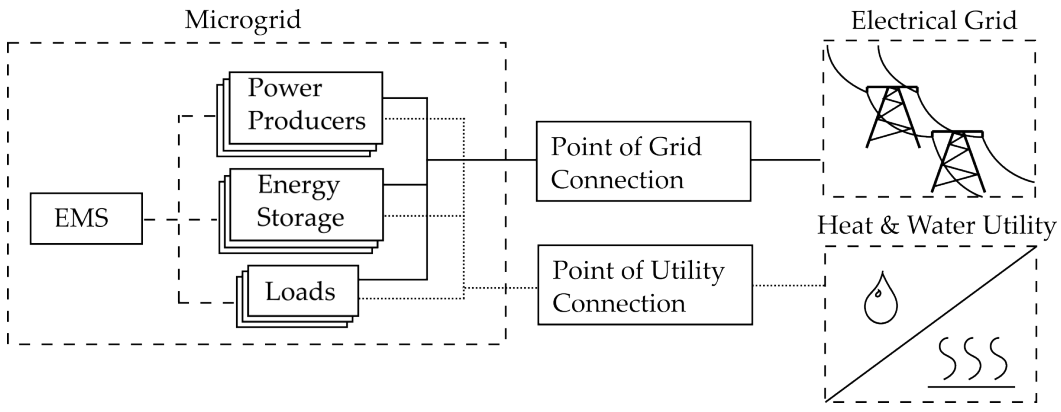

Figure 1.1: Overview of a grid connected microgrid energy system consisting of a number of power producers, energy storage units and loads, all controlled by an energy management system. The microgrid can exchange electricity and utility with the electricity and utility grids, but also internally within the microgrid.

The main advantage of a grid connected microgrid from a societal perspective is the ability to dampen the variability of load observed by the main grid, since it operates as a single coordinated unit. However, microgrids also present financial benefit to the user, since the *Energy Management System* (EMS) is able to coordinate the heat and power production, energy storage and load distribution to minimize cost of import from the grid [Marnay et al., 2015].

The power producers usually consist of a combination of photovoltaic panels, small scale wind turbines and CHP plants. CHP plants utilize waste heat from its electricity production to supply domestic heat demand. This increases the utilization of the fuel, since the heat is a byproduct of the electricity production. Traditionally CHP plants have primarily been powered by fossil fuels, such as coal, oil and natural gas, but technologies based on alternative energy sources have been considered to replace these, in order to combat the rising global temperatures. One of these technologies being *High Temperature Proton Exchange Membrane Fuel Cells* (HT-PEMFCs). While the electrical efficiency of HT-PEMFCs is usually around 40%, the total efficiency can reach 80%, and with the operating temperature of HT-PEMFCs being 150-160 °C, the waste heat is also of sufficient quality for heat integration in domestic use [Rosli et al., 2017]. Another major advantage of HT-PEMFCs is the ability to use impure hydrogen sources, which would typically harm low temperature PEMFCs. This allows for using a wider range of fuels to power the HT-PEMFC, such as chemical hydrides.

1.2 Chemical Hydrides

Chemical hydrides refer to the storage of hydrogen in chemical compounds. One of the major obstacles for large scale utilization of hydrogen is its low energy density, despite it having at large *Higher Heating Value* (HHV). This leads to pure hydrogen either being stored at pressures of up to 900 bar or as liquid at 20 K [Niaz et al., 2015]. The energy density of chemical hydrides are often much higher than either compressed hydrogen or liquid hydrogen, which simplifies the storage and transportation of hydrogen. The tradeoff for this are more complex systems requiring chemical reactors for the hydrogenation and dehydrogenation processes and efficiency losses in the same processes.

Three of the most common chemical hydrides are methane, ammonia and methanol. Key physical properties of these and of hydrogen are shown in Table 1.1.

Table 1.1: Key physical properties of hydrogen, methane, methanol and ammonia for energy storage [Zamfirescu and Dincer, 2009] [Herdem et al., 2018] [Valera-Medina et al., 2018] [NIST, 2025].

Property	Unit	Pressure [bar]	Hydrogen	Methane	Methanol	Ammonia
Boiling Point	[K]	1	21	112	338	239
LHV	[MJ/kg]	-	120	50	19.9	-
HHV	[MJ/kg]	-	142	55.5	23	22.5
Volumetric Density	[kg/m^3]	1	0.09	0.668	792	0.73
		10	7.87	79.2	800	610
		600	115	296	856	651
Energy Density	[MJ/m^3]	1	1.28	37.1	18200	16.4
		10	117	410	-	13700
		600	681	16500	-	-

Of the four chemicals present in Table 1.1, only methanol is liquid at *Standard Temperature and Pressure* (STP), which results in a very large energy density compared to the others at atmospheric pressure. Ammonia turns to liquid at 8.5 bar at 20 °C, which means that it can be stored as a liquid at relatively low pressure, However the energy density is still lower than that of methanol. The HHV of the two are similar, but the methanol has once again a slightly larger higher heating value. The largest HHV is observed for pure hydrogen, but due to the low volumetric density the energy density is the lowest of the four. It should be noted that both methanol and ammonia are toxic, with recommended exposure limits set by the *European Chemicals Agency* (ECHA) being 200 ppm and 20 ppm respectively across an 8 hour period [ECHA, 2025]. This sets strict safety requirements for any system that utilize them, which are not necessary for methane or pure hydrogen. However, if handled professionally, these limits are not difficult to comply with, while high pressure storage in itself carry strict safety requirements. Overall the methanol seems to be the most interesting chemical hydride for large scale hydrogen storage, and will therefore be the subject of investigation of this report.

1.3 Fuel Cell Mechanisms

Fuel cells generate electricity through an electrochemical reaction between hydrogen and oxygen, with water and heat as byproducts. This reaction provides clean and efficient power, making fuel cells suitable for applications where both electrical and thermal outputs are valuable.

At the core of a fuel cell is an electrolyte membrane sandwiched between two electrodes: the anode and the cathode. Hydrogen gas is supplied to the anode, where it is split into protons and electrons. The protons pass through the electrolyte membrane to the cathode, while the electrons are forced to travel through an external circuit, generating electricity. At the cathode, the electrons recombine with the protons and oxygen to form water:

$$\begin{aligned}
\text{Anode:} \quad & H_2 \rightarrow 2H^+ + 2e^- \\
\text{Cathode:} \quad & \frac{1}{2}O_2 + 2H^+ + 2e^- \rightarrow H_2O \\
\text{Overall:} \quad & H_2 + \frac{1}{2}O_2 \rightarrow H_2O + \text{electricity} + \text{heat}
\end{aligned}$$

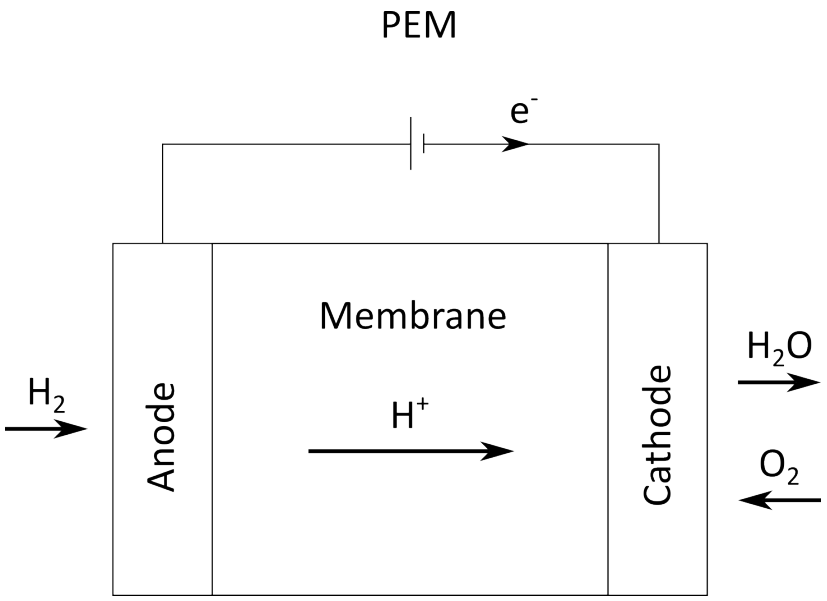

Figure 1.2: Illustration of an individual fuel cell. Inspired by [Sebbahi et al., 2022]

.

To increase the power output of a fuel cell, one approach is to enlarge the active area of the cell. A larger active area provides more surface for electrochemical reactions to occur, thereby allowing more hydrogen to be oxidized and more electrons to flow—resulting in a higher current output. However, increasing the cell area eventually becomes impractical due to constraints in size, cost, and system complexity. A more scalable alternative is to connect multiple cells in series to form a fuel cell stack, which increases the total voltage output. Since each individual cell typically produces less than 1 V under open-circuit conditions, stacking enables the system to reach voltage levels suitable for practical applications [Zhang et al., 2006].

As the current density increases during operation, the voltage output of each cell decreases due to internal losses. At low current densities, activation losses dominate; these are associated with the energy barrier that must be overcome for the electrochemical reactions to proceed. As current increases, ohmic losses become more significant, resulting from resistance to ion transport through the electrolyte and electron flow through the electrodes. At high current densities, concentration losses emerge due to limitations in the supply of reactants and the removal of products at the reaction sites. These combined effects are illustrated in the polarization curve shown in Figure 1.3, where each region reflects the influence of a different loss mechanism on the cell's performance. [Larminie and Dicks, 2003].

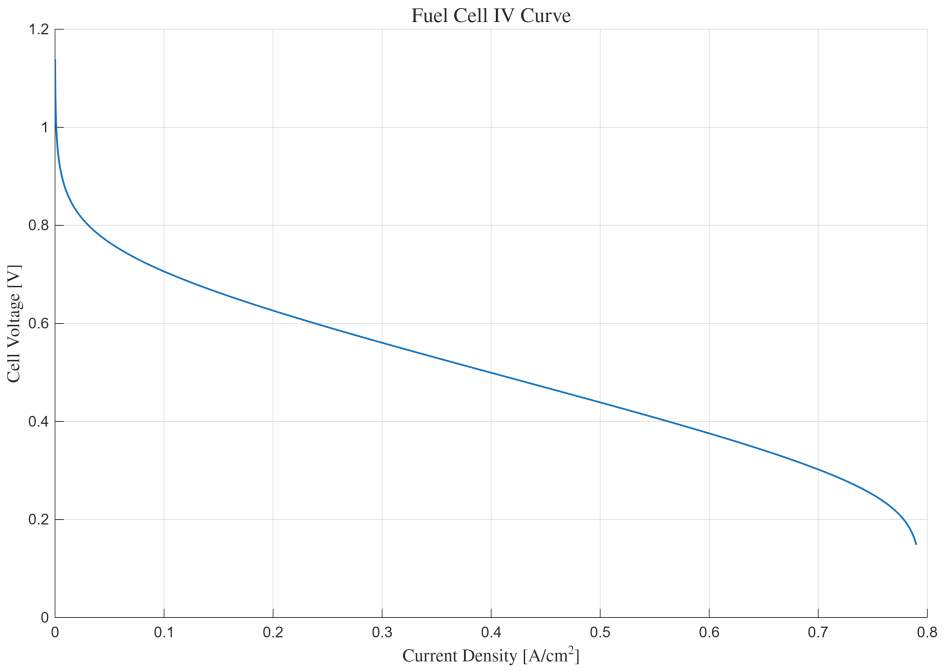

Figure 1.3: Typical polarization curve of a fuel cell, illustrating the voltage drop associated with activation losses (low current density), ohmic losses (intermediate range), and concentration losses (high current density).

Although HT-PEMFCs are more resilient to fuel impurities compared to their low-temperature counterparts, they are not immune to performance degradation caused by contaminants such as CO and methanol slip. These substances can still temporarily poison the anode catalyst, especially under dynamic conditions like frequent start-ups or fluctuating load demands. While the elevated operating temperature of HT-PEMFCs (typically above 160°) allows for better CO tolerance, prolonged exposure or high concentrations can reduce overall system efficiency and catalyst durability. Therefore, careful control of the reformate gas composition—particularly with respect to CO and unconverted methanol—is essential for maintaining long-term stability and achieving optimal fuel cell performance. [Araya, 2012], [Xu et al., 2023].

1.4 Reformed Methanol In HT-PEMFC Systems

As previously mentioned, HT-PEM fuel cell systems exhibit a higher tolerance to impurities in the fuel stream compared to their low-temperature counterparts. This characteristic allows the use of methanol as a practical hydrogen carrier. To supply the required hydrogen to the fuel cell, methanol can undergo various reforming processes, including steam reforming, partial oxidation, and auto-thermal reforming. Among these, steam reforming is particularly well-suited for HT-PEM applications. It involves reacting methanol with steam over a catalyst—typically $Cu/ZnO/Al_2O_3$—at temperatures around 200–300 °C to produce a hydrogen-rich reformate gas. This method offers a high hydrogen yield and relatively low CO concentrations, typically within the tolerance range of HT-PEM fuel cells, making it ideal for integration. Although steam reforming is endothermic and requires external heat, the elevated operating temperature of HT-PEM systems facilitates thermal integration.

In contrast, partial oxidation, where methanol reacts with a limited amount of oxygen, is exothermic and allows for faster thermal start-up. However, it generally results in lower hydrogen yields and significantly higher CO concentrations, which can still lead to degradation over time, even in HT-PEM cells. Auto-thermal reforming, which combines both steam reforming and partial oxidation, offers thermal balance and a more compact reactor design but introduces complexity in terms of control and CO management. [Behrens and Armbrüster, 2012]

Due to these trade-offs, steam reforming is employed in this work as the preferred hydrogen generation method, striking an effective balance between hydrogen output, gas purity, and compatibility with the thermal characteristics of HT-PEM systems. The primary chemical reactions governing methanol steam reforming are as follows:

$$\begin{aligned}
\text{Methanol Steam Reforming:} &\quad \mathrm{CH_3OH + H_2O \rightarrow CO_2 + 3H_2} \quad \Delta H^\circ = +49\ \mathrm{kJ/mol} \\
\text{Methanol Decomposition:} &\quad \mathrm{CH_3OH \rightarrow CO + 2H_2} \quad \Delta H^\circ = +90\ \mathrm{kJ/mol} \\
\text{Water-Gas Shift Reaction:} &\quad \mathrm{CO + H_2O \rightarrow CO_2 + H_2} \quad \Delta H^\circ = -41\ \mathrm{kJ/mol}
\end{aligned}$$

The main reaction driving process is the methanol steam reforming reaction, but due to the high temperature needed for the process of around 180 to 300 °C some of the methanol degrades into CO as shown in the methanol decomposition reaction. Due to the presence of water, some of this CO is converted back into H_2 by the water gas shift reaction. The extent to which each of these reactions proceeds depends on several factors: the operating temperature of the reformer, the total feed flow rate, the *Steam-to-Carbon* (S/C) ratio in the methanol-water mixture, the catalytic surface area available for reaction, and the degree of catalyst degradation over time. Consequently, these parameters play a critical role in shaping the composition of the reformate gas and the overall efficiency and reliability of the reforming process. [Yoon et al., 2007] Managing the gas composition is essential for maintaining fuel cell performance and preventing degradation, particularly with respect to CO and methanol exposure. [Holladay et al., 2009]

Figure 1.4 illustrates a typical integration of a methanol steam reformer with a high-temperature PEM fuel cell stack.

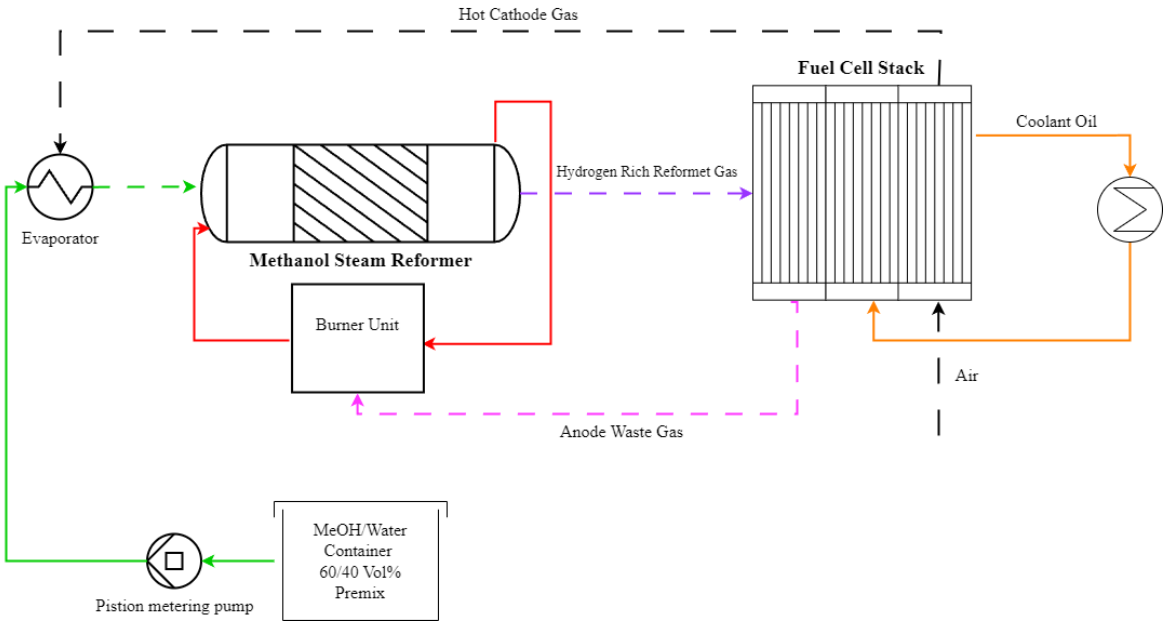

Figure 1.4: Conceptual diagram based on a Ph.d. by [Justesen, 2015], illustrating the integration of a methanol steam reformer with a high-temperature PEM fuel cell stack. The system features partial thermal integration to improve overall efficiency: waste heat from the fuel cell cathode can be used to assist in methanol/water evaporation, while the anode off-gas is routed to a burner unit to supply the heat required for the endothermic steam reforming process.

Figure 1.4 illustrates a conceptual layout of a methanol reforming fuel cell system with potential for further heat integration. While simplified, it highlights the key components and energy flows in such a system. In this configuration, the waste heat from the fuel cell's cathode air stream is recovered and used to preheat and evaporate the methanol–water mixture before it enters the reformer. Additionally, the anode waste gas containing unreacted hydrogen, is combusted to supply thermal energy to the reformer itself. This approach to integrated heat management improves overall system efficiency. A system of this kind was proposed as early as the 1970s by [Kurpit, 1975]. In modern implementations, the fuel cell stack can be cooled using a thermal oil loop operating at around 160 °C. The recovered heat can then be redirected for use in domestic or industrial heating applications, supporting the concept of CHP.

1.5 State of the Art

This section presents an overview of the state of research for HT-PEM fuel cell systems and methanol reformers in a micro-CHP context.

1.5.1 Fuel Cells in Micro-CHP

The usage of HT-PEMFC systems shows promise in stationary applications such as micro-CHP systems due to their ability to provide steady power as a substitute for a fossil fuel based generator especially when proper heat management and integration is incorporated.

Such a system was explored by [Arsalis et al., 2011], where a 1 kW HT-PEMFC-based micro-CHP unit is evaluated under a Danish residential load profile. This study develops

a comprehensive model incorporating all major balance-of-plant components, including a steam methane reformer, water-gas shift reactor, heat exchangers, and a fuel cell stack, interconnected through simulations in LabVIEW to enable potential *Hardware-in-the-Loop* (HiL) expansion. Taken together, the findings of Arsalis et al. provide strong support for the development of compact, efficient HT-PEMFC micro-CHP systems. They further reinforce the relevance of using simulation environments capable of real-time synchronization and hardware interfacing.

A study by [Zhao et al., 2022] furthers the research by implementing a HT-PEM system in a combined cooling, heating and power system and using a methanol steam reformer subsystem as a fuel processing plant. Extending the research into the potential of using methanol as a hydrogen carrier.

1.5.2 Methanol Steam Reformer Modeling

Most research into utilizing methanol steam reforming is conducted using theoretical modeling or semi-empirical techniques to simplify the examination and control of a full system. For the modeling of methanol steam reformers the reaction mechanisms are expressed using reaction rates. A study done by [Sá et al., 2011] compared different methanol steam reforming and reverse water gas shift kinetic rate models developed by different authors to experimental data in order to categorize the accuracy. The result of the comparison showed that a kinetic Langmuir–Hinshelwood model proposed by [Peppley et al., 1999] was the overall best fit.

Modeling methanol steam reformers through first-principles or semi-empirical methods often requires detailed knowledge of chemical kinetics, reactor geometry, catalyst behavior, and thermal integration. These models typically involve numerous assumptions and simplifications. However, the reforming process is inherently nonlinear and sensitive to operational variables such as temperature gradients, catalyst degradation, and fluctuating feed conditions, which are difficult to capture in detail with theoretical based models.

A paper by [Justesen et al., 2013] highlights this challenge, stating that while first-principle or semi-empirical models can provide theoretical insight, they often fail to accurately reflect transient behavior or degradation effects under dynamic operating conditions. In response, their work demonstrates the successful application of data-driven black box methods such as Adaptive Neuro-Fuzzy Inference Systems, which utilize empirical data to model the reformer's dynamic response and enable better control under real-world scenarios.

Nevertheless, while black-box models provide useful abstractions, they still rely heavily on the quality and coverage of training data, and do not inherently incorporate real-world uncertainties or unmodeled dynamics. This is where HiL simulation offers a robust alternative. By combining physical reformer test benches with digital simulation environments, HiL systems allow for the real-time emulation of reformer behavior under varying load and environmental conditions.

1.5.3 Hardware-in-the-Loop Application

The application of HiL simulation in energy systems has grown significantly as the demand for robust and flexible validation environments increases. While HiL techniques have long been employed in sectors such as aerospace and automotive engineering, their adoption in the energy sector, particularly CHP systems, has gained momentum only more recently.

A contribution to this field is presented by [El-Baz et al., 2015], who demonstrate the use of a HiL simulation system for a residential Stirling-engine-based micro-CHP setup. Their testbed integrates real hardware, comprising a heat storage unit and domestic hot water emulation, with a digital building model implemented in Modelica (SimulationX), connected through MATLAB and LabVIEW. This architecture allows for synchronized real-time data exchange, enabling full-system validation under representative environmental and demand conditions.

In addition to research on HT-PEMFC systems in mobile and stationary applications, there are several noteworthy demonstrations of HiL integration for fuel-reforming-based fuel cell systems. A notable example is presented by [Rechberger et al., 2009], who developed a 7 kW *Solid Oxide Fuel Cell* (SOFC) Auxiliary Power Unit (APU) for maritime applications. Their system utilized a methanol reformer employing a catalytic methanation process to generate a hydrogen-rich gas mixture containing methane, which supported internal reforming within the SOFC stack. A key innovation of this project was the integration of a real-time control system using a HiL architecture, interfaced via CAN bus with the test bench automation. This setup enabled dynamic validation of fully automated control states, including start-up, ramp-up, operation, and shutdown sequences. The project demonstrated the effectiveness of combining real hardware with control-oriented simulation to facilitate robust testing and system validation.

A further significant contribution to the field of fuel cell HiL integration is presented by Fröjd et al.[Fröjd et al., 2014], who developed a real-time capable model of a diesel-based fuel processor for a truck APU system. The model was designed for HiL testing of the programmable logic controller responsible for managing the start-up and operational logic of a PEM fuel cell system. Implemented in Modelica and simulated using Dymola, the model included over 25 dynamic components—such as an autothermal reformer, water-gas shift reactor, and preferential oxidizer with simplifications to ensure stability and real-time performance. A particular focus was placed on simulating the start-up phase, which is highly dynamic and critical for fuel processor reliability. This work highlights the importance of realistic real-time simulations for verifying control strategies before system assembly.

1.6 Distributed Test Architecture and Hardware-in-the-Loop

Research into the development and implementation of HT-PEMFC systems for CHP applications in microgrids remains an active and evolving field. Despite their potential for high efficiency, low emissions, and fuel flexibility, HT-PEMFC-based systems face significant technical and integration challenges—particularly when deployed in dynamic real-world environments such as residential or industrial microgrids.

To support the advancement of these technologies, this project integrates HiL into a *Distributed Test Architecture* (DTA). HiL enables physical system components to interact with real-time simulation environments. By using a physical component, complex dynamics such as thermodynamics, heat transfer, fluid mechanics and chemical reactions, do not need to be simulated using models, that are often too simple to accurately capture these dynamics. HiL therefore enables more accurate system modeling and early validation of control algorithms and hardware integration strategies [Tripathi and Gonzalez-Longatt, 2023]. The use of HiL enables real-time testing and validation of physical subsystems within a simulated or partially physical system environment, facilitating safe and cost-effective experimentation under realistic operating conditions. DTA refers to the interconnection of physical devices—such as sensors, actuators, and embedded systems—with digital infrastructure through standardized communication protocols. This project seeks to create a DTA, where each system component can operate independently, exchange data, and receive control signals in real time. The DTA provides the networking framework that allows distributed test benches and control systems to communicate flexibly and reliably, mimicking the decentralized nature of future energy systems. Together, HiL and DTA form the basis for a modular and remotely accessible system framework that supports research and development in HT-PEM fuel cell integration and the evaluation of EMS strategies in micro-CHP contexts.

1.7 Integration with Existing Research Project

This project builds upon the ongoing research initiative FC-COGEN, which aims to demonstrate an e-methanol-based fuel cell system for CHP applications. The system is targeted at both residential and industrial use cases with the goal of reducing dependency on conventional power grid infrastructure [EUDP, 2025]. In the following sections, the FC-COGEN project will first be introduced, followed by a summary of prior work on a predictive EMS developed in as part of the FC-COGEN project. The subsequent sections outline the specific objectives and contributions of this thesis—particularly in HiL integration, simulation complexity, and DTA design, which are applicable beyond the scope of FC-COGEN and contribute to the general advancement of HT-PEMFC system testing and validation.

1.7.1 FC-COGEN

This project is carried out in the context of the FC-COGEN initiative, a Danish research and development effort led by Aalborg University in collaboration with Blue World Technology and other industrial partners. The FC-COGEN project aims to develop and demonstrate a 20 kW methanol-based micro-CHP system utilizing HT-PEMFC technology. The system is intended for both off-grid and on-grid residential and industrial applications, with the broader goal of replacing fossil-fuel-based combustion engines. As part of this ecosystem, our work focuses on the digital integration of experimental test benches into an DTA-based monitoring and control framework to support the validation and optimization of such energy systems [EUDP, 2025].

1.7.2 Existing Electrical Management System

A closely related component of the FC-COGEN research initiative is the development of a two-layer EMS by [Xie et al., 2025], designed for HT-PEMFC-based micro-CHP systems operating in residential environments. The EMS framework addresses both the economic and operational challenges associated with integrating methanol-reformed fuel cells into modern household energy systems. It does so by coupling long-term predictive control with real-time load balancing strategies.

The upper layer of the EMS employs a day-ahead optimization algorithm that forecasts household electricity and heat demand alongside dynamic electricity pricing. Based on these forecasts, it generates hourly operational schedules for the fuel cell and other energy sources (e.g., the grid or battery). The objective is to minimize total operational costs, including both methanol and electricity expenditures. This allows the system to strategically activate the fuel cell during price peaks or high heat demand, ensuring economical operation and efficient resource use.

The lower layer consists of a decentralized control system that executes the schedule from the upper EMS. It handles real-time decisions regarding energy dispatch by monitoring DC bus voltage and battery state-of-charge. In this structure, the fuel cell strictly follows the upper-layer on/off commands and adjusts power output according to reference values, but with flexibility to deviate slightly based on instantaneous load conditions. The system is also robust enough to operate in an unsupervised mode when forecast data are unavailable, relying only on real-time signals.

Figure 1.5 is an illustration from the paper by [Xie et al., 2025] showing an overview of the system designed for a residential microgrid application.

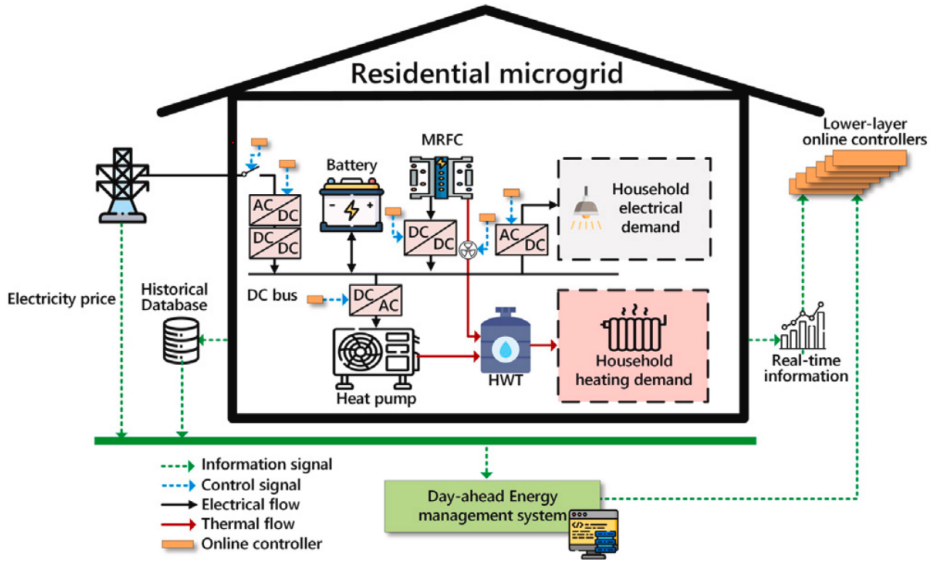

Figure 1.5: Graphical abstract for paper by [Xie et al., 2025]

1.7.3 Project Contribution

The principal scientific contribution of this project is the experimental integration of a physical, HiL-based methanol steam reformer test bench into a predictive EMS framework for a HT-PEMFC CHP system. While prior research, has focused on simulation-based or empirical black-box modeling of reformer-fuel cell integration, this project aims to replace the reformer simulation with a real, instrumented test bench capable of delivering dynamic gas composition data in real time. This HiL-based reformer module allows for experimental validation of EMS strategies under realistic and time-varying operational conditions, bridging the gap between model-based EMS design and deployment on physical systems. The reformer output, comprising H_2, CO, CO_2, and methanol slip, is measured continuously and used to inform a real-time fuel cell model.

Additionally to the HiL-based reformer module a grey-box based fuel cell module operating in real-time is developed. The integration is structured through a modular architecture. Each module, the reformer, fuel cell, and heat integration, is independently developed and capable of real-time operation. The reformer module includes both a predictive model for feed flow control and the actual hardware that produces the reformate gas. When a H_2 demand is received from the EMS layer, the reformer module adjusts its input accordingly and reports the actual gas composition, which is then used by the fuel cell module to simulate power and heat generation in real-time.

The system receives commands from the EMS layer developed by [Xie et al., 2025] for the FC-COGEN project. These include:

- On/Off control signals for system activation,
- Power reference values (P_{Ref}),
- Heat demand profiles for residential use.

These commands are passed through a mid-level coordination layer, implemented in LabVIEW, which manages startup, shutdown, and state transitions across all physical and digital modules.

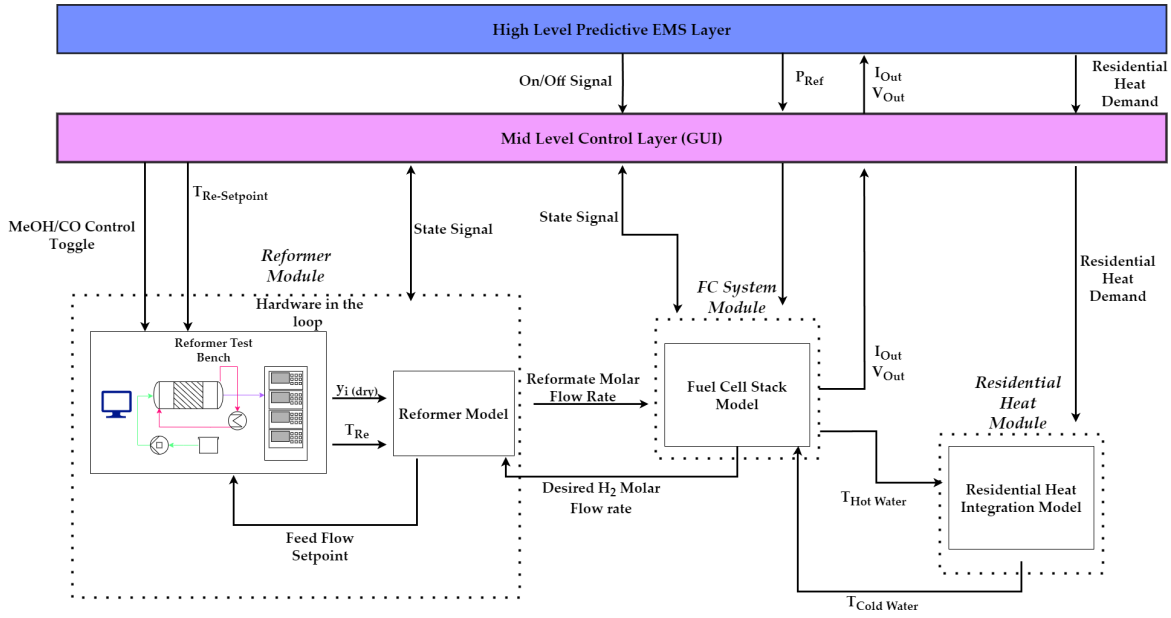

Figure 1.6: Illustration of the communication lines between the modular systems and control levels.

Figure 1.6 illustrates this modular control structure and information flow. Each dotted box in the figure represents a self-contained module, capable of independent execution, and the arrows represent the continuous data exchange enabling real-time coordination between modules and the EMS. A larger version is available in Appendix C

Chapter 2

Thesis Statement

Microgrids present a step towards the elimination of reliance on fossil fuels by decentralizing energy production and control by improving the utilization of energy and reducing the stress on an already challenged main grid. This is done by monitoring the electricity and fuel prices, in order to determine when to draw energy from the grid and when to produce energy locally, when to store energy in batteries and thermal storage and when to offset heat and power loads. Microgrids benefit from the use of combined heat and power plants, since the heat produced during electricity production can be used to cover the heat demand of the microgrid. *High-Temperature Proton Exchange Membrane fuel cells* (HT-PEMFC) are useful in this context being able to produce high quality waste heat and use chemical hydrides, such as methanol, as fuels. This thesis aims to develop a modular, distributed test architecture for a *Methanol Steam Reformer* (MSR) HT-PEMFC system. The architecture combines model-based and hardware-based modules via real-time communication channels to facilitate testing and system development. A physical methanol steam reformer test bench is integrated using *Hardware-in-the-Loop* (HiL) to provide realistic dynamic temperature and gas composition data, which in turn delivers hydrogen to a simulated fuel cell module. This modular framework supports system-level validation and gas quality control.

This leads to the following research questions:

- *How can a high-temperature proton exchange membrane fuel cell be modeled to predict the dynamic behavior of the fuel cell in terms of power output, heat generation and temperature dynamics in a CHP application?*
- *How can a reformer test bench can be integrated as Hardware-in-the-Loop in a distributed real-time test architecture to enable realistic, dynamic interaction with simulation models?*
- *To what extend can the gas composition of a methanol reformer be shaped in real time through temperature control, and how effective is this approach in meeting target impurity constraints for CO and methanol slip?*

2.1 Methodology

To support the development and validation of a HT-PEMFC system for CHP applications, a modular approach is adopted. Each major subsystem, including the reformer, the fuel cell stack and the residential heat integration, is developed as independent modules capable of real-time operation and remote interconnectivity. An overview of the system configuration is illustrated in.

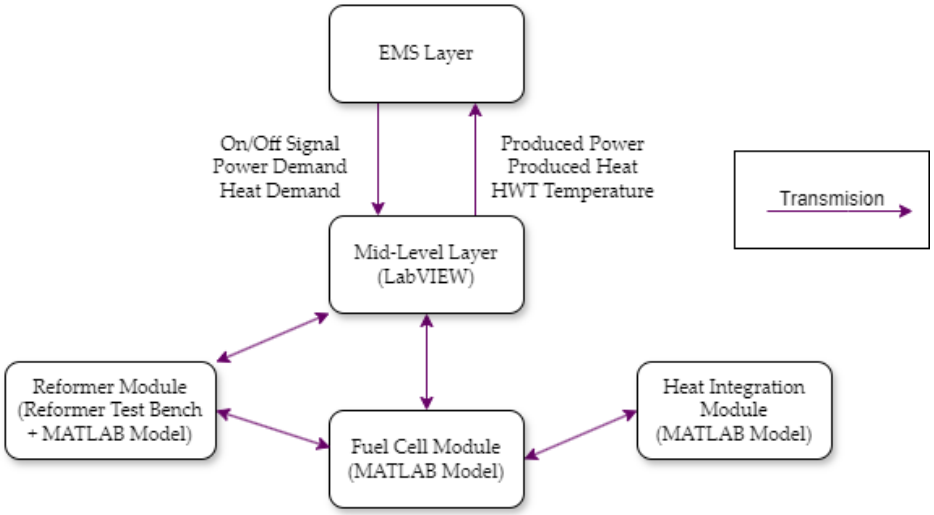

Figure 2.1: Simplified overview of the modular control and communication architecture. Each module operates semi-independently and is coordinated by a mid-level LabVIEW interface. The system receives real-time commands from an upper-level EMS layer and adjusts operational parameters accordingly.

The reformer module consists of a physical test bench integrated as HiL and a real time model. The model performs two functions, it estimates the required feed flow rate based on the hydrogen demand from the fuel cell module and the current reformer temperature, and it calculates the molar flow rates of the reformate gas components using real-time gas composition measurements from the test bench. A module containing a gray-box model of the HT-PEM fuel cell stack is developed in MATLAB and operates in real time. The fuel cell module receives reformate gas data from the reformer module and outputs electrical and thermal power based on demands from an EMS layer. The hot water module serves as the residential heat integration solution. It calculates the resulting water temperature by accounting for both the thermal output from the fuel cell module and the varying residential heat demand.

A mid-level control layer, developed in LabVIEW, acts as the system's coordination hub, receiving all transmissions and managing state transitions between modules, making sure that all components are ready before changing state. Additionally it acts as a graphical user interface for monitoring the modules and configuring control variables. It also receives the commands from the higher-level EMS layer developed by [Xie et al., 2025] and distributes them to the relevant modules.

Based on characterization experiments on the reformate gas a control algorithm is developed and validated that enables the reformer module to predict and adjust the concentra-

tions of CO and methanol slip dynamically based on current operation point by varying reformer temperature.

Finally, the full system is tested under real-time dynamic conditions, including variations in electrical power demand, cyclic on/off operation, and different gas composition control scenarios. The reformer, fuel cell and thermal integration modules coordinates in real-time to meet the demands set by the higher-level EMS layer.

Chapter 3

Theory & Modeling

3.1 Fuel Cell

This section explains the model used for the fuel cell. The model takes the reference signal for the power, the molar flow rate and fraction of hydrogen and the temperature of the fuel cell and outputs the current and voltage of the fuel cell, so that the power output of the fuel cell stack matches the power reference signal. The model is dynamic with the temperature, taking into account the heat capacity of the fuel cell stack, the heat produced during operation and the heat transfer with the oil loop. This allows for investigation of how the dynamics of the oil cooling loop affects the operation of the fuel as well as investigating start up and shutdown procedures.

3.1.1 Polarization curve

The modeling of the polarization curve of the fuel is a gray-box model of the reversible voltage and overpotentials of the fuel cell. The gray-box is later fitted using a dataset of a load cycling test of the fuel cell stack done as part of the MFC Multigen project [Li et al., 2023].

The cell voltage a fuel cell produces is a function of the reversible voltage and the overpotentials, with the reversible voltage being the highest theoretical voltage a fuel cell can produce and the overpotentials being nonidealities causing the voltage to decrease. The resulting cell voltage is described in (3.1).

$$V_{\text{cell}} = U_{\text{rev}} - \epsilon_{\text{act}} - \epsilon_{\text{ohm}} - \epsilon_{\text{conc}} \quad [\text{V}] \tag{3.1}$$

- V_{cell}: Cell Voltage [V]
- U_{rev}: Reversible voltage [V]
- ϵ_{act}: Activation overpotential [V]
- ϵ_{ohm}: Ohmic overpotential [V]
- ϵ_{conc}: Concentration overpotential [V]

The reversible voltage is the ideal voltage the electrochemical reaction of the fuel cell can produce. The reversible voltage is described by the Nernst Equation as shown in (3.2) [Khotseng, 2019].

$$U_{\text{rev}} = -\frac{\Delta G^{\circ}}{z\ F} - \frac{R_{\text{u}}\ T}{z\ F}\ ln\left(\frac{a_{\text{H2O}}}{a_{\text{H2}}\ {a_{\text{O2}}}^{1/2}}\right) \quad [\text{V}] \tag{3.2}$$

- U_{rev}: Reversible voltage [V]

- ΔG°: Standard Gibb's free energy [J/mol]
- z: Number of transferred electrons [-]
- F: Faraday's constant [C/mol]
- R_{u}: Universal gas constant [J/(mol K)]
- a_{H2O}: Activity of water [-]
- a_{H2}: Activity of hydrogen [-]
- a_{O2}: Activity of oxygen [-]

The first term of Equation (3.2) describes the reversible voltage at standard conditions, while the second term corrects for changes in temperature, pressure and the composition of reactants and products. The electrochemical reaction in the fuel cell has a standard Gibb's free energy ΔG° = -228.6 kJ/mol. For gasses, the activity is approximately equal to the ratio of the partial pressure of the gas to the standard pressure, with the standard pressure being atmospheric pressure [Khotseng, 2019]. Thus Equation (3.2) can be written as Equation (3.3).

$$U_{\mathrm{rev}} = -\frac{\Delta G}{z\ F} - \frac{R_{\mathrm{u}}\ T}{z\ F}\ ln\left(\frac{\frac{p_{\mathrm{H2O}}}{p^{\circ}}}{\frac{p_{\mathrm{H2}}}{p^{\circ}}\ \left(\frac{p_{\mathrm{O2}}}{p^{\circ}}\right)^{1/2}}\right) \quad [\mathrm{V}] \tag{3.3}$$

- p_{H2O}: Partial pressure of water [Pa]
- p_{H2}: Partial pressure of hydrogen [Pa]
- p_{O2}: Partial pressure of oxygen [Pa]
- p°: Standard pressure [Pa]

The partial pressure of hydrogen is calculated at the inlet of the anode, the partial pressure of the oxygen is calculated at the inlet of the cathode and the partial pressure of water is calculated at the outlet of the cathode. It is assumed that there is constant pressure along the anode and cathode channels. The partial pressure of each component is the product of the molar fraction and pressure, as shown in Equation (3.4).

$$p_j = y_j\ P_k \quad [\mathrm{Pa}] \tag{3.4}$$

- p_j: Partial pressure of component j [Pa]
- y_j: Molar fraction of component j [-]
- P_k: Pressure of either anode or cathode [Pa]

The molar fraction of oxygen is simply 21%. The molar fraction of hydrogen is assumed to be 68% for the experimental fitting. The molar fraction of water is calculated based on the water produced in the cathode. The molar rate of hydrogen consumption is described using the Faraday equation, as shown in Equation (3.5).

$$\dot{n}_{\mathrm{H2,cons}} = \frac{I_{\mathrm{FC}}\ n_{\mathrm{cell}}}{2\ F} \quad \left[\frac{\mathrm{mol}}{\mathrm{s}}\right] \tag{3.5}$$

- $\dot{n}_{\text{H2,cons}}$: Molar rate of hydrogen consumption [mol/s]
- I_{FC}: Fuel cell stack current [A]
- n_{cell}: number of cells [-]
- F: Faraday's constant [C/mol]

Since water contains 2 hydrogen atoms, the molar rate of water production is equal to the molar rate of consumption of hydrogen. The molar fraction of water is calculated using Equation (3.6)

$$y_{\text{H2O}} = \frac{\dot{n}_{\text{H2O,prod}}}{\dot{n}_{\text{O2,in}} - \frac{1}{2}\dot{n}_{\text{H2,cons}} + \dot{n}_{\text{N2,in}} + \dot{n}_{\text{H2O,prod}}} \quad [-] \tag{3.6}$$

- y_{H2O}: Molar fraction of water exiting the cathode [mol/s]
- $\dot{n}_{\text{H2O,prod}}$: Molar rate of water production [mol/s]
- $\dot{n}_{\text{O2,in}}$: Molar flow rate of oxygen entering the cathode [mol/s]
- $\dot{n}_{\text{N2,in}}$: Molar flow rate of nitrogen entering the cathode [mol/s]

The denominator in Equation (3.6) is the total molar flow rate of gases leaving the cathode. The first two terms in the equation take into account the consumption of oxygen in the fuel cell reaction, while the molar flow rate of nitrogen is constant and the molar flow of water is the produced water in the fuel cell reaction.

The overpotentials are three different voltage losses that occur under the fuel cell reaction and thus constitute efficiency losses. These voltage losses are the activation overpotential, the ohmic overpotential and the concentration overpotential. The activation over potential is caused by the activation energy the reaction has to overcome in order to occur. The activation overpotential has a logarithmic relation with the current density of the fuel cell, as described by the Tafel equation shown in Equation (3.7) [O'Hayre, 2016].

$$\epsilon_{act} = \frac{R_{\text{u}}\ T}{\alpha_{\text{act}}\ z\ F}\ ln\left(\frac{i}{i_0}\right) \quad [\text{V}] \tag{3.7}$$

- ϵ_{act}: Activation overpotential [V]
- α_{act}: Charge transfer coefficient [-]
- i: Current density [A/m^2]
- i_0: Exchange current density [A/m^2]

The current density is the current per cross-sectional area of the membrane. The relation between between the activation overpotential and current density causes the activation overpotential to be dominant at low current densities. The charge transfer coefficient is usually assumed to be α_{act} = 0.5 [García-Valverde et al., 2012]. The exchange current density is temperature dependent. This dependency is described by the Arrhenius equation as shown in Equation (3.8) [García-Valverde et al., 2012].

$$i_0 = i_{0,\text{ref}}\ e^{-\frac{E_{\text{exc}}}{R_{\text{u}}}\left(\frac{1}{T}-\frac{1}{T_{\text{ref}}}\right)} \quad \left[\frac{\text{A}}{\text{m}^2}\right] \tag{3.8}$$

- $i_{0,\text{ref}}$: Reference exchange current density [A/m^2]
- E_{exc}: Activation energy of the current exchange [J/mol]
- T_{ref}: Reference Temperature [K]

The reference temperature for the model is chosen to be 433 K, since this is a common operating temperature of a HT-PEMFC [Xie et al., 2025]. The ohmic overpotential is caused by the electrical resistance of the membrane, which means that there is a proportional relationship between the ohmic overpotential and the current density as shown in Equation (3.9) [O'Hayre, 2016].

$$\epsilon_{\text{ohm}} = \frac{t_{\text{m}}}{\sigma_{\text{ohm}}}\, i \quad [\text{V}] \tag{3.9}$$

- ϵ_{ohm}: Ohmic overpotential [V]
- t_{m}: Thickness of membrane [m]
- σ_{ohm}: Electric conductivity of membrane [S/m]

The proportional relation between the ohmic overpotential and the current density cause the ohmic overpotential to be dominant at intermediate current densities and it is therefore the dominant voltage loss at the current densities most commonly used operating the fuel cell. The electric conductivity of the membrane is also temperature dependent. This dependency is also described using the Arrhenius equation as shown in Equation (3.10) [García-Valverde et al., 2012].

$$\sigma_{\text{ohm}} = \sigma_{\text{ohm,ref}}\, e^{-\frac{E_{\text{pro}}}{R_{\text{u}}}\left(\frac{1}{T}-\frac{1}{T_{\text{ref}}}\right)} \quad \left[\frac{\text{S}}{m}\right] \tag{3.10}$$

- $\Omega_{0,\text{ref}}$: Reference electric conductivity of membrane [S/m]
- E_{pro}: Activation energy of the proton exchange [J/mol]
- T_{ref}: Reference temperature [K]

The concentration overpotential is caused by build-up of products on the cathode. This limits the rate of reaction, since the less of the catalyst sites are available for the reaction to occur. The concentration overpotential has an exponential relation to the current density. The concentration overpotential is therefore often modeled simply as a limiting current density, since it becomes dominant at high current densities and very suddenly. The equation used to limit the current density is shown in Equation (3.11) [García-Valverde et al., 2012].

$$\epsilon_{\text{conc}} = \frac{R_{\text{u}}\, T}{\alpha_{\text{act}}\, z\, F}\, ln\left(1-\frac{i}{i_L}\right) \quad [\text{V}] \tag{3.11}$$

- ϵ_{conc}: Concentration overpotential [V]
- i_{L}: Limiting current density [A/m^2]

The electrical efficiency of the fuel cell is calculated as the ratio of the instantaneous output power of the fuel cell to the chemical energy of the consumed hydrogen, as shown in Equation (3.12)

$$\eta_{\mathrm{FC}} = \frac{I_{\mathrm{FC}}\ V_{\mathrm{FC}}}{\dot{n}_{H2,cons} LHV_{\mathrm{H2}}} \quad [-] \tag{3.12}$$

- η_{FC}: Fuel cell electrical efficiency [-]
- I_{FC}: Fuel cell stack current [A]
- $\dot{n}_{\mathrm{H2,cons}}$: Molar rate of hydrogen consumption [mol/s]
- LHV_{H2}: Lower heating value of hydrogen [J/kg]

With this the equations necessary to determine the voltage output of the fuel cell stack are defined.

3.1.2 Fitting of Polarization Curve

As previously mentioned the is model fitted to a load cycling test to determine key parameters of the model. These parameters are the reference current exchange density, $i_{0,\mathrm{ref}}$; the activation energy of the current exchange, E_{exc}; the activation energy of the proton exchange, E_{pro}; membrane thickness, t_{m}; reference electrical conductivity, $\sigma_{\mathrm{ohm,ref}}$ and limiting current density, i_{L}. To determine these parameters the Matlab function *fmincon* is used to minimize the total relative error between the predicted power and the actual power. The initial guesses, upper and lower bounds for each of the parameters are shown in Table 3.1

Table 3.1: Initial guesses, lower bounds, upper bounds and final values for key parameters of the fuel cell model fitted using Matlab's *fmincon* function.

Parameter	Unit	Initial Value	Lower limit	Upper limit	Final Value
$i_{0,\mathrm{ref}}$	$\mathrm{A/m^2}$	10^{-3}	10^{-4}	10^{-2}	$1.3 \cdot 10^{-3}$
E_{exc}	J/mol	$325 \cdot 10^3$	$50 \cdot 10^3$	$500 \cdot 10^3$	$161 \cdot 10^3$
E_{pro}	J/mol	10^3	10^3	$20 \cdot 10^3$	$19.8 \cdot 10^3$
t_{m}	m	10^{-3}	10^{-4}	10^{-2}	$2.8 \cdot 10^{-3}$
$\sigma_{\mathrm{ohm,ref}}$	S/m	60	1	10^2	62.8
i_{L}	$\mathrm{A/m^2}$	$12 \cdot 10^3$	$6 \cdot 10^3$	$20 \cdot 10^3$	$7.94 \cdot 10^3$

The fuel cell stack tested during the load cycling test had 30 cells and an active cell area of 296 $\mathrm{cm^2}$ per cell. These parameters will therefore be used in the model fitting, and the number of cells will later be used to scale the fuel cell stack model to the power demand. The data used to fit the model is shown in Figure 3.1.

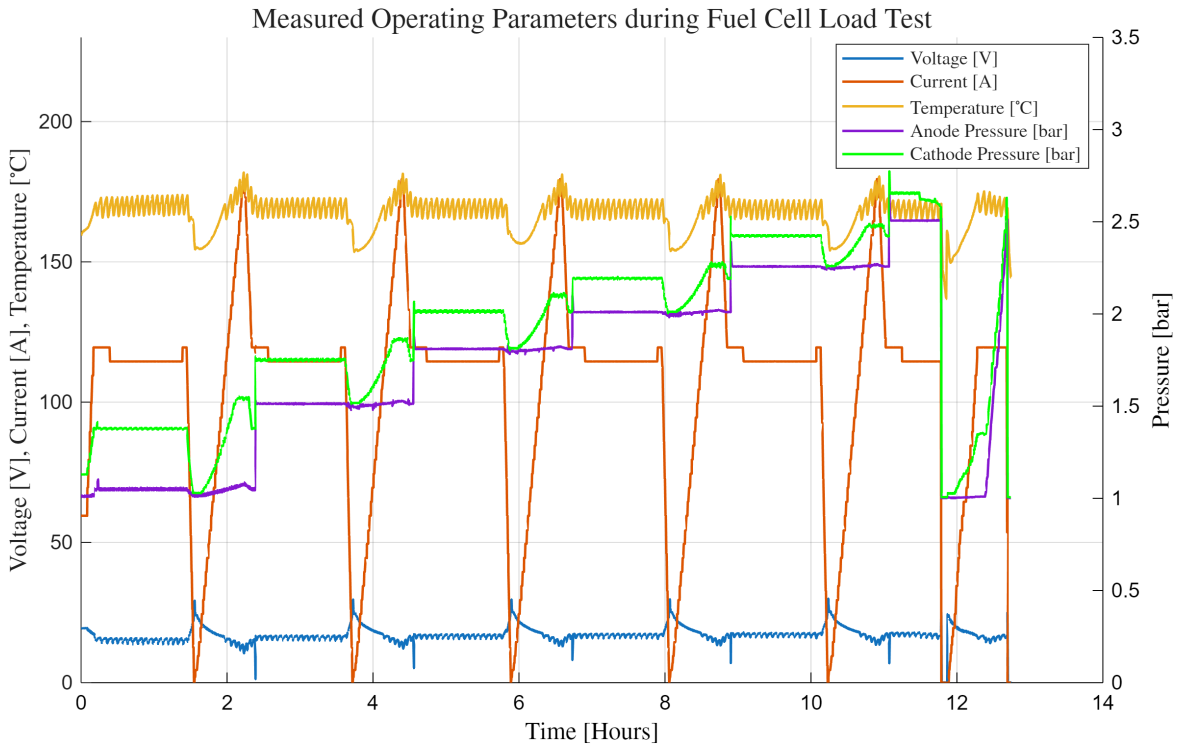

Figure 3.1: Measured operating parameters for a load cycling test used to fit the fuel cell stack model. The test consists of five cycles in which the current ramps from 0 to 120 A and back to 0. During the load cycling test both the anode and cathode pressure is increased for each cycle. Within each cycle the temperature cycles periodically, allowing for fitting of the influence of the temperature in the model.

The temperature measured in the load cycling test is the temperature of the cooling oil leaving the fuel cell stack. This is used a surrogate variable for the temperature of the fuel cell stack, since the internal temperature of the stack is not recorded. The validity of this assumption is explored later in this chapter. Figure 3.2 shows the measured power output of the fuel cell stack during the load cycling test and the simulated power output of the model using the measured current, temperature and pressures as input.

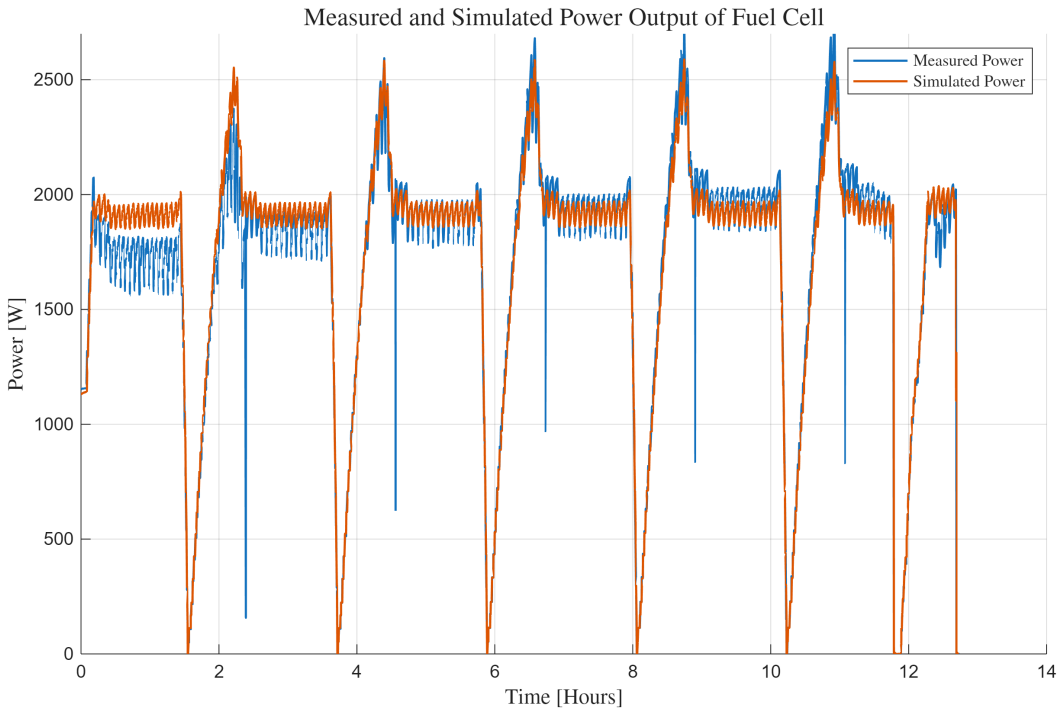

Figure 3.2: Comparison between the measured and simulated power output. The measured current, fuel cell stack temperature, cathode pressure and anode pressures are used as input to the fuel cell model.

Figure 3.2 shows that the model predicts the overall trend of the power output well based on the current input and the temperature of the fuel cell stack. However, the model overestimates the power output at low pressures and underestimates the power output at high pressures, with the model being the most accurate at an anode pressure of 2 bar and a cathode pressure of 2.2 bar. The average relative error of the model is 3.45% across the data set, while the average absolute error being 61 W. With the large variation in both current, temperature and anode and cathode pressures, this is deemed acceptable, especially at pressures around 2 bar for both the anode and cathode. To better illustrate the comparison a single cycle is shown in Figure 3.3.

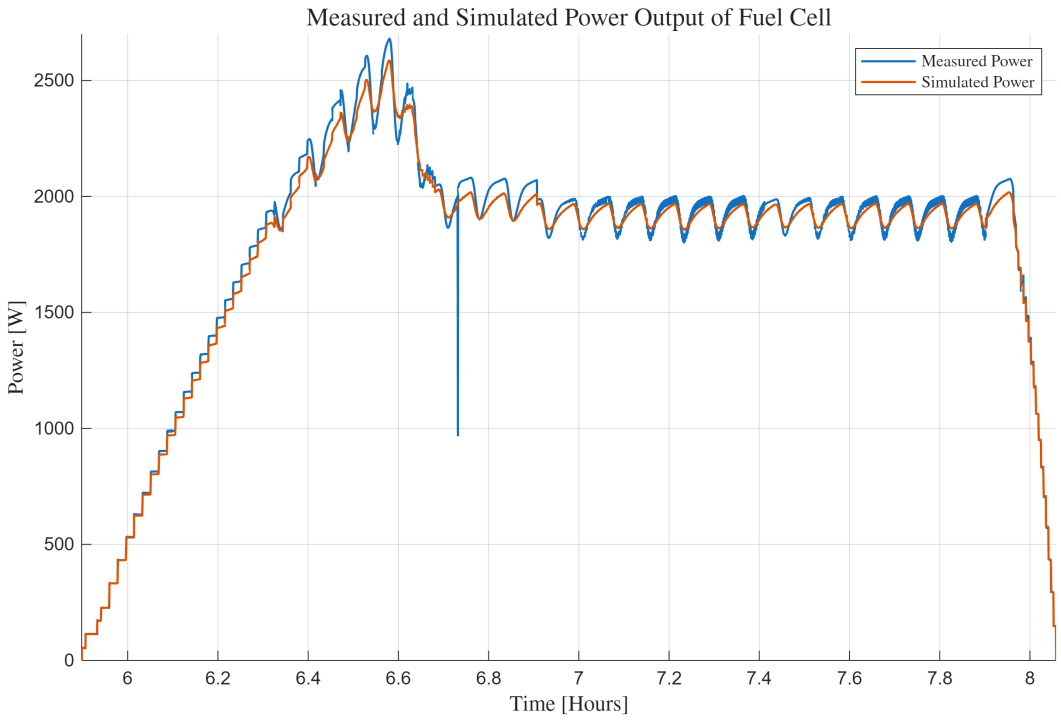

Figure 3.3: Comparison between the measured and simulated power in a single cycle. The measured current, fuel cell stack temperature, cathode pressure and anode pressures are used as input to the fuel cell model.

A separate dataset also produced as part of MFC Multigen project is used as validation of the fitted fuel cell model. The data set used is a combined load cycling and steady load test. The normalized dataset used is shown in Figure 3.4.

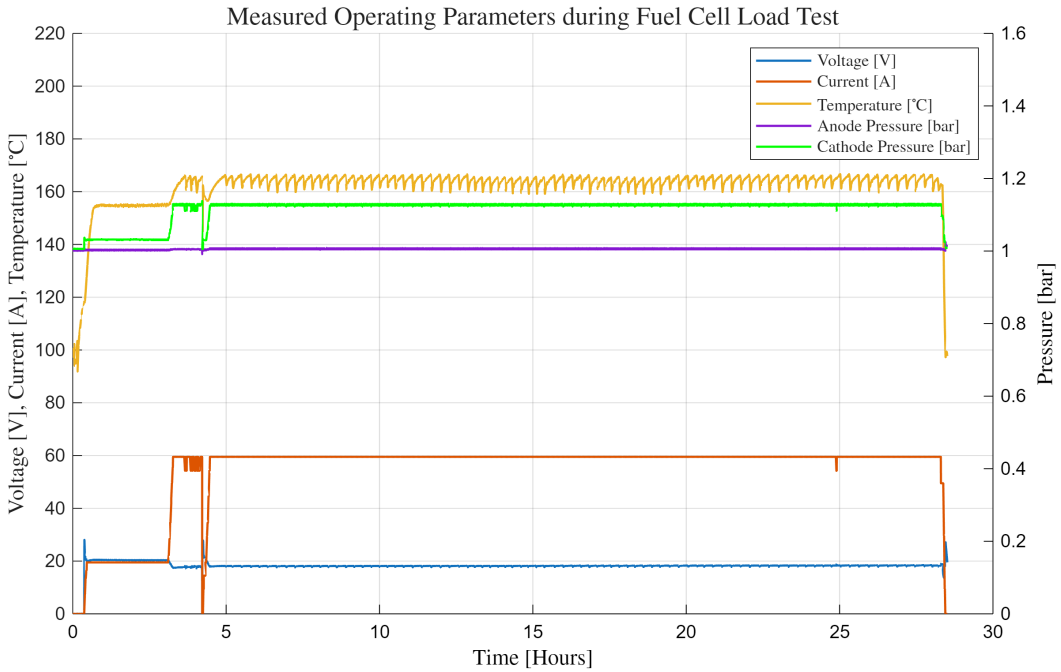

Figure 3.4: Measured operating parameters for a two part load cycling and steady state load test used to validate the fuel cell model.

Unlike the first dataset the anode and cathode pressures are kept constant. The current

is varied in the first part of the test, and kept constant at 59.5 A in the second part. The temperature cycles throughout the test. The comparison between the measured and simulated power is shown in Figure 3.5

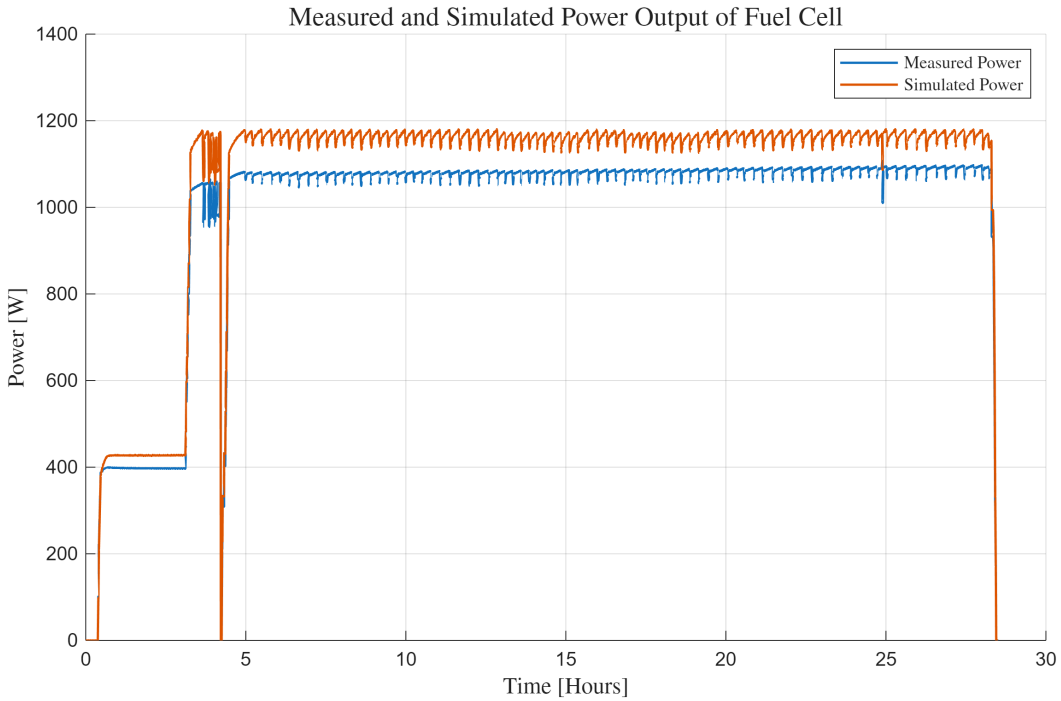

Figure 3.5: Comparison between the measured and simulated power output. The measured current, fuel cell stack temperature,cathode pressure and anode pressures are used as input to the fuel cell model.

The average relative error across the dataset is 8.45% with an average absolute error of 75 W. This is again likely due to the model overestimating the power output at low anode and cathode pressures, since this is what is observed in the validation. Figure 3.6 shows the first 6 hours of the simulation, since the rest of the test is done a steady state, except for the cycling temperature.

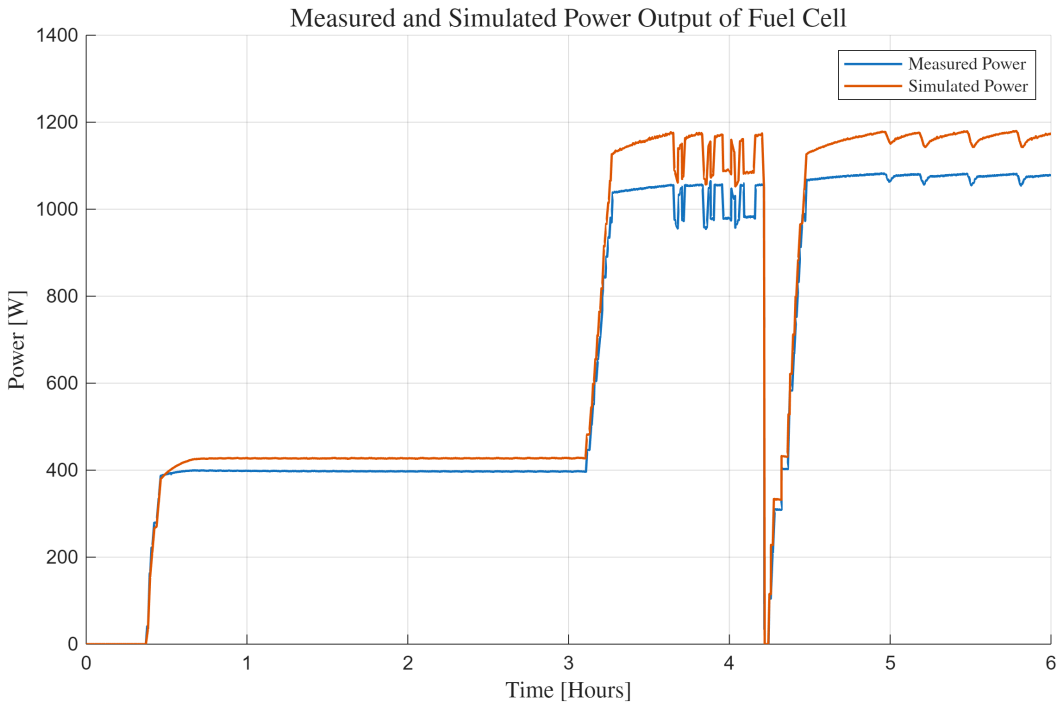

Figure 3.6: Comparison between the measured and simulated power the validation of the fuel cell model for the first 6 hours, since this part contains the dynamic operation of the two part test. The measured current, fuel cell stack temperature,cathode pressure and anode pressures are used as input to the fuel cell model.

Figure 3.6 shows that the behavior of the power output is predicted well, but consistently overestimated. Since this thesis is primarily focused on the dynamics of the fuel cell, this is not a severe issue for the project, but it could be improved upon.

Figure 3.7 presents the modeled polarization curve, illustrating how cell voltage varies with current density at five different temperatures.

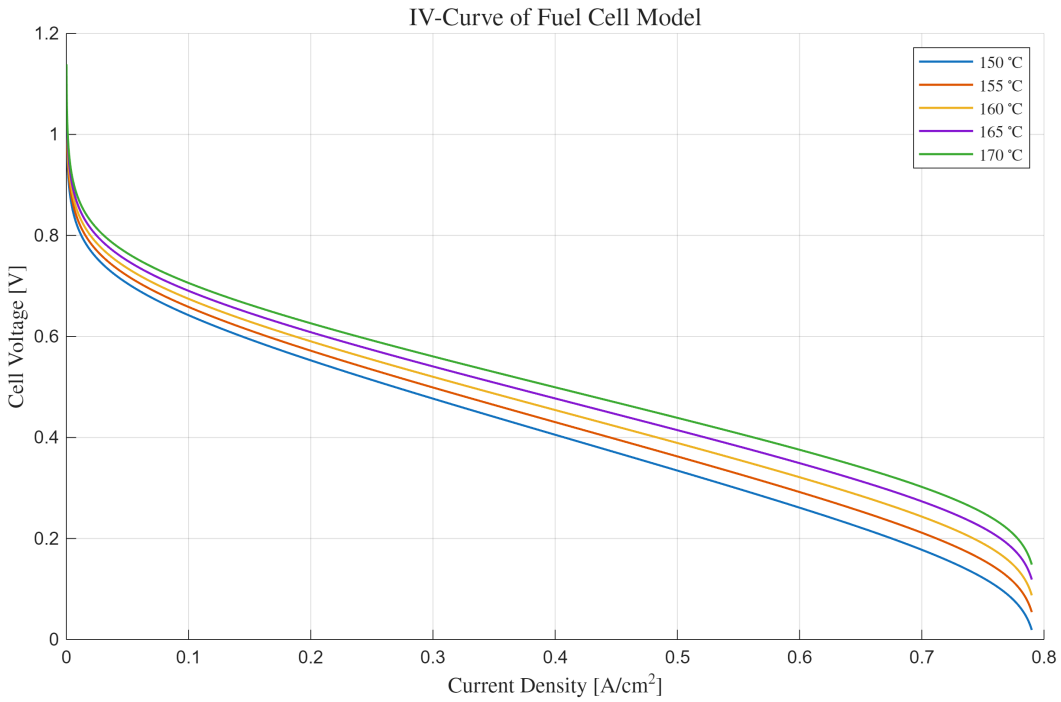

Figure 3.7: Simulated cell voltage as a function of the current density and temperature, with the current varying from 0 to 7.94 A/m^2 and temperature varying form 150 to 170 °C.

The polarization curves of the model display the expected trend of a logarithmic loss from a current density between 0 and 0.1 A/m^2, a linear voltage loss between 0.1 and 0.6 A/m^2 and an exponential voltage loss above 0.6 A/m^2. It is also shown that the voltage losses decrease with an increase in temperature, with a significant difference observed within the operating temperature range of 150 - 170 °C. This difference is even more pronounced in the power curve of the model. The power curve of the model as a function of current density and temperature is shown in Figure 3.8.

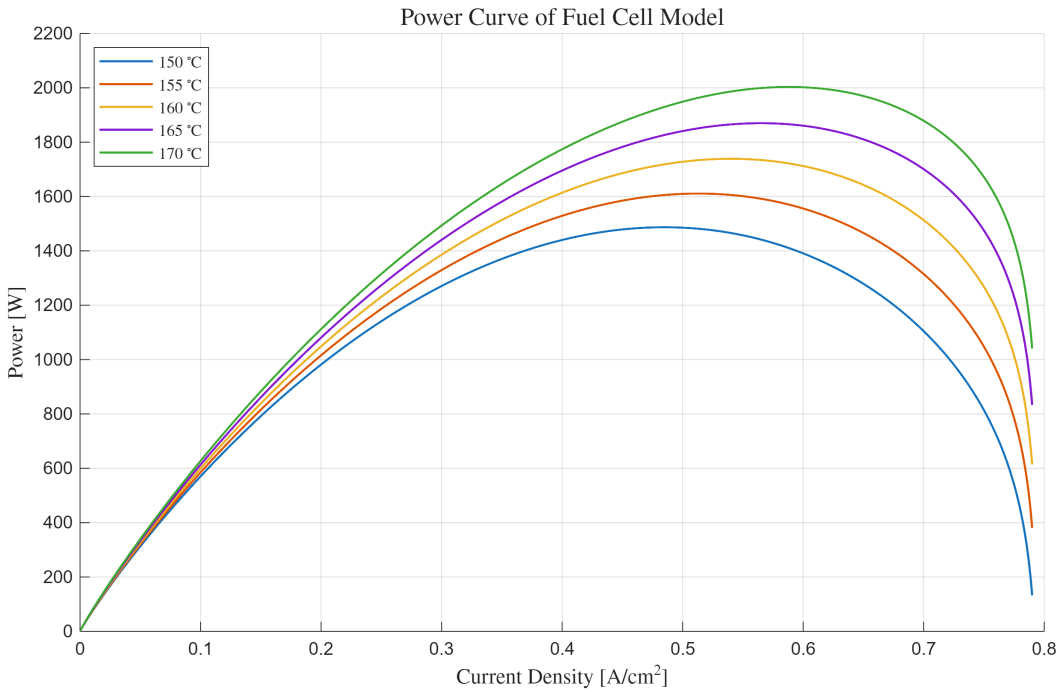

Figure 3.8: Simulated power output of a 30 cell fuel cell stack as a function of the current density and temperature, with the current varying from 0 to 7.94 A/m^2 and temperature varying form 150 to 170 °C.

As observed in Figure 3.8, a fuel cell has a maximum power point at which an increase in current density will lead to a decrease in power output due to the increase in voltage losses being larger than the increase in current. There is therefore no obvious reason to operate at current densities above the maximum power point. As the temperature increases, so does the maximum power point. At 150 °C. the maximum power point is 0.48 A/m^2 with a power of 1.48 kW, while at 170 °C the maximum power point is 0.59 A/m^2 with a power of 2.00 kW. The model efficiency is shown in Figure 3.9.

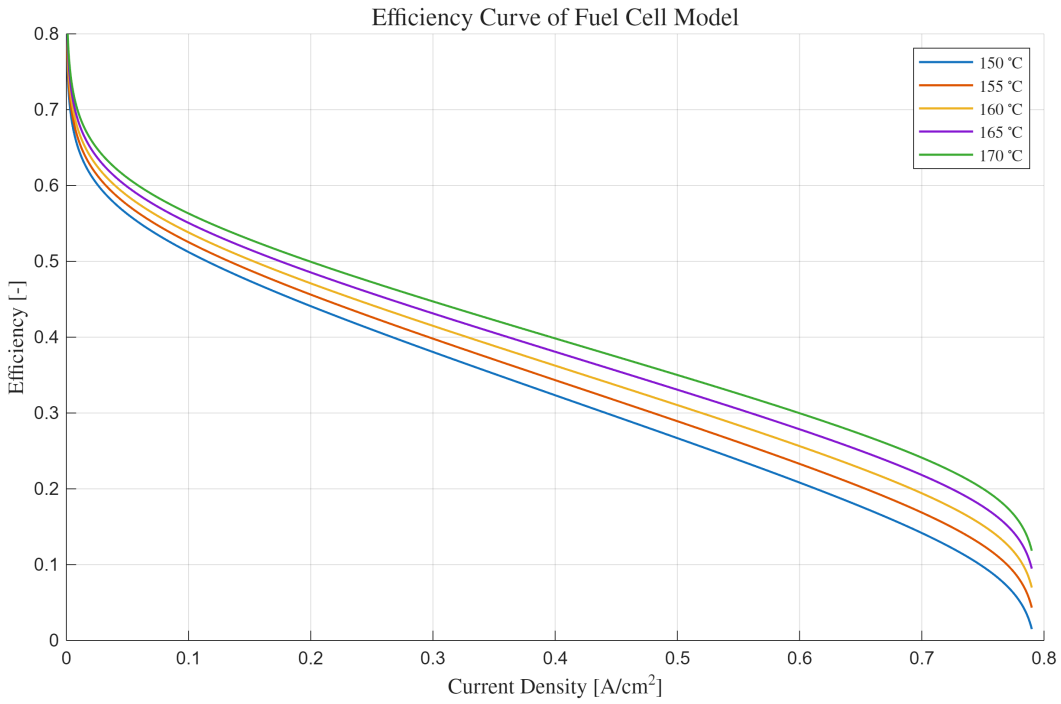

Figure 3.9: Simulated efficiency the modeled fuel cell as a function of the current density and temperature, with the current varying from 0 to 7.94 A/m^2 and temperature varying form 150 to 170 °C.

The electrical efficiency is calculated with regards to the *Lower Heating Value* (LHV), since The efficiency curve is similar to the voltage curve due to the voltage losses being directly proportional to the efficiency losses. As shown in Figure 3.9, the efficiency ranges from 0.27 - 0.3 near the maximum power points, depending on the temperature.

3.2 Thermal Behavior of the Fuel Cell Stack

The strong influence of temperature on cell voltage, observed in the experimental data reproduced in the model illustrates the importance of the thermal behavior of the fuel cell. This section will therefore explain how the thermal behavior is taken into account.

The fuel cell is assumed to be uniform in temperature, and only the heat transfer with the cooling oil is taken into account, when the fuel cell is operating. This allows for determining the fuel cell temperature based on the change in temperature and flow rate of the oil. Heat transfer with the cooling oil occurs in channels within the bipolar plates. The oil used for the fuel cell in this project is *Triethylene Glycol* (TEG)-oil. The key parameters of the oil used are shown in Table 3.2.

Table 3.2: Key thermal properties used for the TEG-oil. [Sagdeev et al., 2012], [Li et al., 2009], [Khayet and Zárate, 2005].

Parameter	Unit	Value
Specific Heat Capacity	J/(kg K)	2393
Density	kg/m^3	1028
Thermal Conductivity	W/(m K)	0.1945
Dynamic Viscosity	Pa s	0.0017

The exact number and measurements of the micro channels are not known, so it is assumed that there are 10 channels per cell and that the channels are 10 mm wide, 2 mm deep and 20 cm long.

Newton's law of cooling is used to calculate the heat transfer between fuel cell and the oil, as shown in Equation (3.13).

$$\dot{Q} = h\ A\ \Delta T \qquad [\mathrm{W}] \tag{3.13}$$

- h: Convective heat transfer coefficient [W/(kg K)]
- A: Surface area [m^2]
- ΔT: Temperature difference [K]

The convective heat transfer coefficient is calculated based on the Nusselt number as shown in Equation (3.14).

$$h = \frac{\mathrm{Nu}\ k}{D_\mathrm{H}} \quad \left[\frac{\mathrm{W}}{\mathrm{m^2\ K}}\right] \tag{3.14}$$

- Nu: Nusselt number [-]
- k: Conductivity of the oil [W/(m K)]
- D_H: Hydraulic diameter [m]

The hydraulic diameter of a square duct is shown in Equation (3.15)

$$D_{\mathrm{H}} = 2\frac{w_{\mathrm{ch}}\, h_{\mathrm{ch}}}{w_{\mathrm{ch}} + h_{\mathrm{ch}}} \quad [\mathrm{m}] \tag{3.15}$$

- w_{ch}: width of channel [m]
- h_{ch}: depth of channel [m]

The surface area of the channels is shown in Equation 3.16.

$$A = L_{\mathrm{ch}}(2\, w_{\mathrm{ch}} + 2\, h_{\mathrm{ch}})\; n_{\mathrm{cell}} \quad [\mathrm{m}^2] \tag{3.16}$$

- L_{ch}: Length of channel [m]
- n_{cell}: Number of cells [-]

The Reynolds numbers observed during simulation with these parameters are in the order of magnitude of Re = 10 or lower, which means that the flow in the channels is laminar. The Nusselt number can therefore be fixed to Nu = 3.96 for a square duct of dimensions used in this project [Cengel et al., 2017].

Due to the large difference between the heat capacities of the fuel cell and the oil flow the fuel cell is assumed to have constant temperature within one iteration, only updating the temperature after the oil has reached the final temperature. This simplifies the calculation of heat transfer, since it is not required to be calculated iteratively. The final temperature is calculated using a first order transfer function as shown in Equation (3.17).

$$T_{\mathrm{oil,out}} = T_{\mathrm{oil,in}} + (T_{\mathrm{FC}} - T_{\mathrm{oil,in}})(1 - e^{-\Delta t_{\mathrm{res}}/\tau_{\mathrm{oil}}}) \quad [\mathrm{K}] \tag{3.17}$$

- $T_{\mathrm{oil,in}}$: Temperature of oil entering the fuel cell [K]
- T_{FC}: Temperature of the fuel cell [K]
- Δt_{res}: residence time of the oil [s]
- τ_{oil}: time constant for the oil [s]

The time constant is the ratio of the rate of heat transfer to the heat capacity of the oil, and it is the time it takes to reduce the temperature difference between the oil and the fuel cell by 63%. This together with the residence time determines, how close the temperature of the oil gets to the fuel cell temperature before leaving it. The time constant of the oil is calculated in each iteration, since it is dependent on the mass flow rate of oil, as shown in Equation 3.18 [Cengel and Ghajar, 2020].

$$\tau_{\mathrm{oil}} = \frac{\dot{m}_{oil}\; c_{\mathrm{p,oil}}}{h_{\mathrm{conv}}\; A} \quad [\mathrm{s}] \tag{3.18}$$

- $\dot{m}_{oil}$: mass flow rate of the oil [kg/s]
- $c_{\mathrm{p,oil}}$: specific heat capacity of the oil [J/(kg K)]
- h_{conv}: Convective heat transfer coefficient [W/(m^2 K)]

- A: Heat transferring area [m^2]

The temperature of the fuel cell is then updated based on the heat generated by the fuel cell, the heat removed from the fuel cell and heat capacity of the fuel cell itself, as shown in Equation (3.19)

$$T_{\text{FC,new}} = T_{\text{FC}} + \frac{\dot{Q}_{\text{gen}} - \dot{Q}_{trans}}{M_{\text{FC}} c_{\text{p,FC}}} \Delta t \quad [\text{K}] \tag{3.19}$$

- $T_{\text{oil,in}}$: Temperature of oil entering the fuel cell [K]
- $\dot{Q}_{gen}$: Heat generated by the fuel cell [W]
- $\dot{Q}_{trans}$: Heat transferred to the oil [W]
- M_{FC}: Mass of the fuel cell [kg]
- $c_{\text{p,FC}}$: Average specific heat capacity of the fuel cell [J/(kg K)]
- Δt: Time step [s]

Since neither the mass of the fuel cell or the specific heat capacity is known, only a total heat capacity of the fuel cell can be estimated. Based on the heat transferred and the rate of change of the fuel cell temperature, The heat capacity of the fuel cell is estimated to be $Mc_{\text{p,FC}}$ = 28000 J/K. The heat generated by the fuel cell is calculated from its efficiency, representing the portion of chemical energy from the consumed fuel that is not converted into electrical power. This residual energy, released as heat, is described by Equation (3.20).

$$\dot{Q}_{\text{gen}} = \frac{P_{\text{FC}}}{\eta_{\text{FC}}} - P_{\text{FC}} \quad [\text{W}] \tag{3.20}$$

- $\dot{Q}_{gen}$: Heat generated by the fuel cell [W]
- P_{FC}:Electrical power output of the fuel cell [W]
- η_{FC}: Electrical efficiency of the fuel cell [-]

The results of applying the model of the fuel cell stack temperature dynamic to the data from the load cycling test is shown in Figure 3.10.

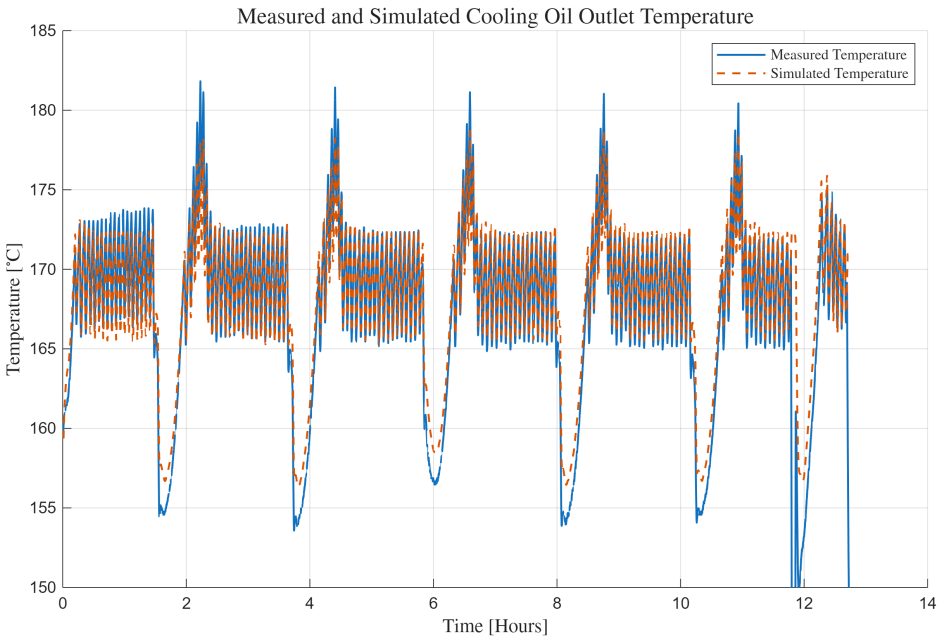

Figure 3.10: Measured and Simulated outlet temperature of the cooling oil. For the simulated temperature the heat generated in the fuel cell and the inlet temperature of the cooling oil is used as inputs.

To better illustrate the comparison between the simulated temperature and the measured temperature, Figure 3.11 shows a zoomed view of a single cycle of the results shown in Figure 3.10.

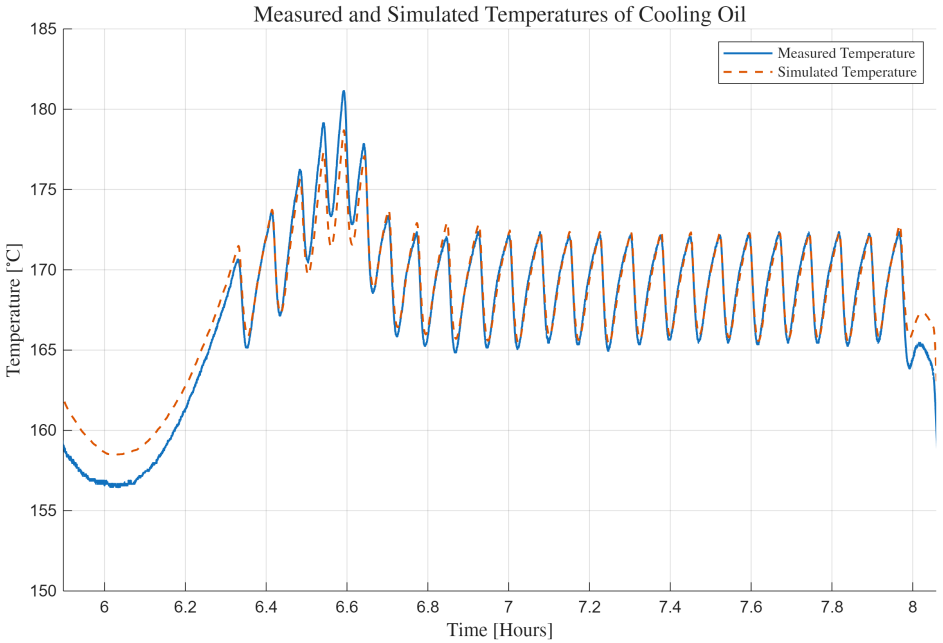

Figure 3.11: Figure 3.10 zoomed in on a single cycle of the current.

Figure 3.10 and Figure 3.11 show good agreement between the measured outlet temperature of the cooling oil and the simulated outlet temperature. This indicates that the combined fuel cell and heat transfer model are sufficient to describe the thermal dynamics of the fuel cell system. However, the modeling relies on the assumption that the tempera-

ture of the cooling oil is a good surrogate variable for the temperature of the fuel cell. The model is used to test this assumption by comparing the simulated temperature of the fuel cell with the simulated outlet temperature of the oil. Figure 3.12 shows this comparison between the fuel cell temperature and the oil outlet temperature.

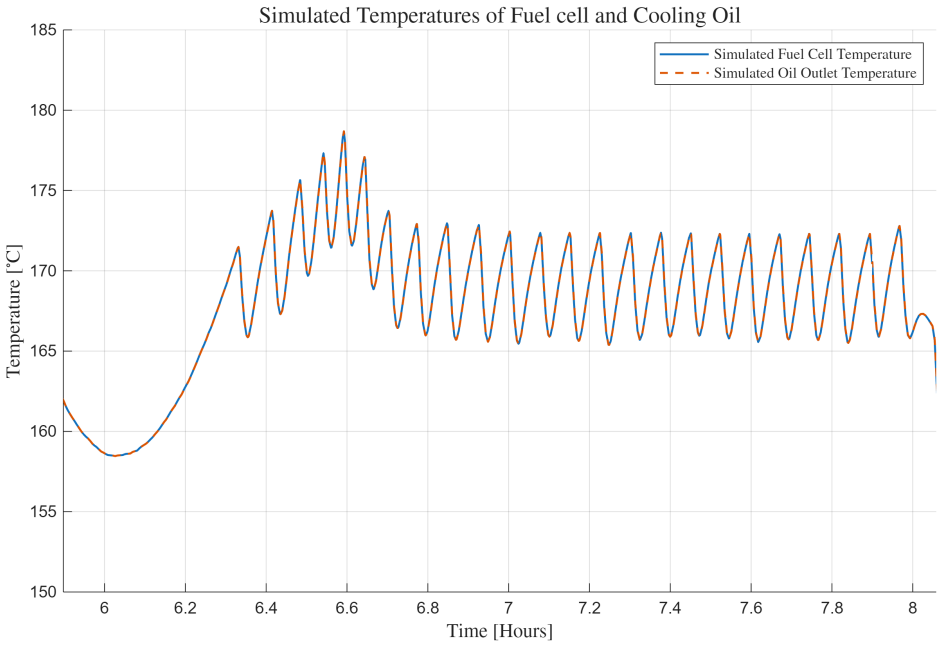

Figure 3.12: The simulated relation between the outlet temperature of the cooling oil and the fuel cell temperature, for a single current cycle of the load cycle test.

Figure 3.12 show that in the model, the fuel cell and cooling oil reach a common temperature. This indicates that the outlet temperature of the oil is a good surrogate variable for the temperature of the fuel cell stack.

The temperature of the fuel cell is controlled by changing the inlet temperature of the cooling oil. The control mechanism used to control the fuel cell temperature is described by Equation (3.21).

$$T_{\text{oil,in,new}} = T_{\text{oil,in}} - 0.05(T_{\text{oil,out}} - T_{\text{FC,sp}})\Delta t \quad [\text{K}] \tag{3.21}$$

- $T_{\text{oil,in,new}}$: Temperature setpoint of oil entering the fuel cell for the next iteration [K]
- $T_{\text{oil,in}}$:Inlet temperature of the oil for the current iteration [K]
- $T_{\text{oil,out}}$: Inlet temperature of the oil for the current iteration [K]
- $T_{\text{FC,sp}}$: setpoint temperature of the fuel cell [K]
- Δt: Time step [s]

The cooling oil in this project is cooled by exchanging heat with the domestic *Hot Water Tank* (HWT). How the inlet temperature of the oil is controlled is beyond the scope of the project, but it could be done in one of several ways, such as controlling the flow rate of both the cooling oil and the water from the HWT, or implementing a bypass system with a mixing valve to regulate the proportion of oil that passes through the heat exchanger before rejoining the main loop.

3.2.1 Hot Water Tank

The heat extracted from the oil cooling loop is transferred to the HWT through a heat exchanger. The heat transferred is calculated as shown in Equation (3.22)

$$\dot{Q}_{HWT} = (T_{\text{oil,in,new}} - T_{\text{oil,out}})\ c_{\text{p,oil}}\ \dot{m}_{\text{oil}} \quad [\text{W}] \tag{3.22}$$

- $\dot{Q}_{HWT}$: Heat transferred to the HWT [W]
- $T_{\text{oil,in}}$: Inlet temperature of the oil for the current iteration [K]
- $T_{\text{oil,out}}$: Inlet temperature of the oil for the current iteration [K]
- $T_{\text{FC,sp}}$: setpoint temperature of the fuel cell [K]
- Δt: Time step [s]

The heat extracted from the HWT is determined by the domestic heat demand. This is subtracted from the heat transferred from the oil when the temperature of the HWT is updated as shown in Equation (3.23)

$$T_{\text{HWT,new}} = T_{\text{HWT}} + \frac{\dot{Q}_{\text{HWT}} - \dot{Q}_{\text{demand}}}{M_{\text{H2O}} c_{\text{p,H2O}}} \Delta t \quad [\text{K}] \tag{3.23}$$

- $T_{\text{HWT,new}}$: Updated temperature fo the HWT cell [K]
- T_{HWT}: Current temperature of the HWT [K]
- $\dot{Q}_{HWT}$: Heat transferred from the oil [W]
- $\dot{Q}_{\text{demand}}$: Heat demand [W]
- M_{HWT}: Mass of water in the HWT [kg]
- $c_{\text{p,HWT}}$: Specific heat capacity of water [J/(kg K)]
- Δt: Time step [s]

The HWT model does not take into account the tank itself in the heat capacity of the HWT system, and heat loss to the surroundings is neglected. The mass of water is assumed to be 500 kg. When hot water is used cold water replaces the extracted water, thus lowering the temperature. The temperature of the water is not allowed to descend below a threshold of 60 °C or exceed a threshold of 65 °C [Xie et al., 2025]. If the temperature exceeds 65 °C, the water must be cooled using a fan or by other means, either before or after heat exchanging with the oil in order to keep the temperature of the HWT below the threshold. If the temperature of the HWT is below 60 °C, a heat pump is activated to keep the temperature above the threshold. The additional cooling and heating required is calculated, as to keep the HWT within the thresholds.

3.3 Operation States

During operation, the behavior of the fuel cell stack is controlled by the control signal received from the mid-level control layer and the internal state logic of the fuel cell module. The fuel cell can be in one of 5 states, depending on the EMS signal, the operation state and the temperature of the fuel cell stack. These 5 states are *Warmup*, *Standby*, *Operation*, *Active Cooldown* and *Off*. These 5 states have been chosen based on data acquired from *Blue World Technologies* during a cycle test conducted on one of their prototype *Methanol Steam Reforming* (MSR) HT-PEMFC systems. The data obtained from *Blue World Technologies* is shown in Figure 3.13.

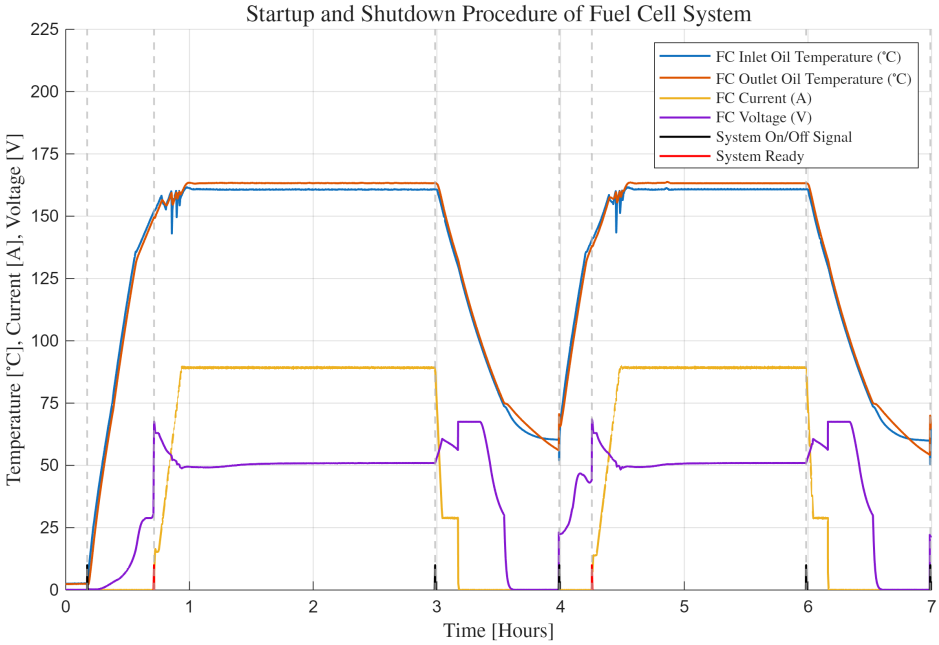

Figure 3.13: Oil temperatures at the inlet and outlet of the fuel cell, current, voltage and On/Off signals, measured during a startup/shutdown test performed by Blue World Technologies on a prototype MSR HT-PEMFC system.

Figure 3.13 shows two startup/shutdown cycles, with the first cycle starting from ambient temperature and the second starts before the fuel cell has cooled down. Once the fuel cell reaches a high enough temperature, the current is increased to 10 A within the first second. Afterwards the current is ramped with a near constant ramp rate of approximately 0.1 A/s. During operation the oil temperatures, current and voltage are all kept constant. Once the system is turned off, the fuel cell continues to be cooled using the oil loop, until it reaches a temperature of approximately 75 °C, after which the oil loop is turned off and the fuel cell stack is cooled only passively by heat transfer to the surroundings. When the oil loop is turned off the outlet temperature of the oil is no longer a good surrogate variable for the temperature of the fuel cell stack.

3.3.1 Warmup

Starting from an "off" state the fuel cell model receives an EMS "on" signal, and goes into warmup phase. To heat the fuel cell, a startup heater connected to the oil loop is turned on. As the heater begins to heat up, it transfers thermal energy to the circulating oil. The

heated oil then flows through the fuel cell, gradually raising its temperature. After passing through the fuel cell, the oil returns to the heater, which continues to increase in temperature, completing the thermal loop. This process continues until the fuel cell reaches its minimum operating temperature and is ready for power production.

Based on the time it takes to heat the fuel cell, the heat produced by the startup heater is estimated to be 3 kW. The thermal dynamics of the startup heater is modeled using the same equations as the thermal dynamics of the fuel cell. The heat capacity of the startup heater is estimated to be $Mc_{\text{p,startup}} = 5000$ J/K based on the obtained data.

3.3.2 Standby

When the fuel cell reaches the minimum operational temperature, in this project chosen to be 150 °C, it is ready to produce power. However, the reformer might not have reached its minimum temperature, and thus the mid-level control layer has not sent the fuel cell model an "on" signal for the operation state. In this case the fuel cell model goes into the *Standby* state. When in this state the temperature of the fuel cell is kept constant, so as to be ready when the "on" signal is received.

3.3.3 Operation

Once the fuel cell module has received an "on" signal for the operation state, power begins to be produced. Unlike the physical fuel cell, which is ramped with a constant change in current, the fuel cell module is ramped with constant change in power. The fuel cell module is therefore allowed to increase to 600 W instantly, after which the power is ramped at a constant rate of 5 W/s, as to mimic the ramp rate of current of the physical fuel cell. The same ramp rate of power is used when the power setpoint of the fuel cell increases. When the setpoint of the power is reduced, the power is allowed to be ramped down at a rate of 15 W/s, since the physical fuel cell current is allowed to ramped down at a rate of 0.3 A/s. The anode pressure is chosen to be 2 bar, the cathode pressure chosen to be 3 bar, the anode hydrogen stoichiometry is chosen to be 1.25 and the cathode air stoichiometry is chosen to be 2.5 [Yan et al., 2006]. The number of cells in the stack is chosen to be to be 90 cells based on the data acquired from Blue World Technologies.

3.3.4 Active Cooldown

When the fuel cell model receives an "off" signal for the operation state, the oil loop continues to cool the fuel cell as the current is ramped down. The current is ramped down at a rate of 15 W/s, until it reaches 0. The inlet temperature of the cooling oil is set to be 1 °C below the temperature of the fuel cell. Once the temperature of the fuel cell reaches 75 °C, the state changes to *Off*.

3.3.5 Off

Once reaching 75 °C, the fuel cell system is completely shut down, however, the fuel cell is still cooling down due to heat loss to the surroundings. This cooldown is modeled using a first order transient. In the recorded data the fuel cell cools down from 74.9 to 70.2 °C in approximately 4000 seconds between the stop of the oil flow in the first cycle

to the beginning of the second cycle. Since the system is started from a cold start in the first cycle, the temperature of the oil loop at the beginning is assumed to be equal to the ambient temperature at 3 °C. The ambient temperature is assumed to be constant throughout the test. The heat loss to the surroundings is described in Equation (3.24).

$$T_{FC,2} = (T_{FC,1} - T_{\text{amb}})(1 - e^{\frac{\Delta t}{\tau_{\text{FC}}}}) + T_{FC,1} \quad [\text{K}] \tag{3.24}$$

- $T_{FC,1}$: Initial temperature [K]
- $T_{FC,2}$: Final temperature [K]
- Δt: Step size [s]
- τ_{FC}: Time constant [s]

Solving this equation for the time constant yields a time constant of $25{\cdot}10^3$ seconds. The fuel cell model will cool down by this function until the fuel cell either reaches ambient temperature or is turned on again, starting the cycle over again.

3.3.6 Comparison with Reference Data

The startup and shutdown procedures of the model were compared to reference data using identical trigger points for the on/off signals. This comparison is illustrated in Figure 3.14.

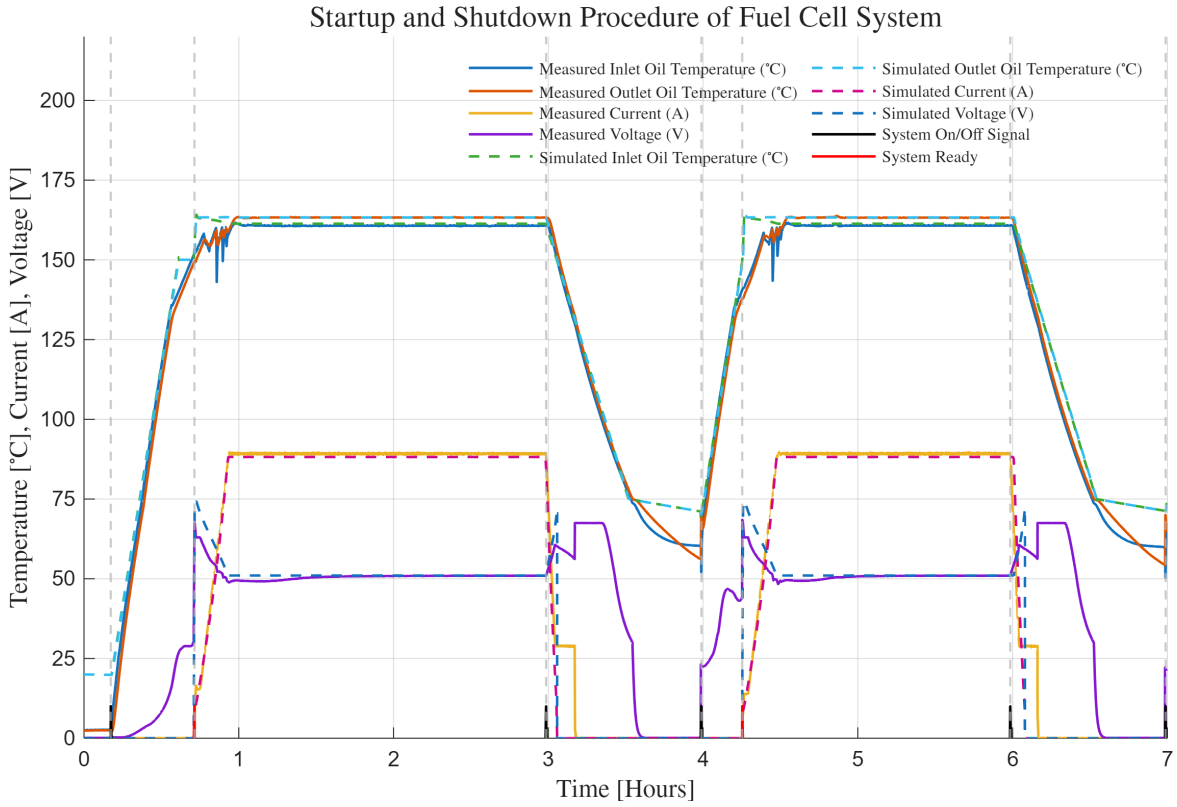

Figure 3.14: Comparison between the modeled startup and shutdown procedures and reference data recorded by Blue World Technologies using the same trigger points for the on/off signals. Compared are the oil temperatures at the inlet and outlet of the fuel cell, current and voltage.

The steady state oil outlet temperature is 163 and the steady state power output is 4.5 kW. These values are used as input to the model for the comparison. The predicted temperatures in the initial phase of the warmup state has very similar slope to the reference data, however, a change in the rate of warmup is observed in the reference data at a temperature of approximately 130 °C, which is not taken into account in the model. This leads the model to reach standby phase before the referenced fuel cell is warm enough to produce power. The simulated voltage during the power ramp up is larger than the measured voltage. This is likely caused by the lower temperature of the tested fuel cell stack during initial ramp up. In the model, voltage is only calculated when power is being drawn. As a result, the simulated voltage differs significantly from the reference data during the periods before startup and after shutdown, when the physical system still reports a voltage but the model does not. However, since no power is produced during these phases, this discrepancy is not considered critical for the purposes of system modeling. The predicted cooldown behavior of the system closely matches the reference data, which is expected given that the model was designed to replicate the same shutdown sequence. There is overall good agreement between the reference data and the simulated data, both in terms of steady state values of the temperatures, current and voltage, but also in the dynamics of the system.

Chapter 4

Reformer Hardware-in-the-Loop Module

This chapter presents the MSR system developed for integration into a high-temperature PEM fuel cell-based micro-CHP platform. The reformer serves as the hydrogen production subsystem, converting a methanol–water mixture into a hydrogen-rich reformate gas via catalytic steam reforming. To enable realistic testing, a physical test bench has been implemented and integrated into the larger HiL simulation framework. The reformer chapter outlines the physical components of the test bench, the instrumentation used for monitoring and control, and the oil-based thermal system that regulates reformer temperature. It also details the control strategies used to modulate gas composition, particularly methanol slip and CO levels, via temperature and flow regulation. The characterization experiments and resulting gas composition models are presented to demonstrate the reformer's dynamic behavior under varying operational conditions. The chapter concludes with a discussion of how the reformer system communicates with the mid-level control layer and the predictive EMS for system-wide coordination. The last part cover the conversion from the measured gas compositions to the molar flow rates and the estimation of required feed flow of methanol for the fuel cell module.

4.1 Reformer Test Bench

The reformer test bench at AAU's Fuel Cell Laboratory was adapted from an existing setup to meet the requirements of this project. It enables remote real-time operation, providing control over key parameters including feed flow rate of a methanol/water mixture, evaporator oil temperature, and reformer oil temperature. Real-time monitoring capabilities include internal catalyst bed temperature measurements and analysis of the reformate gas composition. These features make the system well-suited for experimental studies on methanol steam reforming under dynamically varying conditions.

Figure 4.1 illustrates the *Piping and Instrumentation Diagram* (P&ID) of the reformer test bench. The diagram highlights the locations of temperature sensors distributed throughout the system all of which are thermocouples of the K-type, as well as the gas analysis unit. The gas analysis unit enables dynamic measurement of the reformate gas composition, specifically the concentrations of methanol, H_2, CO, and CO_2.

Figure 4.2 shows an overview of the main part of the reformer test bench, the gas analysis unit can be seen in figure 4.4

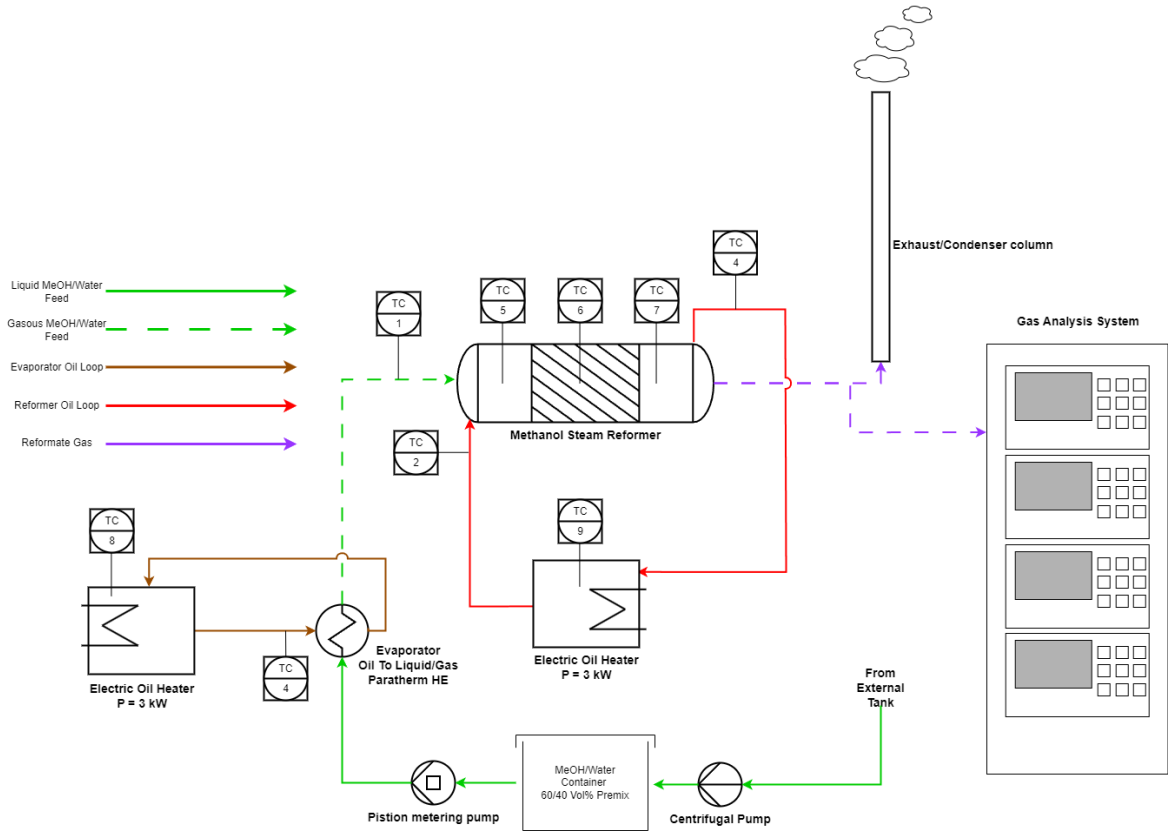

Figure 4.1: P&ID of the reformer test bench illustrating the flow paths of the methanol/water mixture to the reformate gas outlet, as well as the individual heating oil loops for the evaporator and reformer. The approximate locations of the seven thermocouples used for temperature monitoring are also indicated.

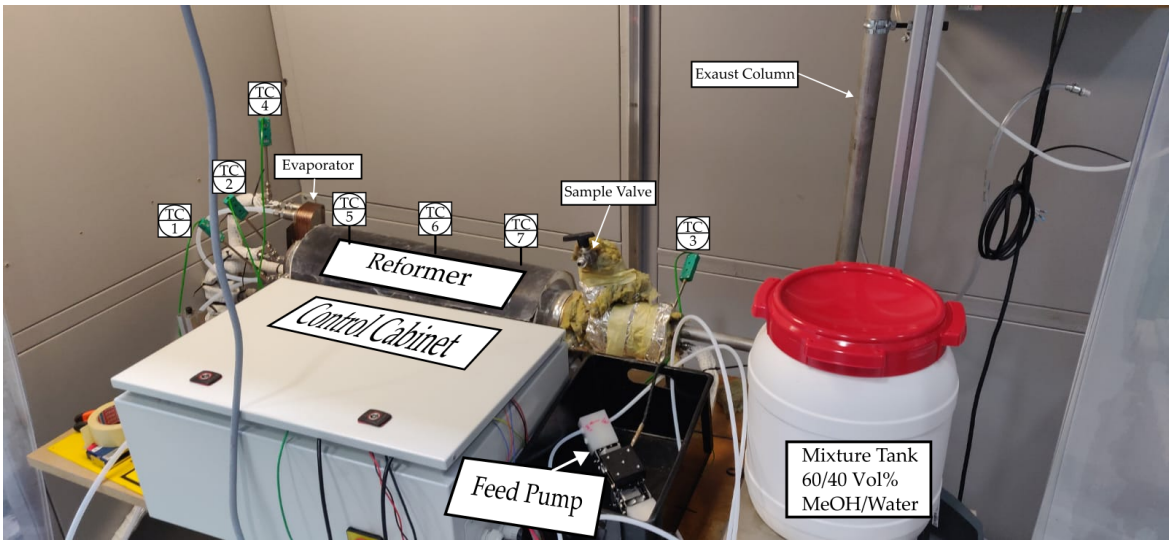

Figure 4.2: Overview of reformer test bench

The reformer test bench consists of a cylindrical packed-bed steam methanol reformer, an evaporator, a methanol/water mixture feed system, and a gas analysis system. The steam methanol reformer and the evaporator are each heated by independent oil heating circuits.

A 60/40 Vol%, corresponding to a steam-to-carbon ratio of 1.5, mixture of methanol and water is fed by a dual-headed displacement pump into an oil-heated evaporator for complete evaporation. The resulting vapor mixture is then fed into the insulated packed-bed reformer, which is filled with a commercially available $CuO/ZnO/Al_2O_3$-based catalyst. The internal temperatures of the catalyst bed are measured at three points along the length of the reformer, spaced approximately 20 cm apart.

A conceptual illustration of the tubular packed bed reformer can be seen in 4.3.

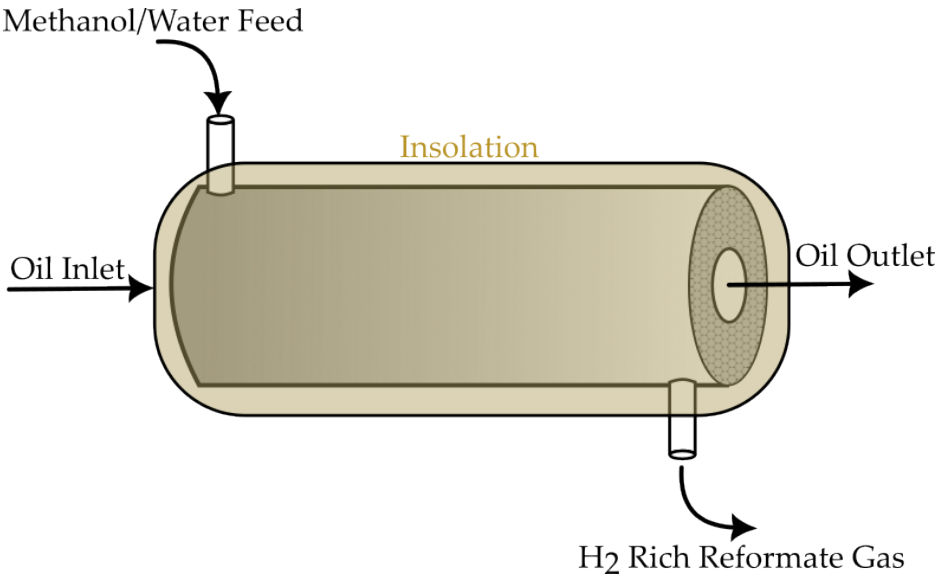

Figure 4.3: Illustration of the tubular packed bed reformer

After exiting the reformer, a continuous sample of the reformate gas is extracted by the gas analysis unit using its internal pumping system. The remaining reformate gas is safely vented through an exhaust column that leads to a vent hood. At the base of the exhaust column, a condensation discharge port collects condensed water and trace amounts of methanol into a container placed within the vented area.

The composition of the reformate gas is measured from the extracted sample. The gas analysis unit includes several devices, each dedicated to specific gas components. A Siemens Fidamat 6, which is a flame ionization detector, measures the total hydrocarbon content of the sample used here to measure methanol. The Fidamat 6 is capable of operating in wet gas conditions with up to 100% H_2O vapor. However, the other gas analyzers require dry gas, so the water content in the sample is first condensed and separated.

Following this drying process, the remaining gas composition is analyzed. A Siemens Ultramat 6 is used to measure CO and CO_2 concentrations. It operates using a *Non-Dispersive Infrared* (NDIR) two-beam alternating light principle [Siemens AG, ndb]. For H_2 measurement, a Siemens Calomat 6 is used, which relies on differences in thermal conductivity between gases [Siemens AG, nda]. The gas analysis unit transmits all measurements in real time to the host computer. From there, the data is transmitted at a frequency of 1 Hz, enabling remote monitoring and integration with the larger DTA-based test architecture.

An overview of the gas analysis unit is shown in Figure 4.4. The image displays the four individual devices used to analyze the components of the reformate gas. Of these, the top three analyzers are actively utilized, while the bottom device is not currently in use for reformate gas analysis. Mounted on the right side of the server-style rack is the heat-traced gas sample line. This heat tracing is crucial, as it prevents condensation of water and methanol during transport from the reformer outlet to the analyzers.

To the right of the rack, a control cabinet houses the hardware responsible for transmitting measurement data via *Network-Published Shared Variables* (NPSVs) to the host computer. Not shown in the image is the external condenser unit, which processes the sample gas by removing water and methanol before it reaches the Calomat 6 and Ultramat 6 analyzers, both of which require dry gas for accurate operation. After analysis, the sample gas is safely vented through a dedicated exhaust line connected to a vent.

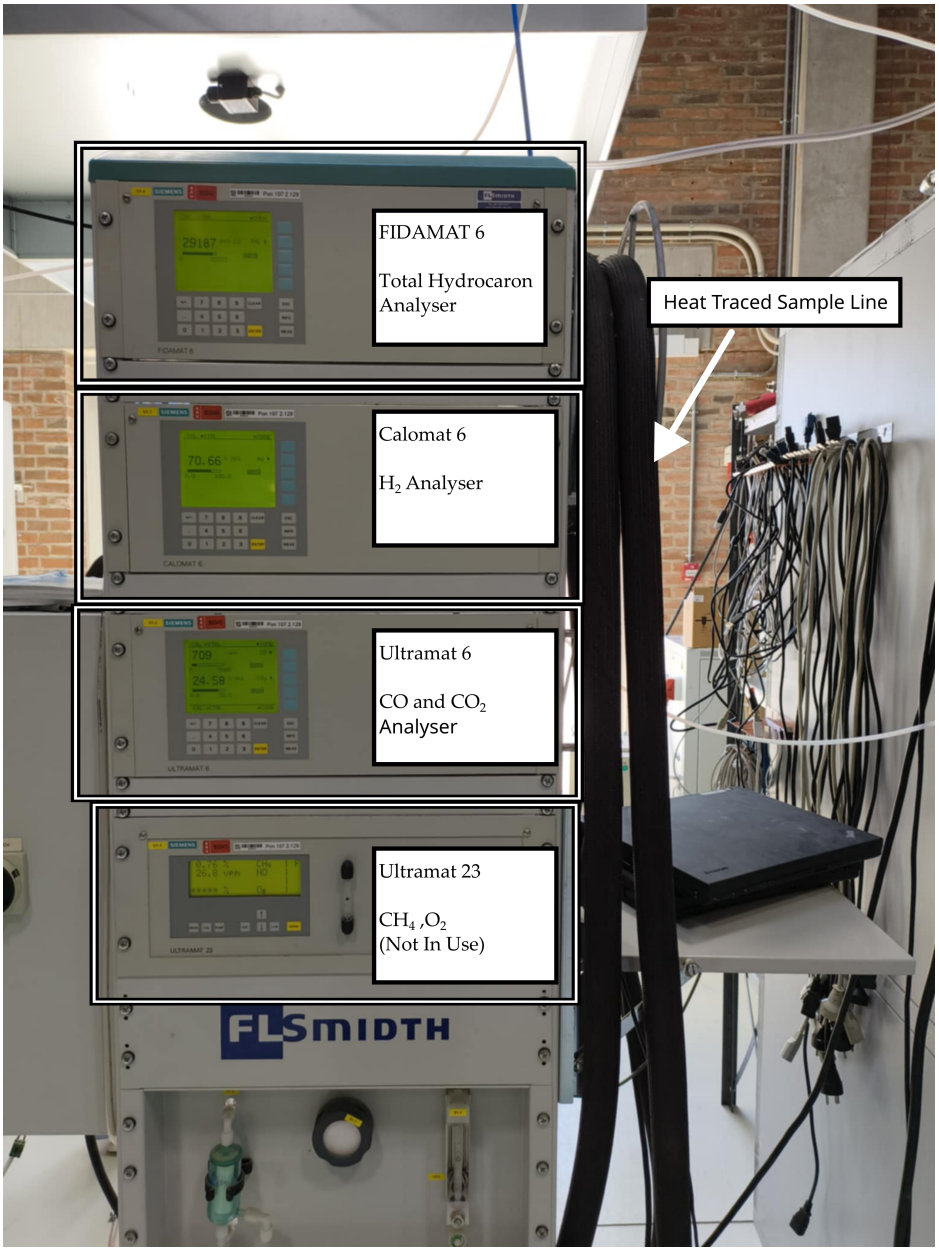

Figure 4.4: Overview of the gas analysis unit

Two 3 kW oil bath heaters are used to heat the oil in the individual circuits. These heaters are controlled by the cRIO deployable controller via serial communication using the RS-232 standard. The controllable parameters include setting the desired oil temperature setpoints, activating or deactivating the heaters, and engaging or disengaging the oil circulation pumps.

4.1.1 Reformer Control and Data Distribution

The reformer test bench is operated by a cRIO-9056 deployable controller equipped with modules for digital I/O, thermocouple inputs, and serial communication. A LabVIEW program deployed on the cRIO manages the communication with these modules, acquiring measurement data and executing control commands. The cRIO sends real-time measure-

ment data, such as temperature readings and system status, via NPSVs to a host computer located in the same laboratory. It also receives control commands from the host computer, which it uses to regulate the feed flow rate and the temperatures of the oil heating circuits.

The host computer serves as a graphical user interface (GUI), enabling manual operation of the reformer system. It also acts as a central hub for aggregating data from both the reformer and the gas analysis unit. This aggregated data is transmitted to the mid-level layer, making it accessible to any external clients. In addition to transmitting data, the host computer receives remote control commands from the mid-level layer. This dual functionality enables the GUI to switch between manual local control and remote control. Pictures of user interface is available in Appendix B.

The tables listing all of the variables transmitted to and received from the laboratory host computer can be found in Appendix table D.1 and D.2. Transmitted variables include real-time measurement data from the reformer test bench, gas analysis unit and control setpoints, while received variables consist of control commands such as start/stop signals, setpoints, and toggles from external clients or EMS layers. This data exchange enables both remote monitoring and control within the modular DTA framework.

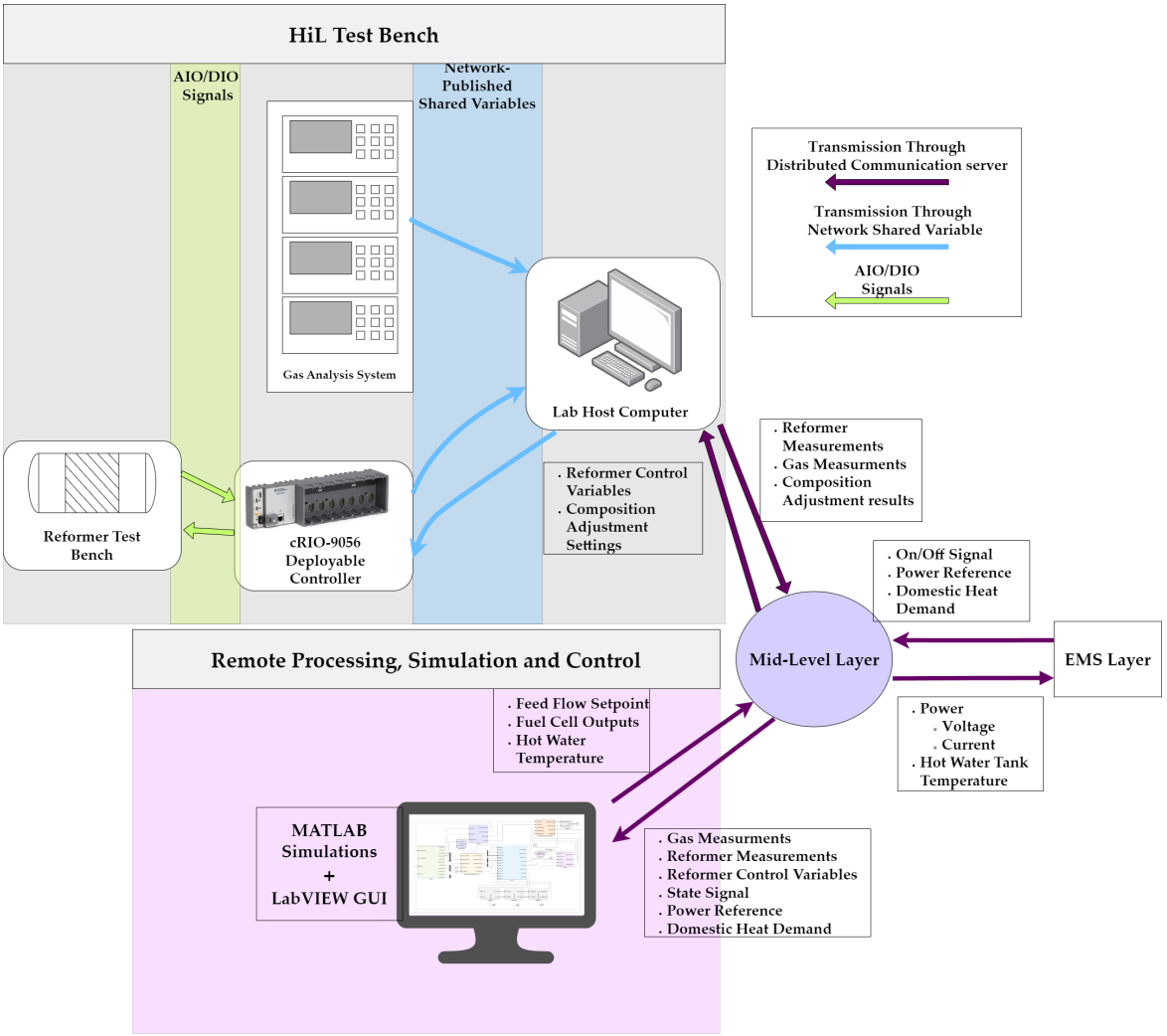

Figure 4.5: Communication architecture of the distributed test system.

4.2 Delay Estimations

From a system integration perspective, it is important to quantify the time delay between a change in the feed flow and a corresponding change in the reformate gas composition. This dead-time influences the responsiveness and stability of any control or monitoring system applied to the reformer.

To estimate the shortest delay, two complementary tests were carried out. In the first test, a step change from 0 to the max flow of 80 ml/min was introduced to the feed flow rate while the response in the reformate gas was monitored using the gas analysis unit. The time between the input change and the first visible response in the gas composition provides a measurement of the total delay in the system.

To isolate the transport delay from the internal dynamics of the reformer, a second test was conducted. In this test, a valve located at the sampling point of the gas analysis unit was changed from a closed state to an open state during steady-state operation of the reformer. This introduced a sudden and detectable change in gas composition without involving

the reformer itself. The time it took for this change to be registered by the gas analysis unit represents the transport delay between the sampling point and the measurement unit.

By subtracting this transport delay from the total delay observed in the first test, it is possible to estimate the internal response delay of the reformer itself. This distinction is essential for building predictive models and implementing real-time monitoring or control strategies with improved accuracy.

Gas Transport Delay Estimation

Figure 4.6 shows the result of the test used to estimate the delay between the reformer outlet and the gas analysis unit.

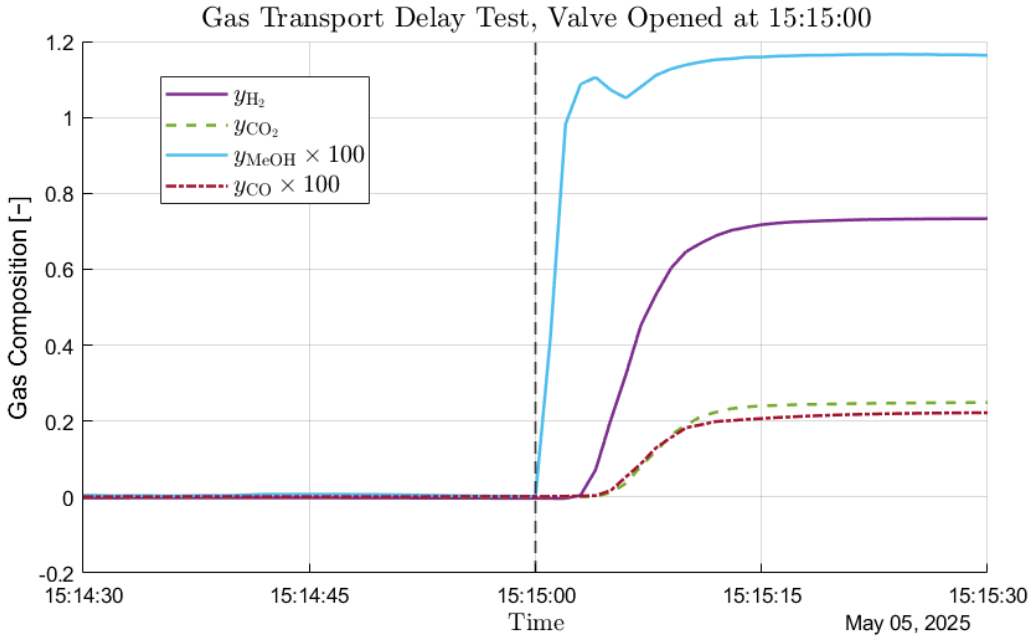

Figure 4.6: Gas transport delay from the sampling point (just after the reformer outlet) to the gas analysis unit. The dotted vertical line indicates when the valve was opened.

The data was sampled at a frequency of 1 Hz, limiting the resolution of the delay estimation to one-second intervals. According to the results, the methanol sensor responds first, showing a change within the same second the valve was opened. This rapid response is likely due to its placement upstream of the water condenser, allowing for quicker detection. The H_2 signal shows a delayed response, appearing approximately 3–4 seconds after the valve opening. The CO and CO_2 concentrations change after approximately 5–6 seconds. Since these two gases are measured using the same detector, their synchronized response is expected. The test also indicates that it takes approximately 20 seconds for the response of all the composition measurements to stabilize.

Total Reformer Flow Delay Estimation

Figure 4.7 shows the result of a test where the feed flow rate of the methanol/water mixture was changed, and the gas composition at the outlet was monitored.

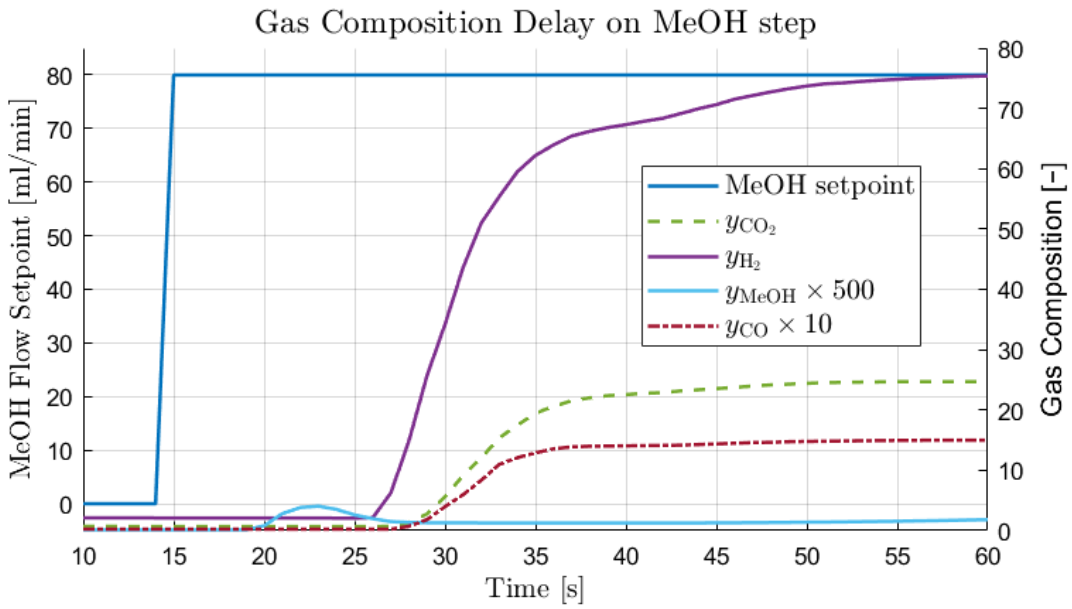

Figure 4.7: Total delay from feed flow rate change to observable change in gas composition.

The methanol concentration changes approximately 5–6 seconds after the step. The H_2 signal follows at around 12 seconds, while CO and CO_2 signals show changes after 14–15 seconds. This progression reflects the response times of the individual sensors, as observed in the previous test. Subtracting these sensor delays indicates that it takes around 5–6 seconds for the feed flow change to influence the reformer output, representing the internal dynamic delay of the reformer and evaporator.

Pump-to-Reformer Flow Delay Estimation

Using the data from the same flow step test, it is also possible to estimate the delay from the pump to the reformer inlet. Figure 4.8 shows the delay between a step change in flow rate (from 0 to 80 ml/min) and the corresponding change in temperature measured immediately after the evaporator.

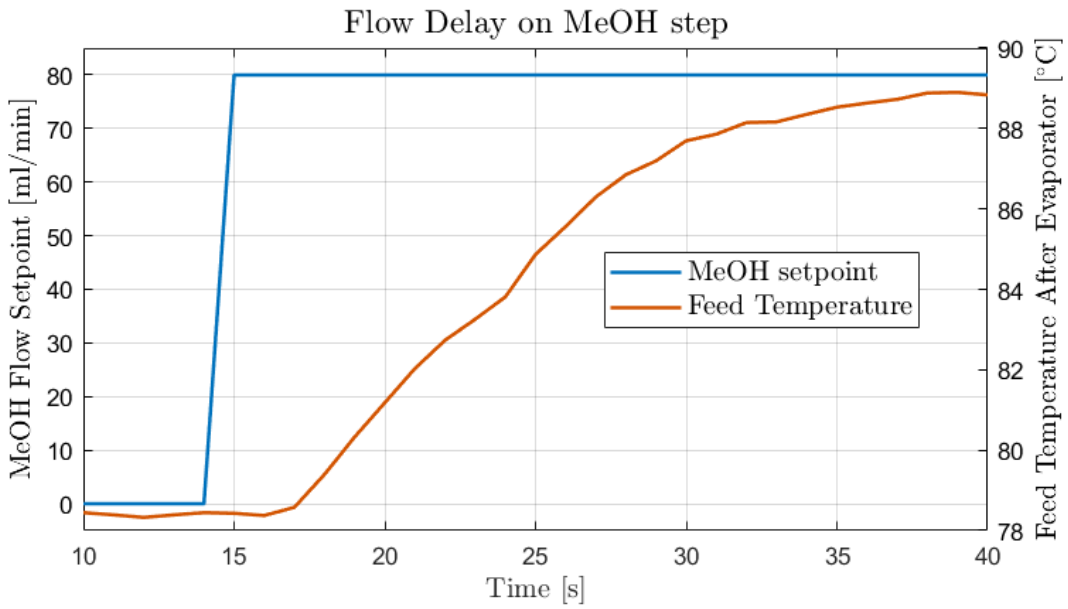

Figure 4.8: Delay between pump flow change and observed temperature increase after the evaporator.

The results show a delay of approximately 2–3 seconds before the change is detected by the temperature sensor. This delay corresponds to the transport time through the pump and piping to the evaporator outlet. Figure 4.9 illustrates the delay results and shows the estimated time it takes for a change in flow from 0-80 ml/min to propagate throughout the reformer system.

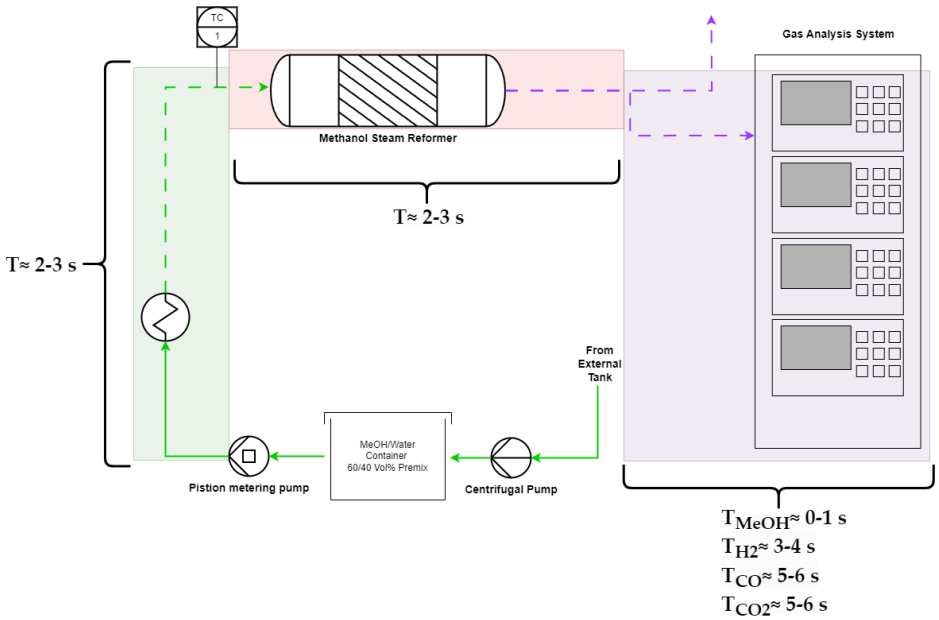

Figure 4.9: Illustration of the reformer system and the flow timings associated with a flow step from 0 to the max of 80 ml/min

4.3 Reformer Gas Composition Characterization

The amount of fuel to be supplied to the reformer is based on the H_2 required by the fuel cell stack. For this purpose a characterization of the gas composition under different operational conditions is needed. This section presents the results of the gas composition characterization with a focus on the H_2 and CO_2 composition. The investigation is additionally used in Section 4.3.3 with a focus on methanol and CO in the reformate gas. The characterization experiment was carried out at temperature intervals of 10°C, ranging from 200 to 260°C. At each temperature level, the feed flow rate was varied in 10 ml/min increments from 0 to 80 ml/min. This systematic variation allows for mapping the reformate composition across a range of realistic operating conditions.

4.3.1 Characterization Test Design

To design an effective test sequence for investigating the gas composition of the reformer, it was first necessary to understand the system's settling time. Therefore, an initial study was conducted to evaluate the dynamic response of the reformer. The primary indicators used to assess when the reformer reaches steady state are the internal temperatures of the catalyst bed and the reformate gas composition. These variables represent the slowest dynamics in the system and are thus the most suitable for determining the time to reach steady-state conditions.

For the investigation, two step-change experiments were performed:

1. The feed flow rate was increased from 10 to 20 ml/min while maintaining the reformer oil temperature at 230 °C.
2. The reformer oil set temperature was increased from 230 to 240 °C while keeping the feed flow rate constant at 20 ml/min.

These experiments provided insight into the time required for the gas composition and internal temperatures to stabilize following a change in either operation parameter, and thereby informed the settling times used in the subsequent gas composition characterization tests. The dynamic responses of the internal catalyst bed temperatures and the reformate gas composition to step changes are shown in Figure 4.10.

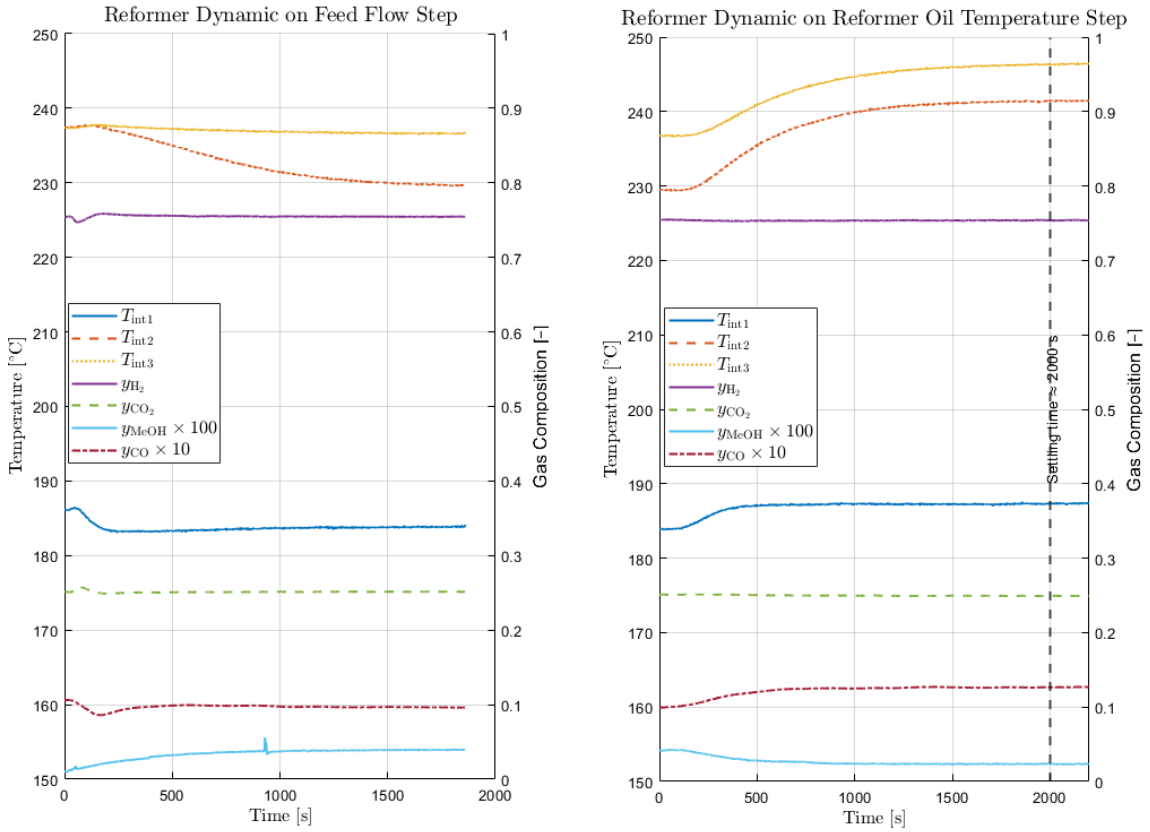

Figure 4.10: Response of the reformer catalyst bed temperatures and gas composition to step changes. The left subplot shows the system's response to a feed flow rate step from 10 to 20 ml/min at a constant reformer oil temperature of 230 °C. The right subplot displays the response to a step increase in reformer oil temperature from 230 to 240 °C with the feed flow held constant at 20 ml/min.

From Figure 4.10 it can be seen that the generally slowest dynamics are the internal catalyst temperatures and at the slowest they take approximately 2000 seconds to stabilize. Based on this investigation, a conservative settling time of 2000 seconds was chosen for all steps in the gas composition characterization test sequence, ensuring that steady-state conditions were reached before each measurement. After reaching steady state, a logging program built in Python logs the gas composition measurements over a duration of 200 seconds. The final reported values used in the analysis are calculated as the average of these 200 seconds of data, providing a more robust and noise-filtered representation of the steady-state condition. The standard deviation over the same period is also recorded and presented in Appendix A to quantify measurement variability.

4.3.2 Gas Composition Characterization Results

The results of the gas composition characterization experiments are presented below as both contour plots and tabulated matrices. These describe how key components of the reformate gas, namely H_2, CO_2, methanol, and CO, respond to varying reformer oil temperatures and feed flow rates.

Figures 4.11 and 4.12 show the contour plots for H_2 and CO_2 concentrations, while Tables 4.1 and 4.2 provide the corresponding raw values used to construct these visualizations.

Table 4.1: H_2 molar concentration in the reformate gas as a function of reformer oil temperature and feed flow rate.

Flow Rate [ml/min]	**Reformer Temperature [°C]**						
	200	210	220	230	240	250	260
80	0.7068	0.7113	0.7177	0.7250	0.7362	0.7439	0.7486
70	0.7084	0.7153	0.7234	0.7364	0.7409	0.7487	0.7526
60	0.7105	0.7191	0.7283	0.7389	0.7449	0.7550	0.7525
50	0.7153	0.7257	0.7343	0.7449	0.7484	0.7521	0.7536
40	0.7239	0.7325	0.7417	0.7489	0.7512	0.7536	0.7541
30	0.7328	0.7409	0.7475	0.7516	0.7533	0.7542	0.7541
20	0.7425	0.7493	0.7521	0.7539	0.7539	0.7542	0.7540
10	0.7510	0.7566	0.7545	0.7550	0.7534	0.7539	0.7540

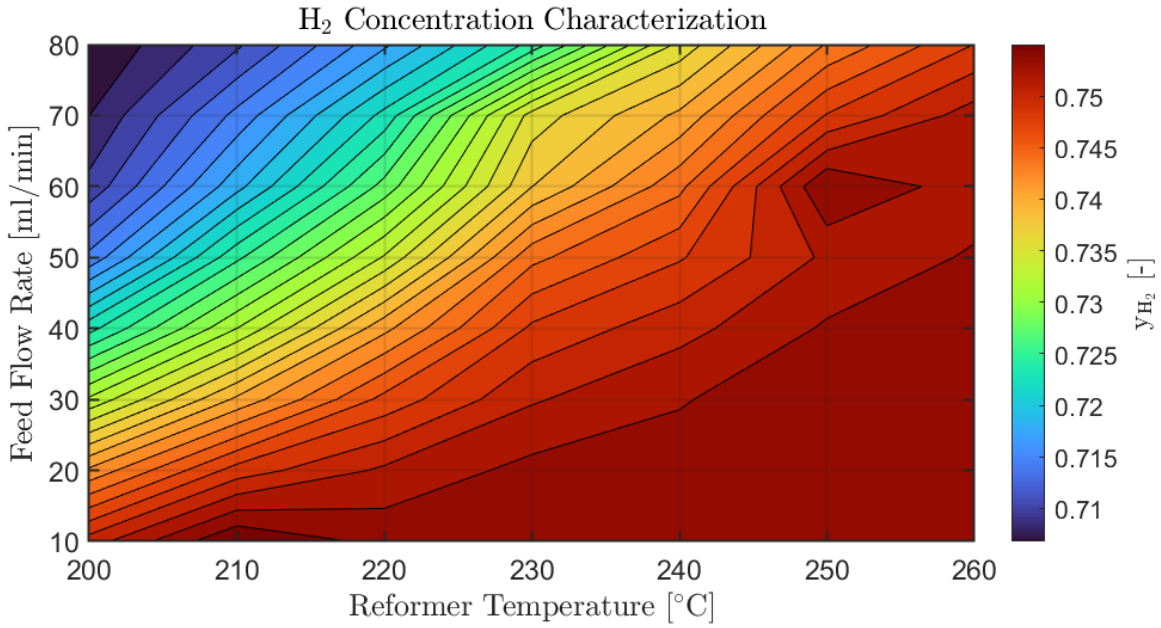

Figure 4.11: Mole fraction of H_2 present in reformate gas under varying feed flow rates and reformer temperatures.

Figure 4.11 shows that the concentration of H_2 in the reformate gas tends to increase with higher reformer temperatures and decrease with higher feed flow rates. This trend inversely mirrors the behavior of methanol slip, as discussed in the next section. A likely explanation is that elevated temperatures promote more complete conversion of methanol into hydrogen through steam reforming reactions, resulting in a higher H_2 yield and lower residual methanol content. However, this increase in conversion is accompanied by a rise in CO concentration though less pronounced than the rise in H_2. Since CO is an undesired byproduct due to its harmful effects on fuel cell catalysts, this introduces a trade-off in gas quality when operating at higher reformer temperatures.

Table 4.2: CO_2 concentration in the reformate gas as a function of reformer oil temperature and feed flow rate.

Flow Rate [ml/min]	**Reformer Temperature [°C]**						
	200	210	220	230	240	250	260
80	0.24560	0.24620	0.24720	0.24900	0.25270	0.24970	0.25050
70	0.24620	0.24720	0.24820	0.25000	0.25280	0.25000	0.25050
60	0.24670	0.24780	0.24900	0.25150	0.25260	0.25070	0.24910
50	0.24730	0.24910	0.24990	0.25230	0.25260	0.25040	0.24820
40	0.24880	0.25050	0.25080	0.25210	0.25220	0.24970	0.24700
30	0.24970	0.25190	0.25130	0.25220	0.25180	0.24880	0.24570
20	0.25270	0.25380	0.25180	0.25230	0.25100	0.24790	0.24470
10	0.25440	0.25320	0.25170	0.25110	0.25060	0.24760	0.24430

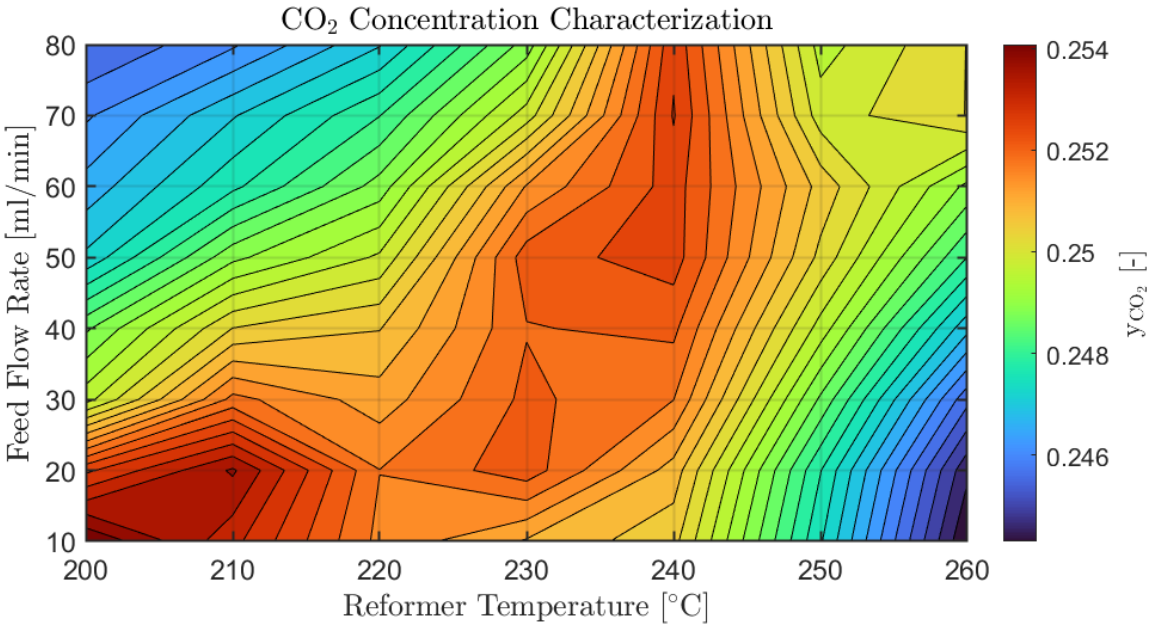

Figure 4.12: Mole fraction of CO_2 present in reformate gas under varying feed flow rates and reformer temperatures.

The contour plot of CO_2 concentration in the reformate gas reveals only a minor trend, with the highest concentrations occurring at low feed flow rates and low reformer temperatures. However, the absolute difference between the minimum and maximum measured volume fraction is approximately 0.009, corresponding to a relative variation of about 4%. This variation is comparable to the standard deviation observed in several of the measurements, particularly in regions with higher CO_2 concentrations. As such, it is likely that a portion of the observed variation is attributable to measurement noise or uncertainty. The standard deviations associated with the gas composition measurements are provided in A.

The resulting H_2 data matrix is used as a lookup table in the reformer model. Given a desired hydrogen molar flow rate, the lookup table is used to estimate the feed flow rate required to produce that amount of hydrogen, based on the current reformer temperature.

The gas composition characterization also included measurements for the methanol slip and CO in the reformate gas as a function of feed flow rate and reformer oil set temperature. These results will be used in the next section to investigate the possibility of regulating these undesirable reformate gas components while still producing the necessary H_2

4.3.3 Methanol Slip and Carbon Monoxide Control

In a PhD thesis by [Sahlin, 2016], a concept was proposed and simulated that explored the potential for controlling the reformate gas composition by adjusting the reformer oil temperature. The central idea is that, with sufficient characterization of the reformer's gas output under varying operating conditions, it becomes possible to influence the levels of methanol slip and CO in the reformate gas through temperature regulation alone while still producing the required H_2. While Sahlin's work validated this concept through simulation-based studies, the present work aims to demonstrate its feasibility in a real-life system. By leveraging real-time gas composition measurements from the HiL reformer test bench and actively controlling the oil temperature, this project investigates whether gas composition shaping, specifically targeting methanol slip and CO concentration, can be achieved under experimental conditions. Additionally the expanded control over the reformate gas could expand on the testing possibilities using the laboratory setup.

The measured methanol slip across the characterization is presented in Table 4.3, with its corresponding contour plot shown in Figure 4.13. The results clearly show that methanol slip decreases with increasing reformer temperature and decreasing feed flow rate. This behavior aligns with expectations, as higher temperatures promote more complete reforming of methanol, reducing the residual slip in the reformate gas.

Table 4.3: Methanol slip in the reformate gas as a function of reformer oil temperature and feed flow rate.

Flow Rate	**Reformer Temperature [°C]**						
[ml/min]	200	210	220	230	240	250	260
80	0.02910	0.02340	0.01800	0.01270	0.00830	0.00540	0.00310
70	0.02660	0.02060	0.01530	0.01000	0.00640	0.00390	0.00210
60	0.02360	0.01760	0.01260	0.00760	0.00480	0.00260	0.00120
50	0.01980	0.01400	0.00940	0.00510	0.00310	0.00140	0.00057
40	0.01550	0.01050	0.00640	0.00350	0.00180	0.00060	0.00018
30	0.01120	0.00670	0.00380	0.00230	0.00079	0.00016	0.00005
20	0.00640	0.00350	0.00160	0.00097	0.00031	0.00004	0.00001
10	0.00200	0.00040	0.00020	0.00019	0.00007	0.00001	0.00000

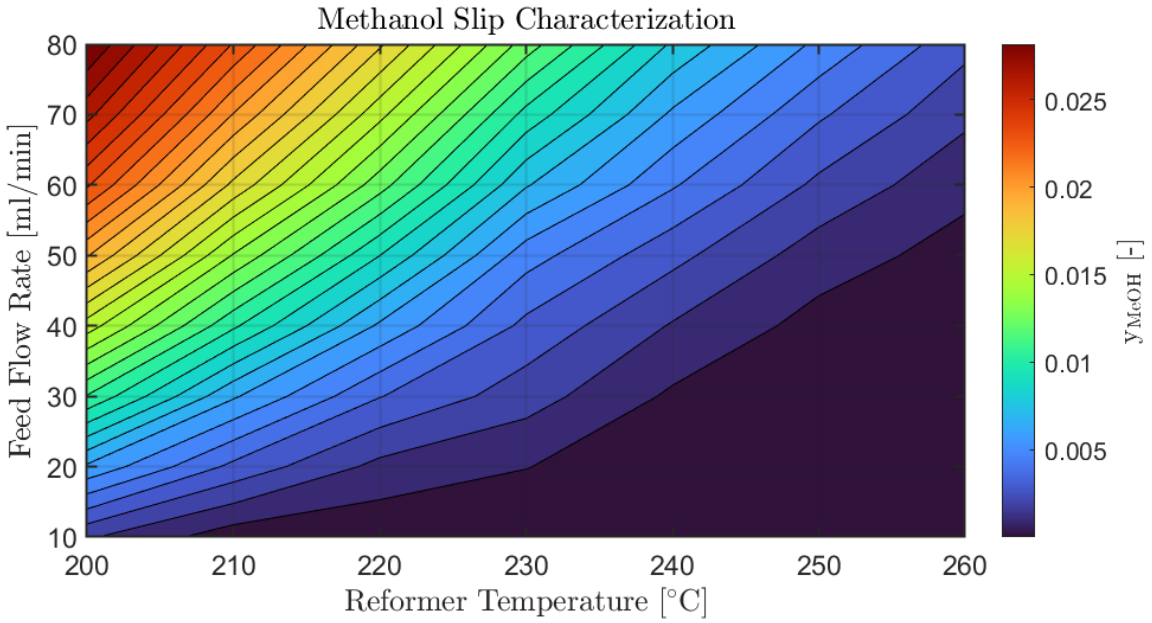

Figure 4.13: Mole fraction of methanol slip present in reformate gas under varying feed flow rates and reformer temperatures.

In contrast to methanol slip, the CO concentration increases with increasing reformer temperature and decreasing feed flow rate. Table 4.4 and Figure 4.14 illustrate this trend. This opposing behavior creates a trade-off between minimizing methanol slip and limiting CO formation—both of which are critical to fuel cell performance and lifetime.

Table 4.4: CO concentration in the reformate gas as a function of reformer oil temperature and feed flow rate.

Flow Rate	**Reformer Temperature [°C]**						
[ml/min]	200	210	220	230	240	250	260
80	0.00071	0.00100	0.00160	0.00250	0.00400	0.00600	0.00850
70	0.00080	0.00120	0.00190	0.00300	0.00490	0.00720	0.00990
60	0.00095	0.00150	0.00240	0.00390	0.00620	0.00860	0.01130
50	0.00120	0.00190	0.00310	0.00500	0.00750	0.01000	0.01280
40	0.00150	0.00260	0.00430	0.00640	0.00890	0.01160	0.01440
30	0.00220	0.00380	0.00580	0.00750	0.01030	0.01310	0.01610
20	0.00360	0.00530	0.00710	0.00860	0.01160	0.01460	0.01750
10	0.00500	0.00660	0.00850	0.01000	0.01300	0.01550	0.01790

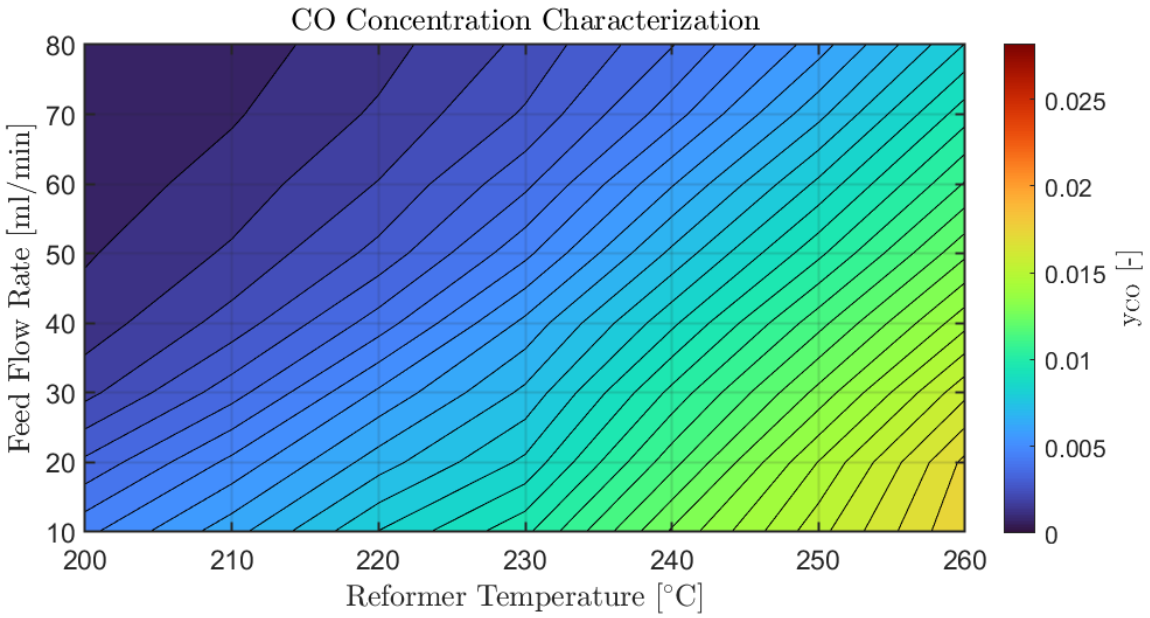

Figure 4.14: Mole fraction of CO present in reformate gas under varying feed flow rates and reformer temperatures.

This inverse relationship between methanol slip and CO concentration in response to changes in reformer temperature, combined with the relatively limited sensitivity of the H_2 concentration, provides a basis for targeted shaping of the reformate gas composition. By tuning the reformer oil temperature within a known operating range, it becomes possible to influence the levels of methanol and CO in the reformate to suit specific system requirements.

4.3.4 Methanol slip and Carbon Monoxide Control Implementation and Validation

The composition control is implemented in the LabVIEW program running on the host computer coupled with the reformer test bench. This host is connected to the mid-level control layer, using the variables listed in Appendix in Table D.1 and D.2. To enable composition shaping without access to real-time gas analysis, the experimentally obtained gas composition matrices for methanol slip and CO concentration are used as static lookup tables. These matrices are first interpolated using a cubic spline method to increase their resolution, so that feed flow rates are defined in 5 ml/min increments and reformer oil temperatures in 5 °C increments. The resulting matrices are imported into the LabVIEW program as 2D arrays.

In the implementation, the current feed flow setpoint is used to extract the relevant row from both the methanol and CO matrices, resulting in two vectors corresponding to different reformer temperatures. A loop is then executed across the allowed temperature range to evaluate all possible values of methanol slip and CO concentration for the current flow rate. Based on the selected control mode, "constrain CO minimize methanol" or "constrain methanol minimize CO", the program checks whether each temperature entry satisfies the constraint. If the constraint is met, the corresponding value of the objective variable is stored. After the loop completes, the program selects the reformer temperature that yields

the lowest value of the objective variable while remaining within the defined constraint. This temperature is then output as the new setpoint for the reformer oil temperature.
The logic enables autonomous control of gas composition characteristics, with a balance between minimizing one component while ensuring the other remains below a set limit. This approach offers an effective method of reformate gas shaping using only static characterization data, without relying on live gas composition feedback.

Composition Control Validation

An experiment was carried out to validate the functionality of the implemented gas composition control. The objective was to confirm both that the control logic activates as intended and that it can adjust the reformate gas composition in accordance with the estimated target values. Three tests were conducted under different conditions. The first was a baseline test with no composition control applied, maintaining a fixed reformer oil temperature of 260 °C. The second test enabled control with a constraint limiting the maximum CO concentration to 10000 ppm (1 Vol%), while minimizing methanol slip. In the third test, the control was active with a constraint on maximum methanol slip at 10000 ppm, while targeting a minimization of CO concentration.

In all tests, the feed flow rate was stepped through three values: 20, 60, and 40 ml/min. At each step, the system was allowed to stabilize before continuing to the next flow setpoint.

Figure 4.15 shows the controllable variables and the corresponding gas composition during the baseline test. The top graph displays the reformer temperature setpoint, the actual oil temperature, and the feed flow setpoint. The bottom graph shows the measured gas composition values, specifically the methanol slip and CO concentration. These plots together illustrate how the system responds to setpoint changes while at a constant reformer oil temperature setpoint.

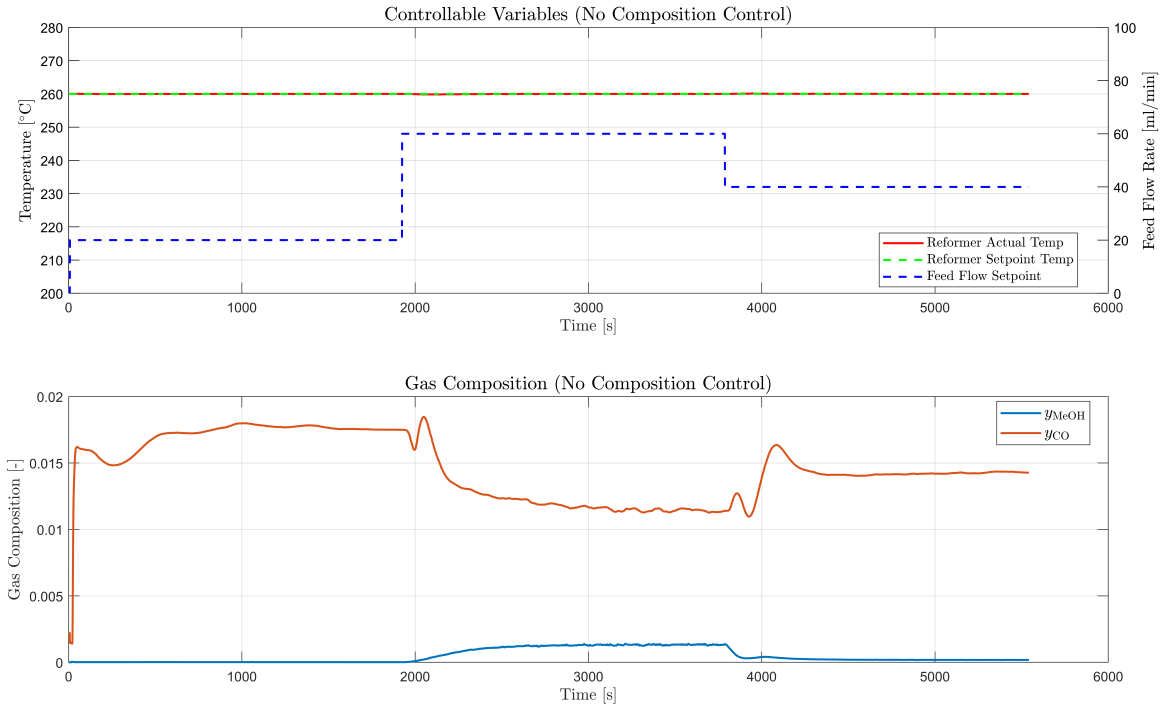

Figure 4.15: Time series of gas composition measurements during the baseline test without composition control. The figure shows the mole fractions of methanol slip and CO in the reformate gas while the system operates under a fixed reformer oil temperature setpoint of 260°C. The step changes in feed flow rate (20, 60, and 40 ml/min) are reflected in the changes in gas composition, demonstrating the steady state composition in the absence of active composition shaping.

Figure 4.16 shows the result for the test minimizing CO with a maximum allowed methanol concentration of 10 000ppm (1 Vol%).

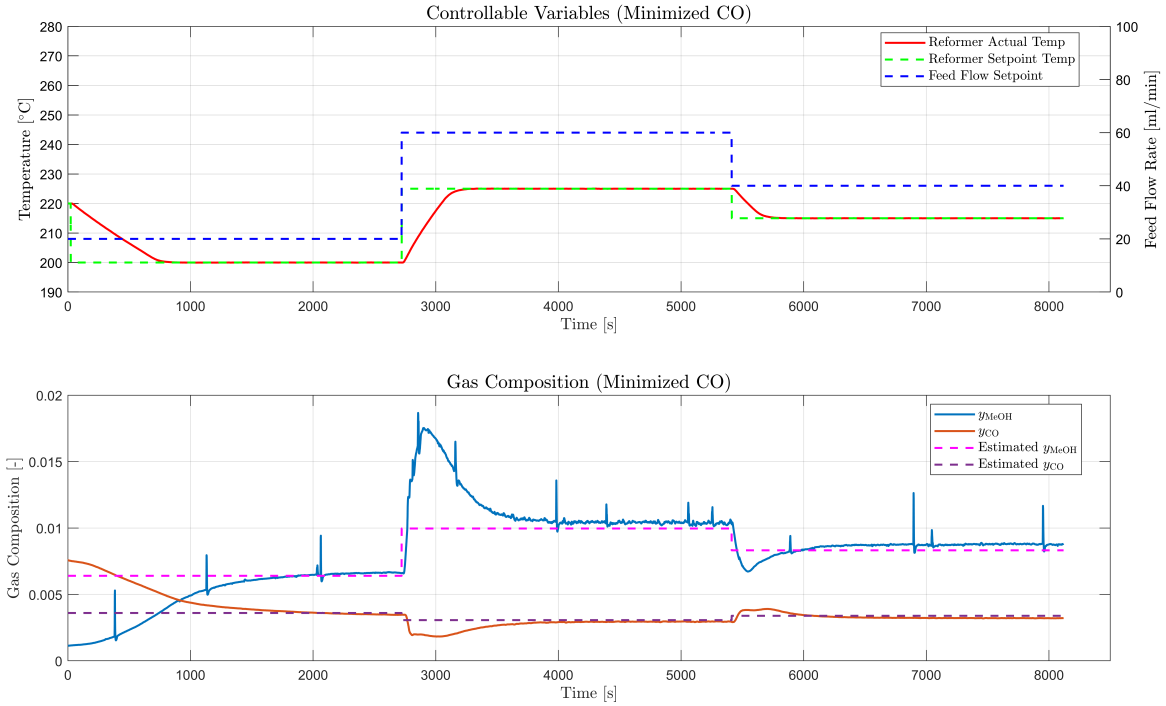

Figure 4.16: Time series of gas composition measurements during the composition control test with CO minimization. The control algorithm attempts to maintain the methanol slip below a threshold of 10 000 ppm (1 Vol%) while minimizing the CO concentration. The reformer temperature is adjusted at each feed flow setpoint (20, 60, and 40 ml/min) to satisfy the constraint and reduce CO levels. The plotted estimated values correspond to the predicted gas composition from the characterization model based on current operating conditions.

Figure 4.16 demonstrates that the control algorithm is effective at both minimizing the CO concentration and keeping the methanol slip below the defined threshold. A peak in methanol slip is observed around 3000 seconds, which is attributed to the slow response of the reformer oil temperature. Once the temperature stabilizes, the methanol slip converges toward the estimated value of 9950 ppm, ultimately reaching a measured value of 10350 ppm. Overall, the results show that in CO minimization mode, the controller performs well, both methanol and CO estimates closely match the actual measured values, confirming the reliability of the model-based composition shaping strategy.

Figure 4.17 shows the result for the test minimizing methanol with a maximum allowed CO concentration of 10 000ppm (1 Vol%).

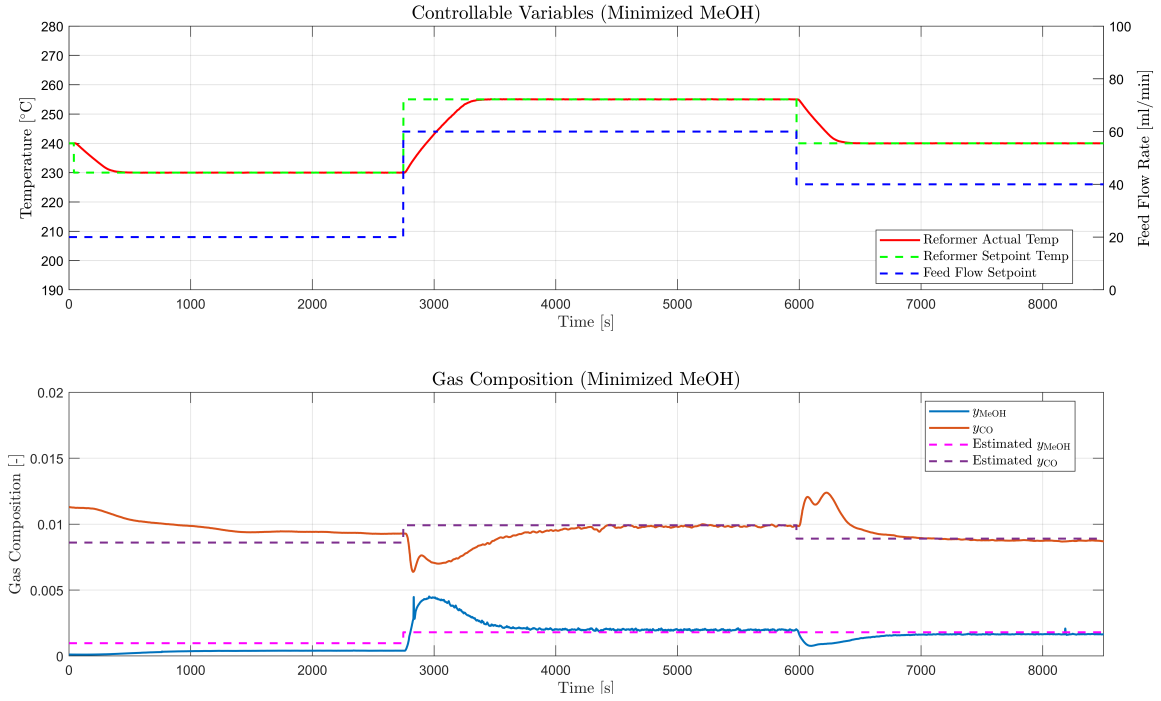

Figure 4.17: Time series of gas composition measurements during the composition control test with methanol minimization. The control algorithm attempts to maintain the CO concentration below a threshold of 10 000 ppm (1 Vol%) while minimizing the methanol slip. The step changes in feed flow rate (20, 60, and 40 ml/min) result in adjusted reformer temperature setpoints to meet the specified constraint. The plotted estimated values correspond to the predicted gas composition from the characterization model based on current operating conditions.

Compared to the CO minimization test, the performance of the methanol minimization test is less accurate during the low feed flow rate step. In this region, the measured values deviate more noticeably from the estimated composition. However, at higher flow rates, the agreement between the estimated and measured values improves significantly. The control algorithm also demonstrates the ability to maintain CO concentrations below the 10,000 ppm threshold, except during brief transients where the reformer temperature has not yet stabilized. These results suggest that the control strategy is more effective under higher flow conditions when attempting to minimize methanol.

The results presented above indicate that the gas composition stabilizes within approximately 1000 seconds following a step change in the feed flow setpoint. This stabilization period is primarily dictated by the slow thermal response of the reformer oil loop, as the reformer oil temperature dynamics are the main limiting factor in the system's overall response time. The observed settling time corresponds to a step change of 40 ml/min, from 20 ml/min to 60 ml/min, representing approximately half of the test bench's operational flow range. Extrapolating from this result, it can be estimated that a full-range step change (e.g., from 10 to 80 ml/min) may require up to 2000 seconds for the gas composition to fully stabilize.
Table 4.5 lists the results obtained from the three tests. It lists the measured values for

each flow rate step together with the estimated/minimized values and the corresponding absolute difference and relative difference with the relative difference calculated as shown in 4.1

$$Rel.Diff. = \frac{|MeasuredValue - EstimatedValue|}{MeasuredValue} \tag{4.1}$$

Table 4.5: Measured and estimated gas composition values for methanol slip and CO during the three validation tests at different feed flow rates. The baseline test was conducted at a fixed reformer oil temperature of 260 °C without composition control. In the two control tests, the reformer temperature was dynamically adjusted to either minimize methanol slip under a CO constraint (10,000 ppm) or minimize CO under a methanol constraint (10,000 ppm). Both absolute and relative differences between measured and estimated values are listed to evaluate control accuracy.

Flow Rate [ml/min]	Quantity	Baseline @260°C	Min. MeOH (10,000 ppm CO)	Min. CO (10,000 ppm MeOH)
20	MeOH Measured (Estimated)	15	401 (970)	6663 (6400)
	Abs. Diff. MeOH Rel. Diff. MeOH	–	569 142%	263 3.95%
	CO Measured (Estimated)	17532	9269 (8600)	3459 (3600)
	Abs. Diff. CO Rel. Diff. CO	–	669 7.22%	141 4.08%
40	MeOH Measured (Estimated)	181	1640 (1800)	8764 (8318)
	Abs. Diff. MeOH Rel. Diff. MeOH	–	160 9.76%	446 5.09%
	CO Measured (Estimated)	14337	9241 (8900)	3204 (3387)
	Abs. Diff. CO Rel. Diff. CO	–	341 3.69%	183 5.71%
60	MeOH Measured (Estimated)	1332	1981 (1800)	10353 (9962)
	Abs. Diff. MeOH Rel. Diff. MeOH	–	181 9.14%	391 3.78%
	CO Measured (Estimated)	11318	9891 (9912)	2945 (3062)
	Abs. Diff. CO Rel. Diff. CO	–	21 0.2123%	117 3.97%

The results show that the implementation yields significant control of the reformate gas composition. The composition control is built directly into the reformer test bench and can be accessed both through the host computer GUI and remotely via the DTA-based communication system, as described earlier. This dual-access design extends the usefulness of the implementation beyond the scope of the current project. Specifically, the reformer test bench can now operate as a flexible reformate gas generator, capable of producing gas mixtures with tailored and known CO, and methanol concentrations. This enhanced func-

tionality makes it a valuable tool for broader experimental purposes, particularly where reformate gases with realistic compositions are needed. In such contexts, using authentic reformate gas may yield more representative results than those obtained with synthetically mixed dry gas compositions. The increased control over the reformate gas composition also opens new possibilities for targeted experimental studies. For instance, it enables more accurate investigations into the poisoning effects of CO and methanol slip on fuel cells, which are critical factors in HT-PEMFC system durability. Additionally, the system could be used to study the long-term effects of repeated start-up and shut-down cycles in methanol-reformed fuel cell systems.

To further support long-term utility, an additional feature has been implemented in the LabVIEW program on the host computer. This feature continuously compares the measured gas composition values from the gas analysis unit with the estimated values derived from the characterization experiment. Over time, a growing discrepancy between measured and estimated compositions may indicate degradation of the reformer. This diagnostic functionality lays the groundwork for future health monitoring by enabling the detection of gradual performance shifts. If these deviations are logged systematically, they could also provide valuable insights into the reformer's degradation rate.

The preceding section presented the investigations conducted on the reformer test bench, including its control architecture, DTA integration, and the implementation of a novel gas composition control strategy. The following section introduces the calculations and estimations developed to interface the test bench with the broader DTA-based system framework, enabling real-time integration with other modular components.

4.4 Real-time Hydrogen Flow Estimation and Feed Flow Calculation

This section describes calculations used to predict the feed flow rate required to meet the H_2 demand of the fuel cell system. These calculations forms part of the reformer module, which operates in real time within the HiL framework.

The reformer module receives an input signal representing the instantaneous H_2 demand from the fuel cell module. Based on this input and the current temperature measured in the reformer oil heating loop, the model calculates the appropriate feed flow rate setpoint for the methanol/water mixture pump. This calculation is based on the result matrices obtained from the reformer characterization experiment, which relate reformer temperature and feed flow rate to the resulting H_2 concentration in the reformate gas. These matrices enable the model to estimate the required feed flow setpoint to meet the dynamic hydrogen demand during system operation.

In parallel, the model continuously reads the real-time gas composition of the reformate, measured by the gas analysis unit connected to the physical reformer. Using this composition data and the applied feed flow setpoint, the model estimates the molar flow rates of each component in the reformate gas, including H_2, CO_2, CO, and methanol slip. This information is then transmitted for use in the fuel cell module.

4.4.1 Feed Flow Setpoint Calculation

The gas analysis unit used to measure the composition of the reformate gas measures the dry volume fractions of CO, CO_2 and H_2, while the volume fraction of methanol is measured wet. The volume fraction of water is not measured at all. Furthermore the flow rate of gas leaving the reformer is not measured. These factors complicate the calculation of the molar flow rate of the hydrogen being produced in the reformer.

The methanol/water mixture volume flow rate is controlled by the pump and is assumed to be accurate to the set point, meaning that the inlet flow rate is known. The conversion from volume flow rate to molar flow rate is shown in Equation (4.2).

$$\dot{V}_{\text{in}} = \frac{\dot{n}_{\text{MeOH,in}}\ MW_{\text{MeOH}}}{\rho_{\text{MeOH}}} + \frac{\dot{n}_{\text{H2O,in}}\ MW_{\text{H2O}}}{\rho_{\text{H2O}}} \quad \left[\frac{\text{m}^3}{\text{s}}\right] \tag{4.2}$$

- $\dot{V}_{\text{in}}$: Volume flow rate of Liquid methanol/water mixture [m^3/s]
- $\dot{n}_{\text{MeOH,in}}$: Molar flow rate of methanol entering the reformer [mol/s]
- $\dot{n}_{\text{H2O,in}}$: Molar flow rate of water entering the reformer [mol/s]
- $MW_{\text{MeOH,in}}$: Molar weight of methanol [kg/mol]
- $MW_{\text{H2O,in}}$: Molar weight of water [kg/mol]
- $\rho_{\text{MeOH,in}}$: Density of liquid methanol [kg/m^3]
- $\rho_{\text{H2O,in}}$: Density of liquid water [kg/m^3]

The S/C ratio is 1.5, which for the methanol/water mixture means that the molar ratio of water to methanol is 1.5. Equation (4.2) can therefore be rewritten as shown in Equation (4.3).

$$\dot{V}_{\text{in}} = \frac{\dot{n}_{\text{MeOH,in}}\ MW_{\text{MeOH}}}{\rho_{\text{MeOH}}} + 1.5\ \frac{\dot{n}_{\text{MeOH,in}}\ MW_{\text{H2O}}}{\rho_{\text{H2O}}} \quad \left[\frac{\text{m}^3}{\text{s}}\right] \tag{4.3}$$

The molar flow rates of methanol and water are therefore calculated as shown in equation (4.4).

$$\dot{n}_{\text{MeOH,in}} = \frac{\dot{V}_{\text{in}}}{2.5\left(\frac{MW_{\text{MeOH}}}{\rho_{\text{MeOH}}} + \frac{MW_{\text{H2O}}}{\rho_{\text{H2O}}}\right)} \quad \left[\frac{\text{mol}}{\text{s}}\right] \tag{4.4}$$

$$\dot{n}_{\text{H2O,in}} = 1.5\ \dot{n}_{\text{MeOH,in}} \quad \left[\frac{\text{mol}}{\text{s}}\right]$$

A series of element balances are then used to find the molar flow rates of components of the reformed gas. Since the only carbon atoms entering the reformer is bound as a single carbon atom in the methanol molecules, the molar flow rate of carbon entering the reformer is the same as the molar flow rate of methanol. One oxygen atom is bound in both the methanol and water molecule, while four hydrogen atoms are bound in the methanol molecule and two hydrogen atoms are bound in the water molecule. The molar flow rates of each of the three elements entering the reformer are therefore:

$$\dot{n}_{\text{C,in}} = \dot{n}_{\text{MeOH,in}} \quad \left[\frac{\text{mol}}{\text{s}}\right] \tag{4.5}$$

$$\dot{n}_{\text{O,in}} = \dot{n}_{\text{MeOH,in}} + \dot{n}_{\text{H2O,in}} \quad \left[\frac{\text{mol}}{\text{s}}\right]$$

$$\dot{n}_{\text{H,in}} = 4\ \dot{n}_{\text{MeOH,in}} + 2\ \dot{n}_{\text{H2O,in}} \quad \left[\frac{\text{mol}}{\text{s}}\right]$$

- $\dot{n}_{\text{C,in}}$: Molar flow rate of carbon atoms entering the reformer [mol/s]
- $\dot{n}_{\text{O,in}}$: Molar flow rate of oxygen atoms entering the reformer [mol/s]
- $\dot{n}_{\text{C,in}}$: Molar flow rate of hydrogen atoms entering the reformer [mol/s]

Assuming only pure water is condensed out of the reformed gas, the molar flow rate of carbon atoms is constant through the process. The molar flow rate of carbon atoms, can together with molar fraction measurements of CO, CO_2 and methanol, be used to calculate the total dry molar flow rate as shown in Equation (4.6).

$$\frac{\dot{n}_{\text{dry,out}}}{\dot{n}_{\text{C,out}}} = \frac{1}{y_{\text{CO,out}} + y_{\text{CO2,out}} + y_{\text{MeOH,out}}} \quad [\text{-}] \tag{4.6}$$

- $\dot{n}_{\text{dry,out}}$: Molar flow rate of dry gas leaving the reformer [mol/s]
- $\dot{n}_{\text{C,out}}$: Molar flow rate of hydrogen atoms leaving the reformer [mol/s]
- $y_{\text{CO,out}}$: molar fraction of CO leaving the reformer [-]
- $y_{\text{CO2,out}}$: molar fraction of CO2 leaving the reformer [-]
- $y_{\text{MeOH,out}}$: molar fraction of methanol leaving the reformer [-]

While the molar fraction of CO and CO_2 are both measured dry, The molar fraction of methanol is measured wet. This means that the molar fraction of methanol is lower than if it was measured in the dry gas, but since the methanol fraction is much lower than the others, this error is small. An element balance for the oxygen atoms can then be utilized to calculate the molar flow rate of the condensed water, as shown in Equation (4.7).

$$\dot{n}_{\text{H2O,out}} = \dot{n}_{\text{O,in}} - \dot{n}_{\text{CO,out}} - 2\ \dot{n}_{\text{CO2,out}} - \dot{n}_{\text{MeOH,out}} \quad \left[\frac{\text{mol}}{\text{s}}\right] \tag{4.7}$$

- $\dot{n}_{\text{H2O,out}}$: Molar flow rate of water entering the reformer [mol/s]
- $\dot{n}_{\text{CO,out}}$: molar flow rate of CO leaving the reformer [mol/s]
- $\dot{n}_{\text{CO2,out}}$: molar flow rate of CO_2 leaving the reformer [mol/s]
- $\dot{n}_{\text{MeOH,out}}$: molar flow rate of methanol leaving the reformer [mol/s]

The element balance for the hydrogen is then utilized to calculate the molar flow rate of hydrogen produced in the reformation reaction, as shown in Equation (4.8)

$$\dot{n}_{\text{H2,out}} = \frac{1}{2}\left(\dot{n}_{\text{H,in}} - 2\ \dot{n}_{\text{H2O,out}} - 4\ \dot{n}_{\text{MeOH,out}}\right) \quad \left[\frac{\text{mol}}{\text{s}}\right] \tag{4.8}$$

- $\dot{n}_{\text{H2,out}}$: Molar flow rate of hydrogen entering the reformer [mol/s]

The relationships described above are used both to determine the feed flow set point required by the reformer test bench and to estimate the molar flow rates of the individual components in the reformate gas. The feed flow setpoint is determined by the hydrogen demand from the fuel cell module and the current reformer oil loop temperature by using Table 4.6.

Table 4.6: Calculated hydrogen molar flow rate (mol/s) in the reformate gas as a function of reformer oil temperature and feed flow rate.

Flow Rate	Reformer Temperature [°C]						
[ml/min]	200	210	220	230	240	250	260
80	0.053	0.054	0.055	0.056	0.057	0.058	0.058
70	0.047	0.048	0.049	0.050	0.050	0.051	0.051
60	0.040	0.041	0.042	0.043	0.043	0.043	0.044
50	0.034	0.035	0.036	0.036	0.036	0.036	0.036
40	0.027	0.028	0.029	0.029	0.029	0.029	0.029
30	0.021	0.022	0.022	0.022	0.022	0.022	0.028
20	0.014	0.015	0.015	0.015	0.015	0.015	0.014
10	0.0073	0.0073	0.0073	0.0073	0.0073	0.0073	0.0072

This Table 4.6 is calculated by passing the values of Table 4.2, Table 4.3 and Table 4.4, through the calculations introduced in this section. To improve the granularity of the feed flow rate set point, the Table 4.6 is interpolated to a granularity of 2 ml/min for the feed flow rate and 2 °C for the temperature. In contrast to the calculation of the feed flow rate set point, the output molar flow rates of the reformate gas components are computed using the real-time measured gas composition and the actual applied feed flow rate.

Chapter 5

Full System Implementation and Validation

The system developed in this project consists of three primary modules: a reformer module, a fuel cell stack module, and a HWT module. These modules are designed to communicate with one another via the web-based communication system and are coordinated by a mid-level control layer. In addition, the system interfaces in real-time with a high-level EMS layer developed by [Xie et al., 2025].

5.1 Mid-Level Layer

The mid-level control layer serves as both a coordination hub and a user interface for setting system control parameters. Developed in LabVIEW, it receives all relevant transmissions from the individual modules and the high-level EMS layer. One of its primary functions is to receive the On/Off signal from the EMS, which indicates when the CHP system should begin or stop producing heat and power. Upon receiving a startup signal, the mid-level layer initiates the start-up sequence for both the reformer and fuel cell modules. It continuously monitors system parameters to determine when each module reaches its operational temperature—specifically, when the reformer is ready to produce hydrogen and the fuel cell is prepared to deliver power.

Once the reformer reaches its target temperature, the mid-level layer sets the feed flow rate to 10 ml/min and based on results from chapter 4.2 it waits for 60 seconds to allow the system to stabilize. It then commands the fuel cell module to begin ramping up power output to match the power reference provided by the upper EMS layer.

Whenever the EMS layer issues a new power reference, the mid-level layer transmits this updated demand to the fuel cell module. The fuel cell then calculates a new desired hydrogen molar flow rate, which is passed to the reformer module. Based on this requirement, the reformer's host PC computes a new feed flow rate and determines an updated reformer temperature setpoint, depending on whether the composition control algorithm is active.

When a shutdown signal is received from the EMS layer, the mid-level controller sets the temperature setpoints for the reformer and evaporator to 20 °C and triggers the fuel cell module's shutdown procedure. The startup and shutdown sequence for the fuel cell module is handled by the module itself, the mid-level only ensures that all modules have reached sufficient operational states.

A *Unified Modeling Language* (UML)-based diagram illustrating the mid-level control logic can be seen in figure 5.1

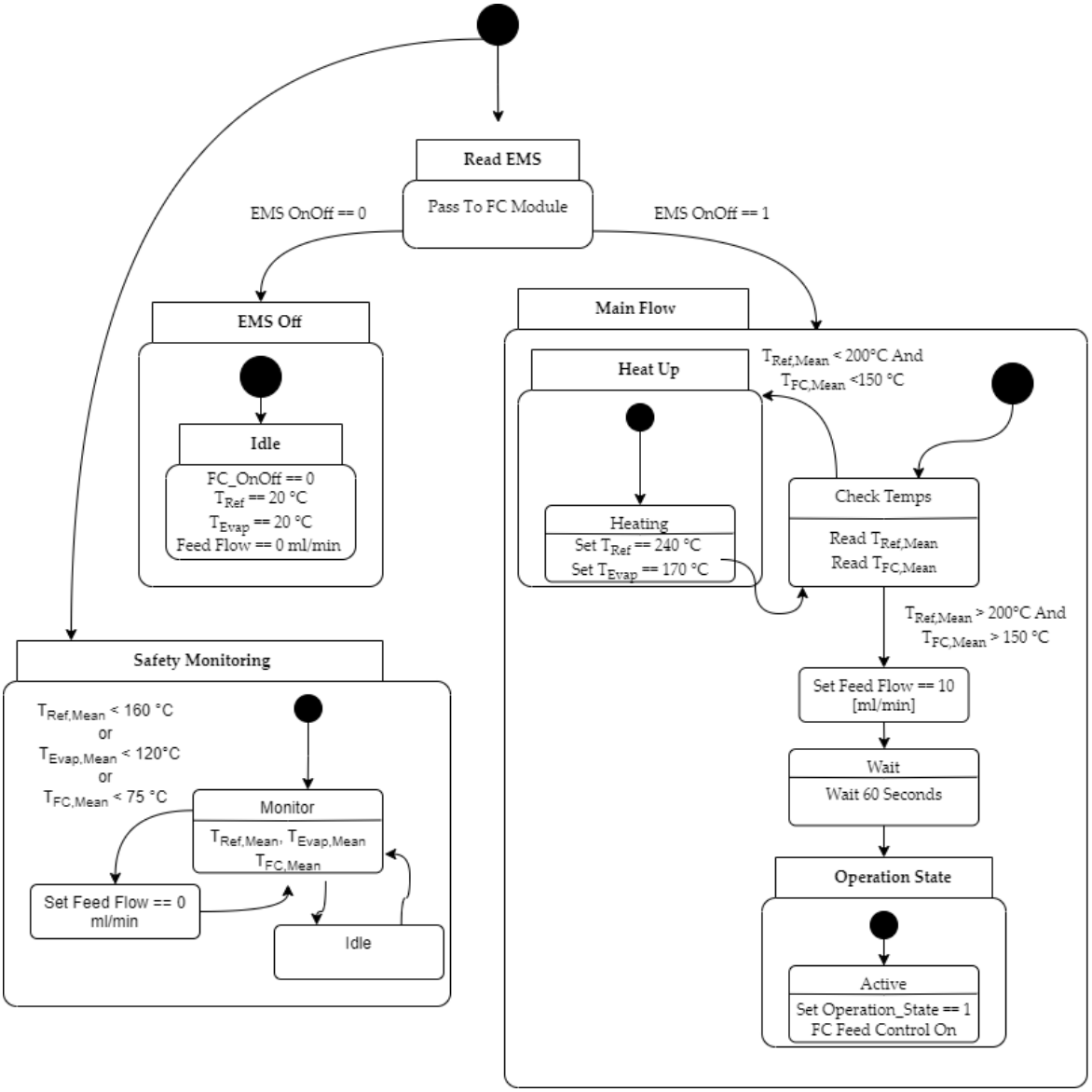

Figure 5.1: UML-based finite state diagram illustrating the mid-level control logic, including system startup, temperature checks, feed flow regulation, and continuous safety monitoring.

As previously mentioned, the LabVIEW program developed for the mid-level control layer also functions as a user interface for system monitoring and configuration. Screenshots of the interface panels are provided in Appendix B.

Through this interface, the user can control multiple parameters of both the reformer modules. For the reformer module, the user can remotely adjust the oil loop temperature setpoint, evaporator temperature setpoint, and feed flow rate. Additionally, the user has access to the gas composition control parameters, including setting the maximum allowable CO concentration when minimizing methanol slip, and the maximum allowable methanol concentration when minimizing CO. The interface also provides the ability to toggle between the two composition control modes or disable composition control entirely.

Beyond reformer-specific settings, the interface also includes a debug mode for higher-

layer Energy Management System (EMS) commands. This allows the user to emulate EMS behavior by setting On/Off signals, power reference values, and heat demand levels. These capabilities are especially useful during system validation, where controlled testing of dynamic interactions between modules is required.

An overview of all available control variables and their associated functionalities is provided in Table 5.1.

Table 5.1: Controllable variables accessible through the mid-level user interface.

Category	Variable Name	Description
Reformer Control	Reformer Oil Temp Setpoint	Desired temperature for the reformer oil heating loop.
	Evaporator Temp Setpoint	Desired temperature for the evaporator oil loop.
	Feed Flow Rate	Methanol/water mixture flow rate into the reformer.
Gas Composition Control	Max CO (Min MeOH Mode)	Maximum allowed CO concentration when minimizing MeOH.
	Max MeOH (Min CO Mode)	Maximum allowed MeOH concentration when minimizing CO.
	Control Mode Toggle	Switch between: Off (0), Min MeOH (1), Min CO (2).
EMS Emulation	EMS On/Off State	Simulated system start/stop command (0 = Off, 1 = On).
	Power Reference	Requested fuel cell power output.
	Heat Demand	Simulated thermal load representing domestic heating.

5.1.1 Remote Operation Safety Measures

In order to ensure safe operation of the reformer test bench during automated and remote control, several protective measures were implemented. One such measure addresses the risk of communication failure. The reformer host system continuously monitors the synchronization of timestamps received from the remote GUI. If a desynchronization of 30 seconds or more is detected, the system automatically enters manual fallback mode to prevent unsafe behavior. In this mode, all critical control variables are reset to predefined safe values, as listed in Table 5.2.

These fallback values ensure that the system remains in a thermally and chemically non-hazardous state until user intervention is possible. Additionally, during normal operation, these same control variables are constrained by predefined maximum limits within the host program. This prevents the system from exceeding operational thresholds even if erroneous setpoints are issued remotely.

Table 5.2: Control setpoints enforced by the host program during communication loss and during normal operation.

Control Variable	Safe Value (De-Sync Mode)	Max Allowed Setpoint	Unit
Feed Flow Rate	0	80*	ml/min
Reformer Oil Loop Temperature	20	269**	°C
Evaporator Oil Loop Temperature	20	190	°C

* Limited by the heating power of the oil heater [3 kW].
** Max temperature the oil heater is capable of before entering alarm state.

The host program on the reformer test bench also receives transmitted data from the laboratory's gas alarm sensors to ensure safe operation. If any of these sensors report a value equal to or greater than 2, the system automatically sets the feed flow setpoint to 0 ml/min and triggers an audible alarm through the mid-level GUI program. The laboratory is equipped with 12 gas alarm sensors, all of which are monitored continuously by the host. These sensors are primarily configured to detect H_2 and methanol, both of which are relevant to the reformer's operation and present safety risks in the event of leaks. Their readings are also accessible via the GUI at any time, allowing users to stay informed about the safety status of the environment as well as get early indicators of leak issues.

5.2 Full System Test

To validate the integrated system under realistic operating conditions, a full-system test was conducted involving the reformer, fuel cell and thermal integration modules as well as the high-level EMS. The primary objective was to demonstrate coordinated operation across the HiL-based reformer module, digital fuel cell module, and EMS signal handling using the mid-level control layer.

Figure 5.2 shows the temperature evolution of both the reformer oil loop and the fuel cell module. The figure highlights the moment when the EMS issued the system "On" command and the point at which both modules reached their operational temperature thresholds, as determined by the mid-level controller. These markers confirm that the system can successfully transition from idle to active mode based on EMS input as well as initiate shutoff.

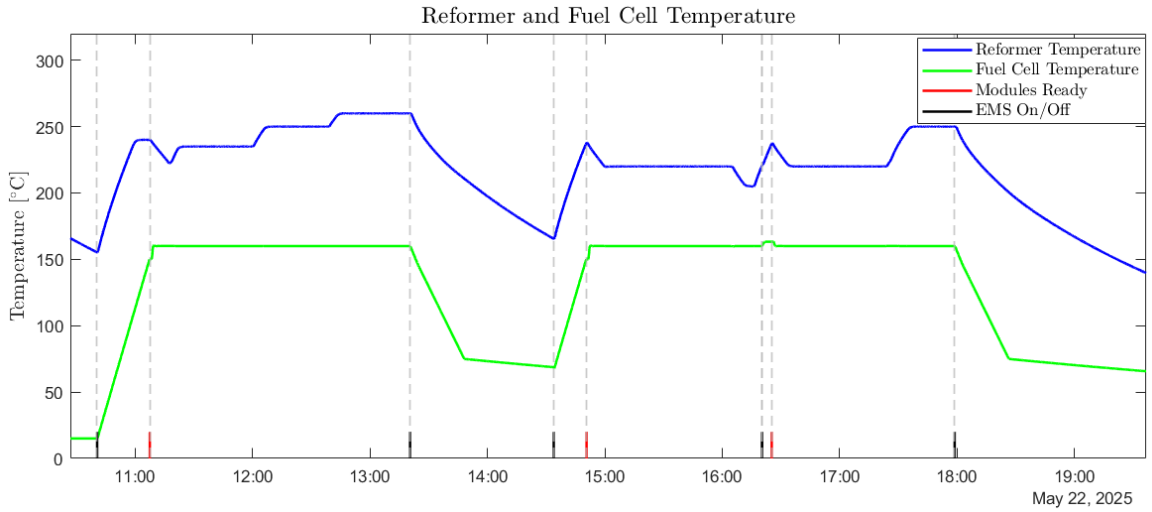

Figure 5.2: Temperature profiles of the reformer oil loop and fuel cell module during a full system test. The figure highlights the moment the On/Off signal is issued by the EMS layer, as well as the point at which the mid-level control layer determines that both modules have reached operational temperature and are ready to begin coordinated power and heat generation.

The system behavior observed around 16:20 resulted from a safety feature implemented in the mid-level control layer. This mechanism is designed to temporarily disengage the higher-level EMS layer if the average internal reformer temperature falls below a defined safety threshold, ensuring safe operation. In this particular test, the threshold was mistakenly set to an average of 180 °C over a 10-second window, despite the fact that the reformer is capable of operating safely at this temperature. As a result, the EMS was erroneously disengaged. The threshold has since been corrected to 160 °C to better reflect the reformer's actual operational capabilities.

Electrical Power Response

Figure 5.3 shows the electrical power reference set by the EMS layer and the actual power, current and stack voltage output from the fuel cell module. The response closely tracks the reference, demonstrating effective coordination between the modules and confirming that the fuel cell module adapts dynamically to EMS commands.

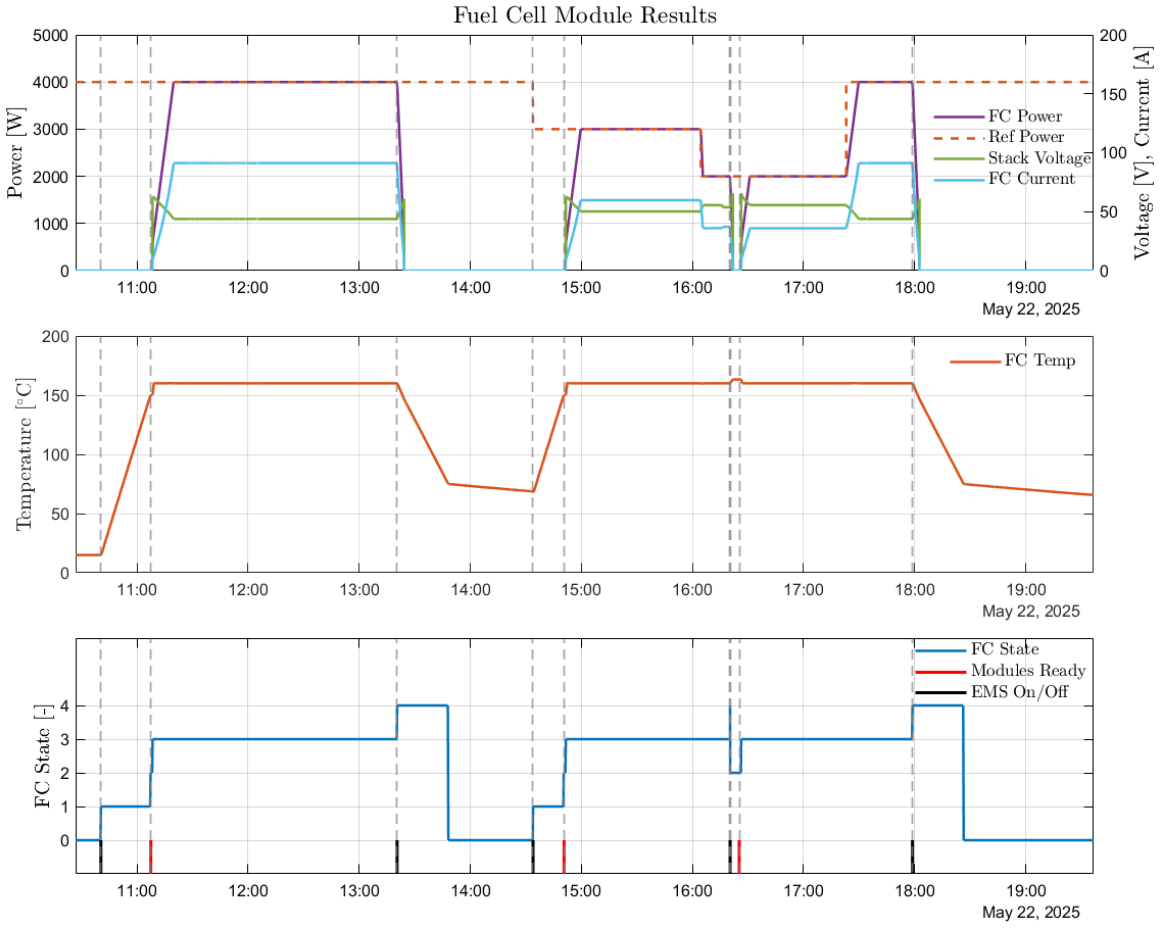

Figure 5.3: Comparison of the power reference from the EMS and the simulated power output from the fuel cell model.

At 10:40 the fuel cell module receives an "On" signal from EMS and the temperature of the fuel cell begins to increase from the initial temperature of 15 °C to the fuel cell standby temperature of 150 °C. Since the reformer started warmup already at a temperature of 150 °C, the reformer is ready before the fuel cell module. The *Standby* state of the fuel cell module is therefore skipped, and as soon as the fuel cell module reaches 150 °C, the system goes into operation. The power begins to ramp up until it reaches the power setpoint for the first cycle at 4 kW. The temperature controller of the fuel cell stack manages to keep the temperature of the fuel cell module steady at the setpoint temperature of 160 °C. Once the EMS "Off" signal is received the fuel cell module goes into *Active Cooldown*, until it reaches 75 °C, at which point it goes into the *Off* state. During the second cycle the power is varied, starting at a reference power of 3 kW, then being reduced to 2 kW, before being increased to 4 kW. The fuel cell module is able to accurately meet the power demand. At 16:20 the safety feature on the reformer briefly shut the system down, putting the fuel cell module into *Standby*. Once the issue was fixed operation continued.

To take into account the hot water demand throughout the test, a dataset of residential heat demand, recorded as part of the FC-COGEN project, is used [EUDP, 2025]. The simulated temperature development of the HWT, the heat generated by the fuel cell and the reference heat demand is shown in Figure 5.4.

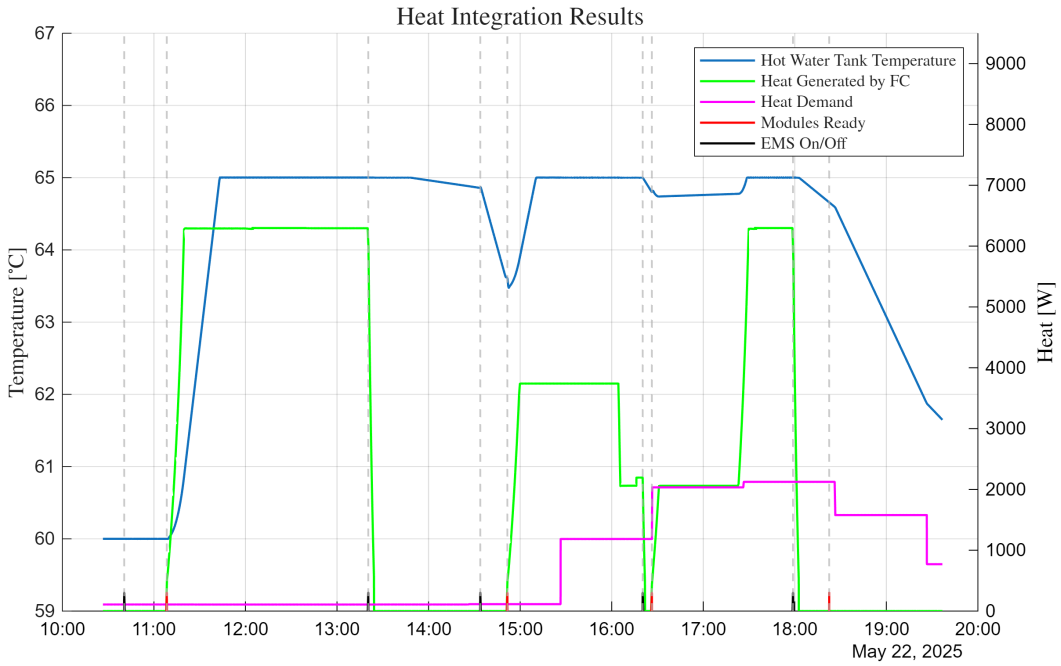

Figure 5.4: Temperature development of the HWT, heat generated by the fuel cell and domestic heat demand, throughout the validation test.

The HWT starts at a temperature of 60 °C. Once the system is turned on the temperature quickly rises to the maximum temperature of 65 °C, due to the low heat demand. The heat generated by the fuel cell in this period is lost to the surroundings, and therefore constitute an efficiency loss for the system's total efficiency. Only when the system is turned off is the heat demand large enough to decrease the temperature of the HWT. Once the system is turned on for the second cycle, the temperature once again rises to the maximum temperature. This indicates that the heat demand can generally be covered by the excess heat from the fuel cell during operation, and only when not in operation is additional potentially heat required from an external source.

The electrical efficiency across the system validation test is 29%, with respect to the LHV and with an anode stoichiometry of λ_a = 1.25, while the total efficiency is 69%. This total efficiency is overestimated compared to a real system since the model assumes all the generated heat is removed through the cooling loop, and that none is removed through passive cooling and the cathode flow. Thus the only heat lost, is the heat transferred through a radiator in the cases where the HWT is at its upper threshold temperature.

Reformate Gas Response

Figure 5.5 shows the reformate gas composition response during the full-system validation test. The measured mole fractions of H_2, CO, CO_2, and methanol slip are plotted over time, capturing the impact of dynamic operational conditions such as start-up, power ramping, composition control adjustments and shutdown sequence.

The hydrogen concentration remains relatively stable during steady operation, indicating

that the gas composition control has limited impact on the amount of H_2 being produced. The CO and methanol concentrations exhibit expected fluctuations during steady power production. The test was conducted in minimizing CO mode and during the first operation period from 11:00 to 13:30 the max allowed methanol value was lowered from 1 Vol% to 0.5 Vol% at 12:00 and 0.35 Vol% at 12:50.

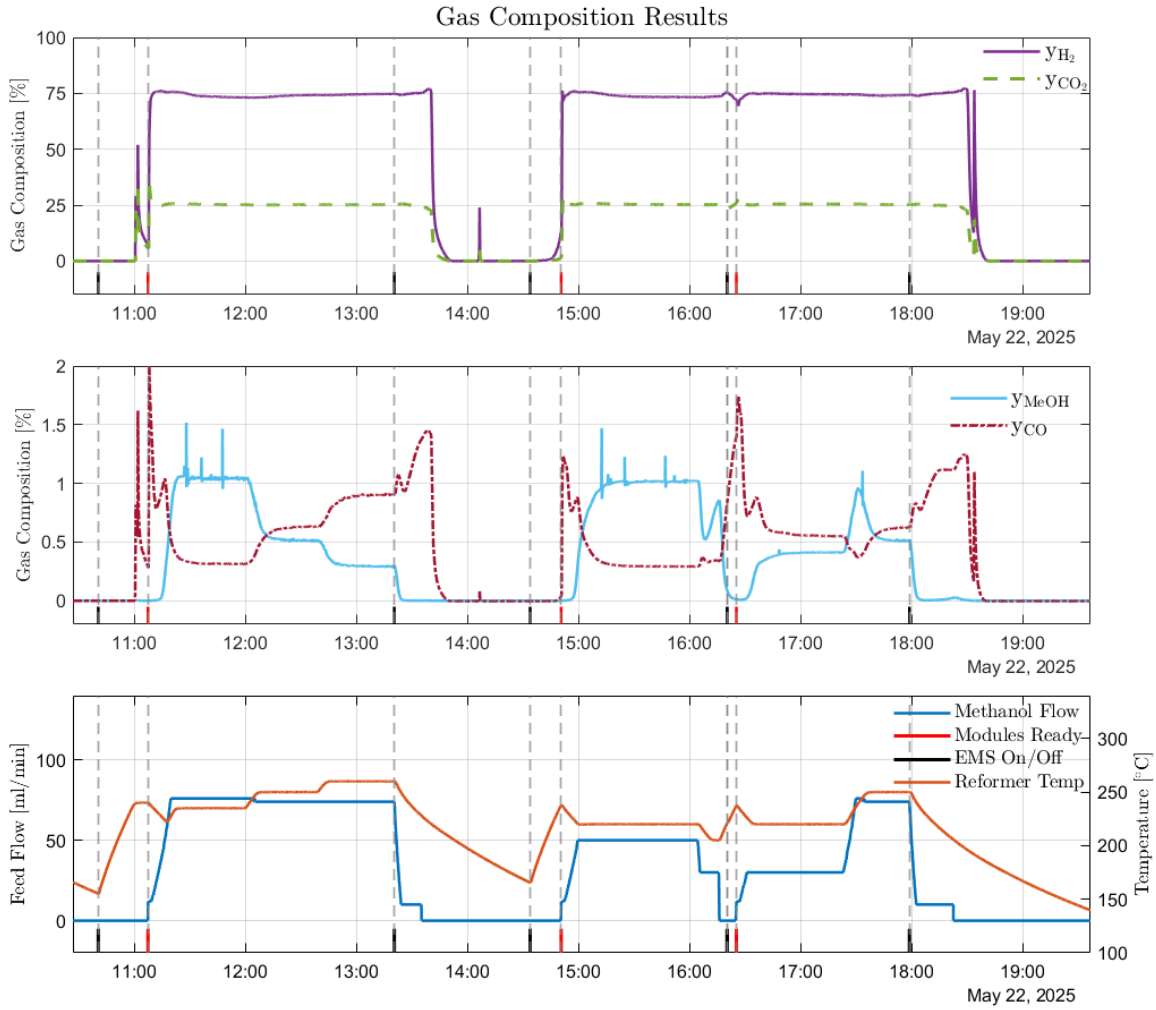

Figure 5.5: Measured reformate gas composition during full-system validation. The plot shows dynamic responses of H_2, CO, CO_2, and methanol as the system transitions through various operational states.

Figure 5.6 illustrates the performance of the gas composition shaping system during part of the full-system validation test scenario, specifically from 10:00 to 14:10. The plot displays the concentrations of CO and methanol in the reformate gas, alongside the changes in max allowed methanol as well as the estimated minimized CO.

Through the interface the max allowed methanol is changed and the plot shows the reformer module changing the oil loop temperature to minimize the CO while keeping the methanol at this max value.

The results show that the composition control system works well in a full system test, with the methanol stabilizing at 1.04 Vol% at a max allowed of 1 Vol%, 0.52 at a max allowed of

0.5 and 0.3 at a max allowed of 0.35.

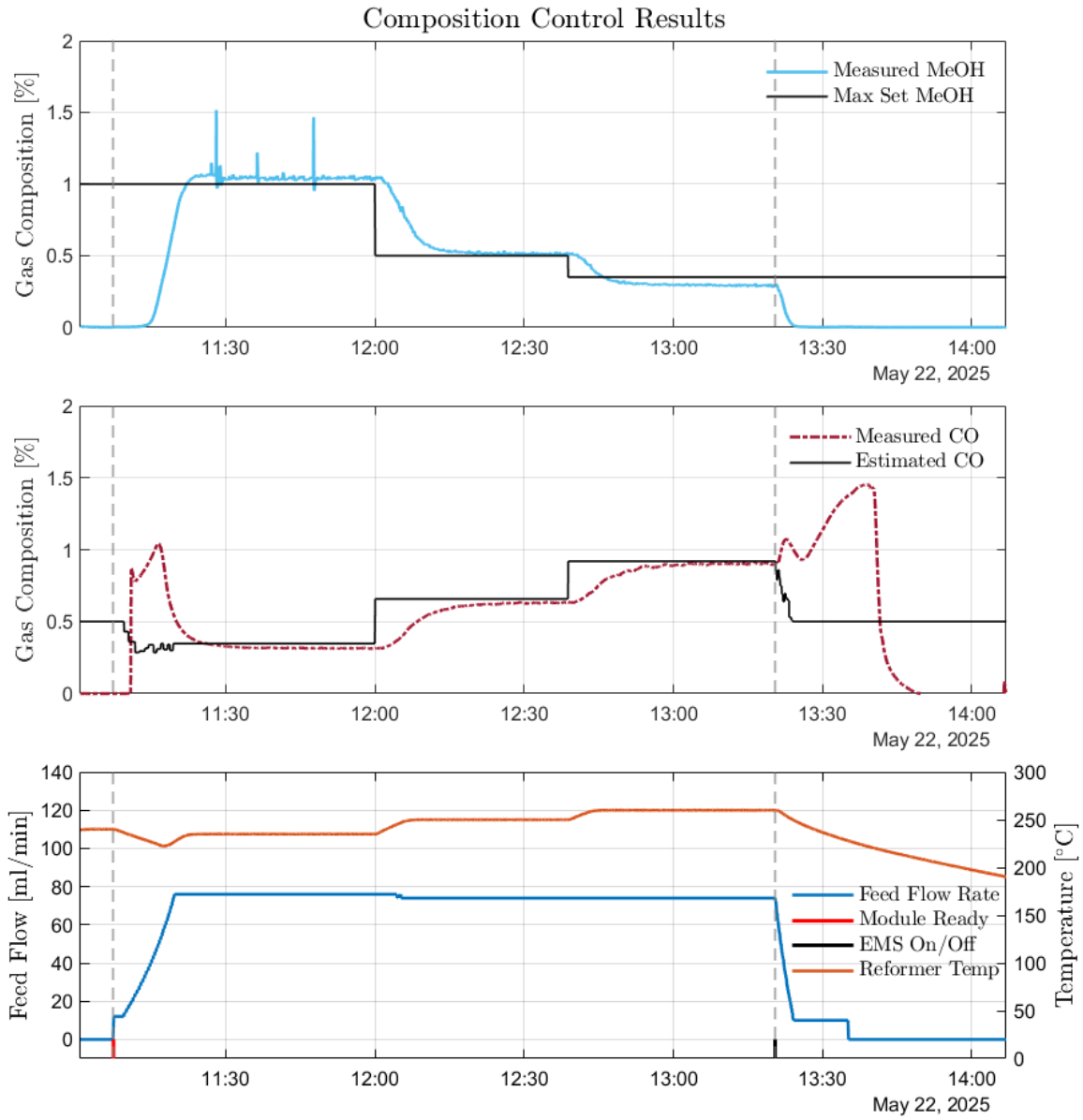

Figure 5.6: Measured CO and methanol compositions during part of the full system test. The plot shows the response of CO and methanol as the system transitions through various operational states and at different composition control parameter setpoints

Table 5.3 presents the outcome of three test scenarios designed to validate the composition shaping system under full system operation. In each case, the control objective was to minimize the concentration of CO in the reformate gas while ensuring that the methanol slip remained below a specified upper limit—set at 1.00, 0.50, and 0.35 Vol% respectively.

The results show that the system was able to maintain methanol slip close to the specified thresholds in all cases, with stabilized values of 1.04, 0.52, and 0.285 Vol%. Correspondingly, the CO concentration was minimized within these constraints, achieving stabilized

values of 0.315, 0.631, and 0.904 Vol%. The table also includes the estimated CO levels computed during operation, which closely match the measured concentrations, thereby demonstrating both the reliability of the estimation method and the effectiveness of the real-time control strategy.

These results confirm that the composition shaping system can successfully navigate the trade-off between minimizing CO and limiting methanol slip through dynamic adjustment of the reformer operating temperature.

Table 5.3: Results of gas composition shaping during full-system test. Columns represent each composition control case.

Metric	**Case 1**	**Case 2**	**Case 3**
Max MeOH [Vol%]	1	0.5	0.35
Stabilized MeOH [Vol%]	1.04	0.52	0.285
Estimated CO [Vol%])	0.3475	0.6575	0.92
Stabilized CO [Vol%]	0.315	0.6314	0.904

Chapter 6

Discussion

6.1 Module Communication

All variables transmitted between the different layers and modules are updated at a fixed interval of one second (1 Hz). Given the current scale and dynamic behavior of the system, this update rate has proven sufficient to maintain effective coordination between the reformer, fuel cell, and thermal integration modules. However, in applications involving faster dynamics or more stringent control requirements, future implementations may benefit from adjustable or higher-frequency update rates. Notably, the current system architecture imposes no inherent limitations that would prevent such a change.

6.2 Experimental

Equipment constraints in the reformer test bench limited the scope of the experimental tests. The feed flow rate of the methanol/water mixture was capped at approximately 80 ml/min due to the power limitations of the oil heater used to heat the evaporator. Additionally, the maximum reformer oil loop temperature was restricted to below 270 °C, as the oil bath heater would trigger an alarm if the oil bath temperature reached exactly 270°C or above.

Several of the instruments used in the gas analysis unit of the reformer test bench are sensitive to moisture and therefore require dry gas samples for accurate measurement. As a result, only the FIDAMAT 6, which measures methanol slip, operates on the wet gas stream and provides measurements of the uncondensed gas composition. All other analyzers, such as those used for CO and CO_2 require the gas to pass through a condenser unit to remove water before analysis. This setup necessitates estimating the wet gas composition from the dry measurements provided by most of the analyzers. While this estimation generally carries a low level of uncertainty, the key source of error arises from how the carbon balance is calculated. Specifically, the methanol concentration measured in wet composition by the FIDAMAT 6, is incorrectly treated as dry in the carbon balance calculation. This assumption results in an underestimation of the total carbon molar flow exiting the reformer. As a consequence, a small but systematic error is introduced in the conversion from dry to wet composition.

The characterization of the reformate gas composition as a function of feed flow rate and reformer temperature was conducted using relatively large step changes in both parameters. This approach resulted in a coarse granularity of the measured data. To mitigate this limitation and enhance the resolution of the resulting characterization maps, the data matrices were interpolated, effectively doubling the point density and enabling smoother transitions in subsequent estimations. It is presumed that applying an even finer interpolation could further enhance the performance of the gas composition adjustment strategy,

particularly in operating regions with high sensitivity to temperature or flow variations.

6.3 Model limitations

The fuel cell module created in this thesis has proven reasonably accurate both in steady state and dynamic operation. However, a number of points could be improved upon to make the module more accurate for simulating both steady state and dynamic operation. The model underestimates the impact of the pressure of the anode and cathode, over-predicting the cell voltage at low pressure and under-predicting the cell voltage at higher pressures.

The model could also be improved by taking into account the specific impacts that each component of the reformed gas has on the voltage losses, since these can be different for each component in addition to lowering the molar flow rate of hydrogen.

Only the temperature dynamics of the fuel cell are explicitly modeled. While these are the slowest and most dominant dynamics, especially under the imposed power ramp-rate limitation of 5 W/s, other important dynamics such as gas flow distribution and electrochemical transients are neglected. These effects could be impactful in scenarios where the constraints such as the power ramp-rate is the area of investigation, or the operation is under fault conditions.

The fuel cell module assumes idealized thermal control, meaning that it is presumed that the heat exchanger can always cool the oil loop such that it can achieve the setpoint temperature with sufficient responsiveness. In practice, the heat exchangers and thermal integration modules dynamics would limit how fast the oil temperature can be adjusted, and would also necessitate more complex system design and control implementation.

The anode stoichiometry of the fuel cell is fixed at $\lambda_a = 1.25$. This stochiometry is assumed to be high enough to operate a fuel cell safely without risk of starvation. The HiL reformer module uses an electric oil heater to heat the reformer, since the reformation reactions are predominantly endothermic. However, the FC-COGEN project utilizes a burner instead of the electric heater to accomplish this. The burner is fueled by the anode waste gas exiting the fuel cell which necessitates a significantly higher stoichiometry than used in this thesis. Moreover, since the energy input from the electric oil heaters used in this HiL setup is not included in the system energy balance, a meaningful calculation of overall system efficiency is not feasible. Neglecting this substantial thermal input would lead to artificially inflated efficiency figures. The balance of plant is also not taken into account, however the contribution of the balance of plant is often small compared to other efficiency losses seen in MSR HT-PEMFC systems.

Chapter 7

Conclusion

This work investigated the integration of digital models and physical hardware in a modular reformed methanol fuel cell system, with the aim of advancing real-time testing strategies for micro-CHP applications.

The distributed architecture developed in this work enables each major subsystem, including the reformer, fuel cell, and residential heat integration, to operate semi-independently while maintaining real-time coordination through a mid-level control layer. This modularity facilitates the real-time integration of both hardware-based and model-based approaches. Hardware-in-the-loop techniques are employed in subsystems like the reformer module, where complex dynamics are difficult to model accurately, thereby improving the reliability of the results from here. Conversely, in components where the dynamics are better understood and sufficiently captured by models, such as the fuel cell and thermal integration, model-based techniques reduce system complexity.

A gray-box fuel cell model was developed as part of the distributed test architecture. Data from a fuel cell load cycling test, which is part of a larger test base, was used to fit key parameters of the model to develop a polarization curve as a function of the current density, temperature of the fuel cell stack, anode and cathode pressures. The model reached an average relative error of 3.45% and an average absolute error of 61 W across the reference dataset it was fitted to, while it reached an average relative error of 8.45% and an average absolute error of 75 W across a separate validation dataset. The heat output of the fuel cell is calculated based on the electric efficiency of the fuel cell, and together with a heat transfer model for the oil loop the thermal dynamics of the fuel cell was modeled. This model of the temperature dynamics of the fuel cell showed good agreement with the temperature dynamic of the reference load cycling test.

The fuel cell module is incorporated into the distributed test architecture and receives a control signal from the mid-level control layer signaling when the EMS layer requires the system to produce power. This signal is used in the fuel cell module to initiate an internal startup and shutdown procedures. These procedures were designed based on data from a start/stop test performed by Blue World Technologies on a prototype methanol steam reformed high temperature PEM fuel cell system. The fuel cell model was able to mimic the temperature dynamics during startup and shutdown well, if a bit simplified. The model also showed good agreement with the reference current and voltage dynamics during operation.

A central contribution of this project is the implementation and integration of a reformer test bench as a HiL module. To support this integration, a dedicated gas composition characterization experiment was conducted on the reformer to understand how feed flow rate and reformer oil temperature influence the resulting gas mixture. These results were

used to construct lookup tables for estimating wet gas composition in real time. By incorporating real dynamic responses from the reformer into the simulation environment, the system can more accurately capture the nonlinear behavior of methanol steam reforming under varying thermal and flow conditions. This is particularly important for modeling gas composition outputs and transient thermal behavior, which are difficult to represent using purely theoretical models. The test bench not only supports validation of reformer control strategies but also provides a flexible platform for investigating gas composition shaping and long-term degradation effects.

To further enhance reformate gas quality, a reformer oil loop temperature-based composition adjustment strategy was implemented using the result matrices from the characterization experiment. The strategy enabled dynamic adjustment of the reformer oil temperature to shape the concentrations of impurities, specifically CO and methanol slip, based on predefined constraints. The system allowed the user to toggle between two control modes: minimizing CO while keeping methanol below a defined threshold, or minimizing methanol while constraining CO levels. Validation tests were conducted under three different feed flow rates (20, 40, and 60 ml/min) and demonstrated that the control logic could successfully steer the composition toward the target values. In the CO minimization mode, the estimated and measured concentrations showed strong agreement, with relative errors for both CO and methanol below 5%. In contrast, the methanol minimization mode showed more variable performance, particularly at lower flow rates, where the relative deviation reached 142%. However, at medium to high flow rates, the estimates were significantly more accurate, with relative deviations falling below 10%. Notably, the absolute differences between measured and estimated values across all cases remained around 600 ppm or lower.

These results show that the reformer temperature-based gas composition adjustment approach has effective capabilities to shape the reformate gas composition under varying feed flow rate operation. The capability to shape reformate gas composition based on operational objectives adds functional flexibility to the reformer module and could be useful in scenarios requiring fine-tuned fuel cell input conditions or accelerated degradation studies.

A system validation test was performed across a 9-hour period by doing a 2 cycle start/stop test of the system with varying power loads. The test proved that the distributed test architecture was capable of communicating the required signals to the modules. The mid-level control system was able to control the power output of the fuel cell module, and initiate the startup and shutdown procedures. The composition control was shown to accurately control the composition, throughout the test. Despite not being the intent, the validation test also tested the safety protocols included in this project, shutting the system down when the temperature of the reformer crossed the minimum temperature.

This thesis demonstrated the design and integration of a modular high-temperature PEM fuel cell system for combined heat and power applications, with a focus on real-time distributed testing architecture and hardware-in-the-loop implementation. A central goal of the project was to combine simulation and physical systems by creating a test environment, where digital models and hardware components interact dynamically. Through this

approach, key challenges related to system coordination, start-up logic and gas composition control were explored under realistic operating conditions.

Chapter 8

Future Work

The work done in this thesis presents opportunities for further research in the topic of distributed test architectures. This chapter explores these opportunities for expanding on the work done in this thesis.

8.1 Hardware-in-the-Loop Emulators

This thesis has demonstrated that a distributed test architecture can effectively link simulation environments with physical HiL test benches. However, the same architecture also enables the implementation of HiL emulators, physical subsystems that use computational models to replicate the behavior of components under test. Unlike pure simulations, these emulators interact with real hardware in real time, offering a hybrid between model-based control and physical testing.

HiL emulators offer similar benefits to HiL test benches in that they can capture system-level dynamics more realistically than abstract simulations. However, they do so without the need for full physical prototypes, resulting in significantly lower capital and operational costs. This makes them especially useful for early stage testing, sensitivity analysis, or scenarios where safety, cost, or availability limits the use of actual hardware.

The modular structure of the distributed test architecture developed in this project supports the flexible implementation of such emulators. For example, future work could include a thermal HiL emulator designed to evaluate heat integration strategies. By using the existing fuel cell module to simulate thermal output, a physical system could emulate the heat transfer, oil loop thermal inertia, and heat exchange behavior with water tanks or radiators. This would allow for focused investigation of thermal management strategies in a micro-CHP context, without requiring a fully operational fuel cell system.

8.2 Further Research on Dynamic Interactions Between Fuel Cells and Reformers

While the tests performed on the interaction between the fuel cell module and the reformer was limited, it has proven the potential of the distributed test architecture to act as a research tool. This tool could potentially allow for faster research done on how fuel cells and reformers interact dynamically. This is useful for research projects that include reformed high-temperature PEM fuel cells with dynamic loads, such as FC-COGEN.

Control over more parameters from the mid-level control layer on the fuel cell module, such as fuel cell temperature setpoint, anode stoichiometry, ramp rate of the power, etc.,

would allow for a wider range of test to be performed on the interconnectivity of the system.

8.3 Remote Test Bench Interface

The use of a distributed test architecture that operates over the internet opens new opportunities for remote access to physical test benches. By enabling bidirectional communication between simulation environments and hardware modules via lightweight protocols, test setups can be controlled, monitored, and modified from geographically distant locations.

This capability introduces significant potential for collaborative research and cost-effective infrastructure sharing. Universities, research institutions, and industrial partners can connect to and interact with remote laboratory setups without requiring local hardware. As a result, the need for duplicating expensive experimental infrastructure across multiple sites is reduced, facilitating more efficient use of resources.

Furthermore, this approach allows institutions to share test bench time or offer remote access to experimental platforms for teaching, prototyping, or system validation. In the context of micro-CHP or fuel cell system research, where test equipment can be costly and specialized, such remote interfacing enhances accessibility and scalability.

8.4 Degradation Analysis

The successful implementation of gas composition control in the reformer module significantly enhances its experimental flexibility. By enabling real-time adjustment of CO and methanol concentrations in the reformate gas, the test bench can serve as a controllable reformate gas generator. This functionality allows for the generation of gas mixtures with well defined and reproducible compositions, closely replicating real-world conditions. One particularly promising application is the study of catalyst poisoning in HT-PEM fuel cells due to CO and methanol slip, which are factors known to adversely affect both efficiency and long-term durability.

Another future development area is the refinement of the built-in health monitoring functionality. The LabVIEW program on the host computer currently tracks discrepancies between measured gas compositions and estimated values based on prior characterization. These deviations can act as early indicators of performance drift or catalyst degradation. Future work could extend this functionality into a fully-fledged degradation monitoring framework, incorporating data logging, trend analysis, and possibly machine learning algorithms to model reformer aging in real time.

8.5 Digital Reformer Twin

With the reformer test bench always transmitting a plethora of measurements to an intermediary server a future addition to the system could involve development of a digital

twin of the reformer test bench. A digital twin is a real-time, computer generated representation of a physical system that continuously receive real-time data from its physical counterpart and uses this data to update its internal adaptive models so as to better emulate the behavior of the physical system.

In the context of this project, the digital twin could leverage the developed distributed test architecture to synchronize the physical reformer test bench with a real-time simulation model deployed elsewhere. By integrating sensor data such as internal temperatures, feed flow rates, gas composition, and control inputs, the twin could serve multiple roles such as:

- Fault detection and diagnostics, by comparing expected behavior from the model with live measurements.
- Predictive maintenance, by tracking trends that may indicate catalyst degradation or sensor drift.
- Model refinement, as live data can be used to recalibrate or retrain empirical or black-box models like neural networks or *Adaptive Neuro-Fuzzy Inference System* (ANFIS) models.
- Scenario testing and control development, where control strategies can be virtually tested before being deployed on the real hardware.

Bibliography

[Araya, 2012] Araya, S. (2012). High temperature pem fuel cells - degradation and durability.

[Arsalis et al., 2011] Arsalis, A., Nielsen, M. P., and Kær, S. K. (2011). Modeling and off-design performance of a 1kw ht-pemfc (high temperature-proton exchange membrane fuel cell)-based residential micro-chp (combined-heat-and-power) system for danish single-family households. *Energy (Oxford)*, 36(2):993–1002.

[Behrens and Armbrüster, 2012] Behrens, M. and Armbrüster, M. (2012). *Methanol Steam Reforming*, pages 175–235. Springer New York, New York, NY.

[Cengel et al., 2017] Cengel, Y. A., Cimbala, J. M., and Turner, R. H. (2017). *Fundamentals of Thermal Fluid Sciences*. McGraw-Hill Education / Asia, S.l, 5.ed. edition.

[Cengel and Ghajar, 2020] Cengel, Y. A. and Ghajar, A. J. (2020 - 2020). *Heat and mass transfer : fundamentals applications*. McGraw-Hill Education, New York, sixth edition in si units. edition.

[Ebi et al., 2016] Ebi, K. L., Ziska, L. H., and Yohe, G. W. (2016). The shape of impacts to come: lessons and opportunities for adaptation from uneven increases in global and regional temperatures. *Climatic change*, 139(3-4):341–349.

[ECHA, 2025] ECHA (2025). Echa chemical database. https://chem.echa.europa.eu/. Accessed: 2025-05-26.

[El-Baz et al., 2015] El-Baz, W., Sänger, F., and Tzscheutschler, P. (2015). Hardware in the loop (hil) for micro chp systems. In *Proceedings of the Fourth International Conference on Microgeneration and related Technologies, Tokyo, Japan*, pages 28–30.

[EUDP, 2025] EUDP (2025). Fc-cogen project. https://eudp.dk/en/node/16733. Accessed: 2025-05-04.

[Fröjd et al., 2014] Fröjd, K., Axelsson, K., Torstensson, I., Åberg, E., Osvaldsson, E., Dolanc, G., Pregelj, B., Eborn, J., and Pålsson, J. (2014). Development of a real-time fuel processor model for hil simulation. In *Modelica 2014 Conference*, pages 675–682.

[García-Valverde et al., 2012] García-Valverde, R., Espinosa, N., and Urbina, A. (2012). Simple pem water electrolyser model and experimental validation. *International Journal of Hydrogen Energy*, 37(2):1927–1938. 10th International Conference on Clean Energy 2010.

[Herdem et al., 2018] Herdem, M. S., Mundhwa, M., Farhad, S., and Hamdullahpur, F. (2018). Multiphysics modeling and heat distribution study in a catalytic microchannel methanol steam reformer. *Energy&fuels*, 32(6):7220–7234.

[Holladay et al., 2009] Holladay, J., Hu, J., King, D., and Wang, Y. (2009). An overview of hydrogen production technologies. *Catalysis Today*, 139(4):244–260. Hydrogen Production - Selected papers from the Hydrogen Production Symposium at the American Chemical Society 234th National Meeting & Exposition, August 19-23, 2007, Boston, MA, USA.

[IPCC, 2022] IPCC (2022). *Impacts of 1.5°C Global Warming on Natural and Human Systems*, page 175–312. Cambridge University Press.

[Justesen, 2015] Justesen, K. K. (2015). Reformed methanol fuel cell systems - and their use in electric hybrid systems.

[Justesen et al., 2013] Justesen, K. K., Andreasen, S. J., Shaker, H. R., Ehmsen, M. P., and Andersen, J. (2013). Gas composition modeling in a reformed methanol fuel cell system using adaptive neuro-fuzzy inference systems. *International Journal of Hydrogen Energy*, 38(25):10577–10584.

[Khayet and Zárate, 2005] Khayet, M. and Zárate, J. M. O. d. (2005). Application of the multi-current transient hot-wire technique for absolute measurements of the thermal conductivity of glycols. *International journal of thermophysics*, 26(3):637–646.

[Khotseng, 2019] Khotseng, L. (2019). Fuel cell thermodynamics. In Vizureanu, P., editor, *Thermodynamics and Energy Engineering*, chapter 1. IntechOpen, Rijeka.

[Kurpit, 1975] Kurpit, S. S. (1975). 1.5 and 3KW indirect methanol-air fuel cell power plants. In *Energy 10; Annual Intersociety Energy Conversion and Engineering Conference*, pages 222–228.

[Larminie and Dicks, 2003] Larminie, J. and Dicks, A. (2003). *Fuel cell systems explained.* J. Wiley, Chichester, West Sussex, 2nd ed. edition.

[Li et al., 2009] Li, C.-K., Soriano, A. N., and Li, M.-H. (2009). Heat capacities of the mixed-solvents desiccants (glycols + water + salts). *Thermochimica acta*, 487(1):26–32.

[Li et al., 2023] Li, N., Cui, X., Zhu, J., Zhou, M., Liso, V., Cinti, G., Sahlin, S., and Simon Araya, S. (2023). A review of reformed methanol-high temperature proton exchange membrane fuel cell systems. *Renewable and Sustainable Energy Reviews*, 182.

[Marnay et al., 2015] Marnay, C., Chatzivasileiadis, S., Joos, G., Abbey, C., Lombardi, P., Iravani, R., Mancarella, P., and von Appen, J. (2015). Microgrid evolution roadmap. In *2015 International Symposium on Smart Electric Distribution Systems and Technologies (EDST)*, pages 139–144. IEEE.

[Niaz et al., 2015] Niaz, S., Manzoor, T., and Pandith, A. H. (2015). Hydrogen storage: Materials, methods and perspectives. *Renewable & sustainable energy reviews*, 50:457–469.

[NIST, 2025] NIST (2025). Thermophysical properties of fluid systems. https://webbook.nist.gov/chemistry/fluid/. Accessed: 2025-05-05.

[O'Hayre, 2016] O'Hayre, R. (2016). *Fuel cell fundamentals.* Wiley, Chichester, elektronisk udgave; 3. ed. edition.

[Peppley et al., 1999] Peppley, B. A., Amphlett, J. C., Kearns, L. M., and Mann, R. F. (1999). Methanol–steam reforming on cu/zno/al2o3. part 1: the reaction network. *Applied catalysis. A, General*, 179(1-2):21–29.

[Rechberger et al., 2009] Rechberger, J., Schauperl, R., Hansen, J. B., and Larsen, P. K. (2009). Development of a methanol sofc apu demonstration system. *ECS Transactions*, 25(2):1085.

[Rosli et al., 2017] Rosli, R., Sulong, A., Daud, W., Zulkifley, M., Husaini, T., Rosli, M., Majlan, E., and Haque, M. (2017). A review of high-temperature proton exchange membrane fuel cell (ht-pemfc) system. *International Journal of Hydrogen Energy*, 42(14):9293–9314. Special Issue on Sustainable Fuel Cell and Hydrogen Technologies: The 5th International Conference on Fuel Cell and Hydrogen Technology (ICFCHT 2015), 1-3 September 2015, Kuala Lumpur, Malaysia.

[Sagdeev et al., 2012] Sagdeev, D., Fomina, M., Mukhamedzyanov, G., and Abdulagatov, I. (2012). Experimental study of the density and viscosity of polyethylene glycols and their mixtures at temperatures from 293 k to 465 k and at high pressures up to 245 mpa. *Fluid phase equilibria*, 315:64–76.

[Sahlin, 2016] Sahlin, S. (2016). Characterization and modeling of a methanol reforming fuel cell system: Karakterisering og modellering af en methanol reformering fuel cell system. Søren Juhl Andreasen, Principal supervisor.

[Sebbahi et al., 2022] Sebbahi, S., Nabil, N., Alaoui-Belghiti, A., Laasri, S., Rachidi, S., and Hajjaji, A. (2022). Assessment of the three most developed water electrolysis technologies: Alkaline water electrolysis, proton exchange membrane and solid-oxide electrolysis. *Materials Today: Proceedings*, 66:140–145. 4th International Conference on Advanced Materials for Photonics, Sensing and Energy Conversion Energy Applications.

[Siemens AG, nda] Siemens AG (n.d.a). CALOMAT 6 – Thermal Conductivity Gas Analyzer. `https://mall.industry.siemens.com/mall/en/WW/Catalog/Products/10028635`. Accessed: 2025-04-29.

[Siemens AG, ndb] Siemens AG (n.d.b). ULTRAMAT 6 – Infrared Gas Analyzer. `https://mall.industry.siemens.com/mall/da/dk/Catalog/Products/10028608`. Accessed: 2025-04-29.

[Sá et al., 2011] Sá, S., Sousa, J. M., and Mendes, A. (2011). Steam reforming of methanol over a cuo/zno/al2o3 catalyst, part i: Kinetic modelling. *Chemical Engineering Science*, 66(20):4913–4921.

[Tripathi and Gonzalez-Longatt, 2023] Tripathi, S. M. and Gonzalez-Longatt, F. M. (2023). *Real-Time Simulation and Hardware-in-the-Loop Testing Using Typhoon HIL*. Transactions on Computer Systems and Networks. Springer Nature Singapore, Singapore, 1st ed. 2023. edition.

[Valera-Medina et al., 2018] Valera-Medina, A., Xiao, H., Owen-Jones, M., David, W., and Bowen, P. (2018). Ammonia for power. *Progress in energy and combustion science*, 69:63–102.

[Xie et al., 2025] Xie, P., Zhou, F., Tan, S., Liso, V., and Sahlin, S. L. (2025). Development of a two-layer control and management system for a residential microgrid with ht-pemfc-based micro-chp. *Applied Energy*, 381:125118.

[Xu et al., 2023] Xu, J., Zhao, Y., Wu, Y., Wang, Y., Xiao, S., and Xu, X. (2023). Experimental investigation on influences of methanol reformate impurities in performances of high temperature proton exchange membrane fuel cells. *International Journal of Hydrogen Energy*, 48(45):17261–17276.

[Yan et al., 2006] Yan, Q., Toghiani, H., and Causey, H. (2006). Steady state and dynamic performance of proton exchange membrane fuel cells (pemfcs) under various operating conditions and load changes. *Journal of Power Sources*, 161(1):492–502.

[Yoon et al., 2007] Yoon, H. C., Otero, J., and Erickson, P. A. (2007). Reactor design limitations for the steam reforming of methanol. *Applied Catalysis B: Environmental*, 75(3):264–271.

[Zamfirescu and Dincer, 2009] Zamfirescu, C. and Dincer, I. (2009). Ammonia as a green fuel and hydrogen source for vehicular applications. *Fuel processing technology*, 90(5):729–737.

[Zhang et al., 2006] Zhang, J., Tang, Y., Song, C., Zhang, J., and Wang, H. (2006). Pem fuel cell open circuit voltage (ocv) in the temperature range of 23°c to 120°c. *Journal of Power Sources*, 163(1):532–537. Special issue including selected papers presented at the Second International Conference on Polymer Batteries and Fuel Cells together with regular papers.

[Zhao et al., 2022] Zhao, J., Chang, H., Luo, X., Tu, Z., and Chan, S. H. (2022). Dynamic analysis of a cchp system based on fuel cells integrated with methanol-reforming and dehumidification for data centers. *Applied Energy*, 309:118496.

Appendix A

Reformer Characterization Test Standard Deviations

This appendix presents the standard deviations associated with the gas composition measurements obtained during the reformer characterization experiments described in Chapter 4. The purpose of these experiments was to map the steady-state reformate gas composition—specifically the concentrations of H_2, CO_2, methanol, and CO as a function of feed flow rate and reformer oil temperature.

To ensure the accuracy of the characterization data, each operating point was held for a duration of 200 seconds after reaching steady state. During this period, gas composition measurements were logged at a frequency of 1 Hz. The standard deviation of each gas component was then calculated over this interval to quantify how much the data spread out around the mean.

Table A.1: Standard deviation of H_2 concentration measurements during the reformer characterization experiment. Values are reported for each combination of feed flow rate and reformer oil temperature.

Flow [ml/min]	200°C	210°C	220°C	230°C	240°C	250°C	260°C
10	2.61e-04	2.84e-04	2.39e-04	2.37e-04	2.15e-04	1.96e-04	1.44e-04
20	2.72e-04	4.49e-04	1.44e-04	1.58e-04	1.39e-04	7.32e-04	1.01e-04
30	0.0043	5.3e-04	3.1e-04	2.38e-04	3.11e-04	1.29e-04	1.16e-04
40	0.0037	0.0018	7.44e-04	0.0012	8.89e-04	1.68e-04	1.56e-04
50	0.0030	0.0016	0.0012	0.0011	0.0011	2.16e-04	2.55e-04
60	0.0018	8.35e-04	8.89e-04	8.33e-04	8.96e-04	3.73e-04	3.69e-04
70	0.0017	6.39e-04	6.27e-04	0.0037	6.16e-04	5.85e-04	4.18e-04
80	8.25e-04	2.45e-04	4.15e-04	0.0016	5.13e-04	4.8e-04	3.9e-04

Table A.2: Standard deviation of CO_2 concentration measurements during the reformer characterization experiment. Values are reported for each combination of feed flow rate and reformer oil temperature.

Flow [ml/min]	200°C	210°C	220°C	230°C	240°C	250°C	260°C
10	2.84e-04	9.377e-05	2.11e-04	2.43e-04	2.33e-04	1.97e-04	2.09e-04
20	1.28e-04	2.42e-04	1.144e-04	1.55e-04	8.95e-04	8.18e-04	7.66e-04
30	0.0035	2.14e-04	2.50e-04	1.38e-04	2.16e-04	8.86e-04	6.25e-04
40	0.003	0.0014	1.68e-04	8.69e-04	5.94e-04	1.13e-04	1.10e-04
50	0.0024	0.0012	3.75e-04	7.81e-04	6.91e-04	1.37e-04	1.66e-04
60	0.0011	4.36e-04	7.23e-04	5.59e-04	6.08e-04	2.06e-04	2.08e-04
70	9.75e-04	3.46e-04	5.26e-04	0.0031	3.12e-04	3.42e-04	2.70e-04
80	4e-04	2.21e-04	2.7e-04	0.035	4.93e-04	3.01e-04	2.75e-04

Table A.3: Standard deviation of methanol slip concentration measurements during the reformer characterization experiment. Values are reported for each combination of feed flow rate and reformer oil temperature.

Flow [ml/min]	200°C	210°C	220°C	230°C	240°C	250°C	260°C
10	1.08e-05	2.49e-05	1.31e-05	1.80e-06	1.59e-06	4.58e-08	1.95e-07
20	1.24e-05	2.97e-04	8.2e-06	3.02e-06	1.28e-06	1.54e-07	1.36e-07
30	4.04e-04	5.56e-05	2.90e-05	1.55e-05	7.37e-06	9.39e-07	2.81e-07
40	5.09e-04	3.06e-04	3.29e-05	7.78e-05	6.21e-06	5.24e-06	2.29e-07
50	6.39e-04	6.14e-04	2.54e-04	1.24e-04	1.29e-05	1.31e-05	9.79e-07
60	4.38e-04	2.45e-04	2.21e-04	1.58e-04	1.34e-05	4.39e-05	2.55e-06
70	5.26e-04	1.50e-04	1.91e-04	7.01e-04	1.13e-04	7.61e-05	5.13e-05
80	2.09e-04	1.35e-04	3.85e-04	8.41e-04	1.56e-05	7.60e-05	6.03e-05

Table A.4: Standard deviation of CO concentration measurements during the reformer characterization experiment. Values are reported for each combination of feed flow rate and reformer oil temperature.

Flow [ml/min]	200°C	210°C	220°C	230°C	240°C	250°C	260°C
10	5.44e-06	6.85e-05	7.06e-06	6.15e-05	2.44e-05	1.83e-05	6.35e-05
20	5.37e-06	8.42e-06	9.54e-06	1.24e-05	1.41e-05	7.45e-06	3.76e-05
30	6.10e-05	7.15e-06	6.16e-06	9.09e-06	2.27e-05	2.31e-05	2.01e-05
40	3.63e-05	2.30e-05	1.28e-05	3.48e-05	6.08e-05	2.02e-05	4.04e-05
50	1.86e-05	1.90e-05	1.82e-05	2.84e-05	5.58e-05	2.15e-05	2.01e-05
60	8.63e-06	5.91e-06	1.29e-05	2.48e-05	4.54e-05	2.98e-05	2.82e-05
70	5.45e-06	3.85e-06	5.93e-06	6.18e-04	1.70e-05	3.33e-05	3.39e-05
80	2.08e-06	2.52e-06	8.32e-06	3.03e-05	1.23e-05	3.70e-05	4.50e-05

Appendix B

Mid-Level Interface

This appendix provides an overview of the GUI and communication structure implemented in the mid-level control layer of the distributed test architecture. The mid-level interface, developed in LabVIEW, serves as the central coordination hub for the modular system, managing communication between the reformer module, fuel cell module, and the high-level EMS.

The interface enables real-time monitoring and control of key system parameters, including reformer oil temperature, evaporator temperature, feed flow rate, and gas composition control settings. It also facilitates the execution of startup and shutdown sequences, state transitions, and safety protocols such as communication loss detection and gas alarm handling.

The following figures illustrate the layout and functionality of the mid-level interface. These include detailed views of the control panel, system overview, and EMS interaction layer.

Figure B.1 shows the main control tab, where reformer control parameters can be manually adjusted, including those related to the gas composition control strategy used by the reformer test bench. To the right of the manual control section, several tabs allow for observation of the test bench. The active tab in this figure displays live measurements of all temperature sensors and the feed flow setpoint. Another tab (not shown) provides real-time reformate gas composition data.

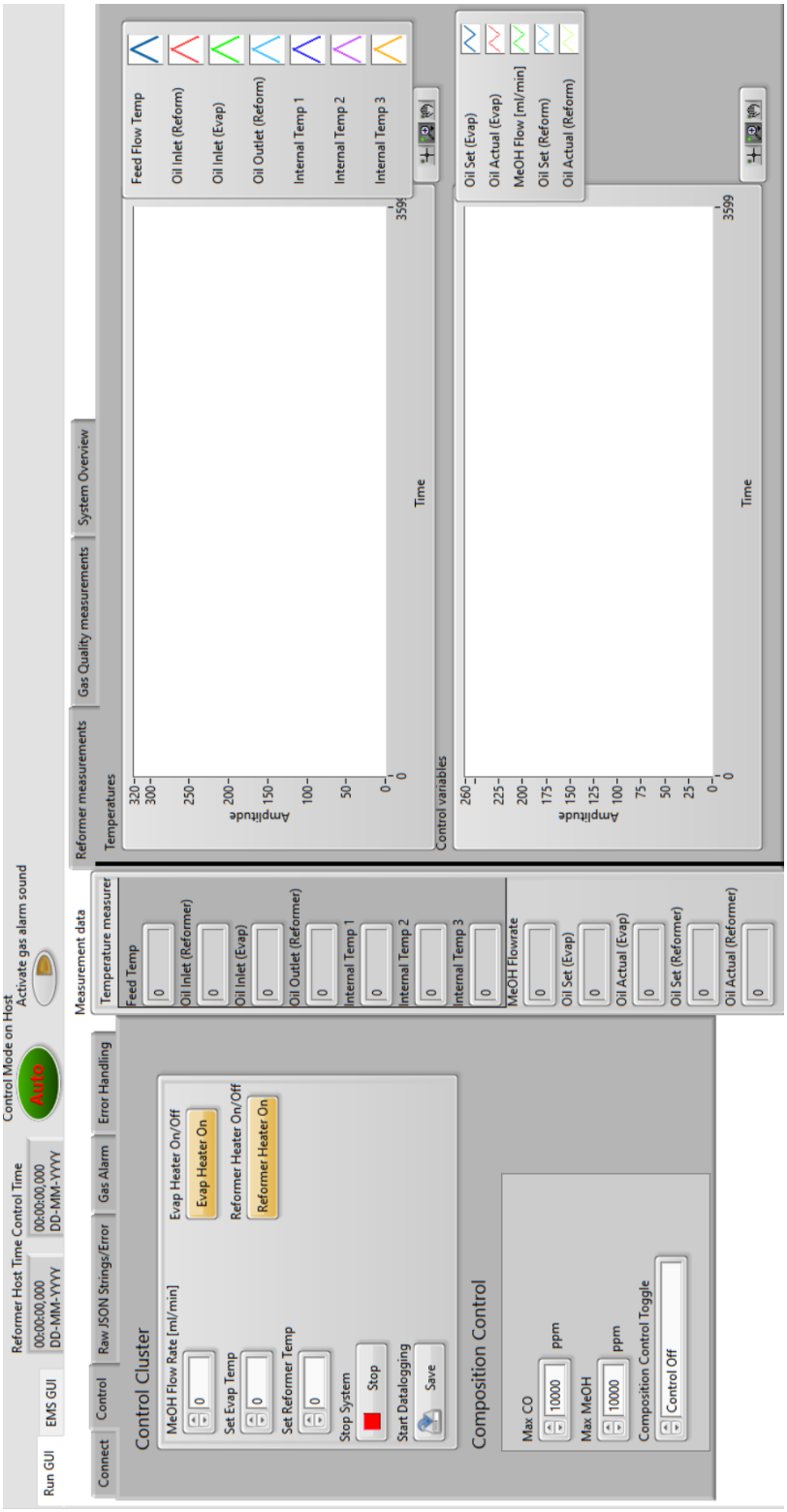

Figure B.1: Main control tab of the mid-level interface, showing manual control of reformer parameters and live temperature measurements.

Figure B.2 shows the same control section as Figure B.1, but with the system overview tab active. This view provides a schematic representation of the physical system, indicating where each measurement is taken, which helps contextualize the data shown in the control panel.

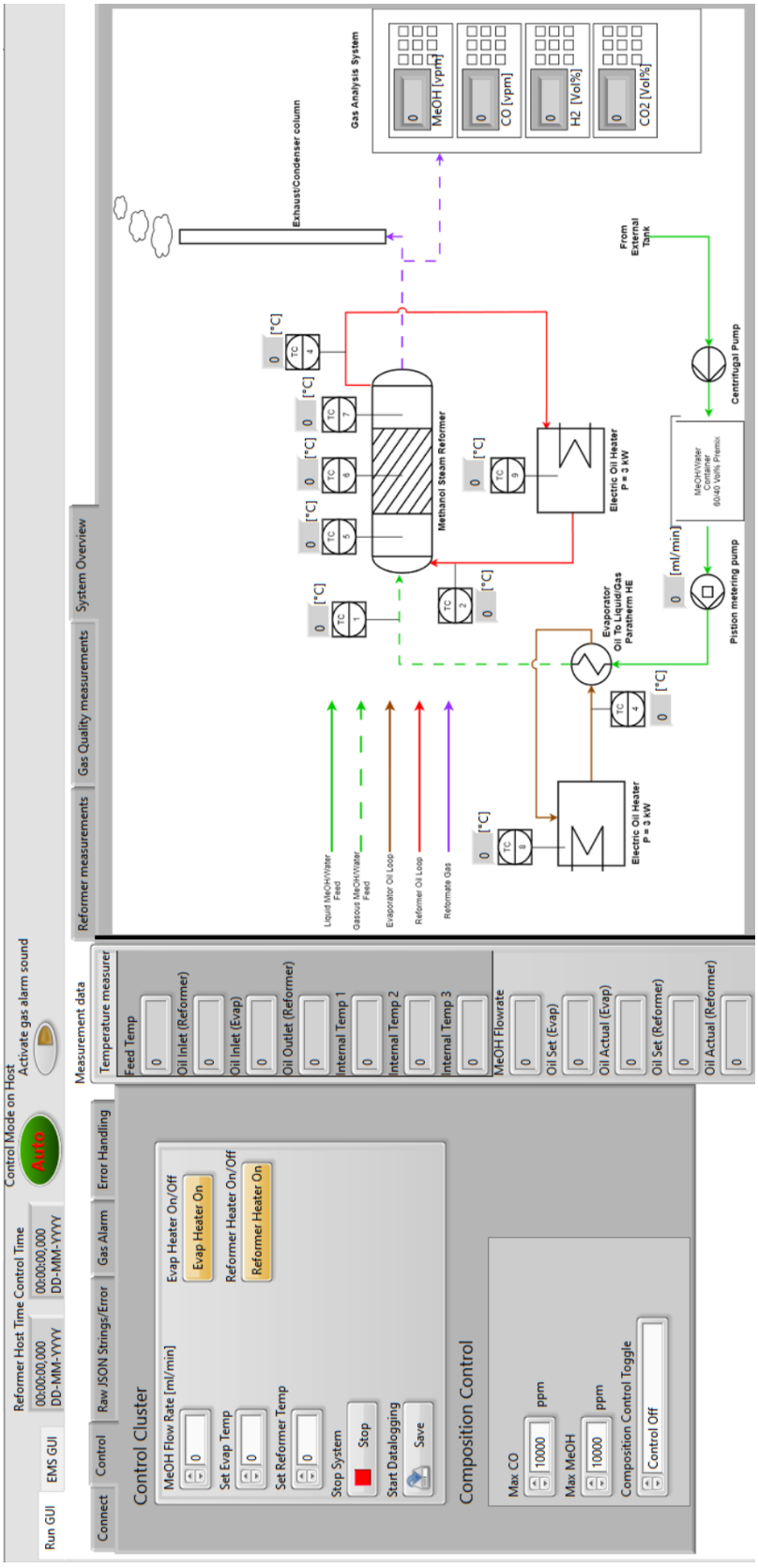

Figure B.2: System overview tab of the mid-level interface, showing the physical layout and sensor locations.

Figure B.3 displays the EMS control tab, which contains the parameters associated with EMS-based operation. This includes the On/Off signal, power reference, and heat demand

inputs. Additionally, it shows the values transmitted from the fuel cell module, such as current and voltage, as well as the temperature of the HWT.

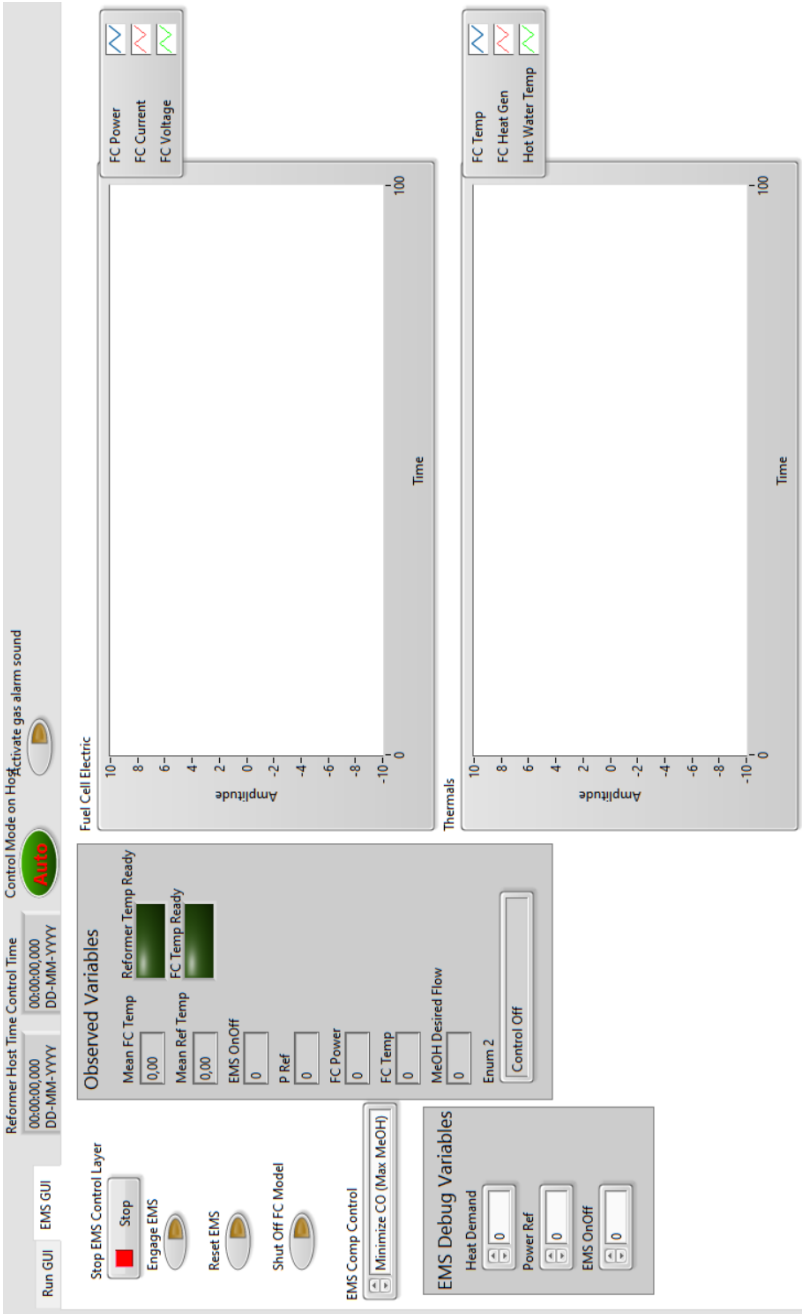

Figure B.3: EMS control tab of the mid-level interface, showing EMS parameters and real-time values from the fuel cell and hot water tank.

Appendix C

System Overview

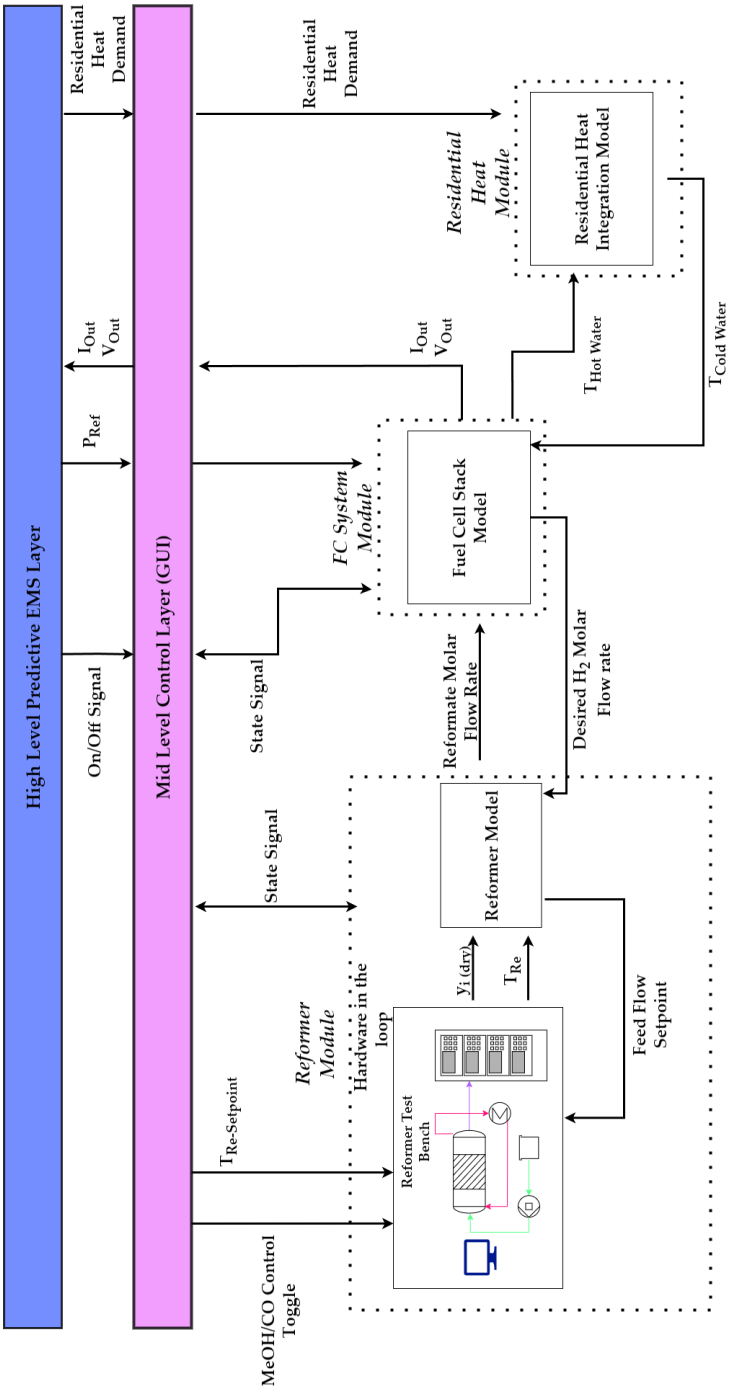

Figure C.1: Illustration of the communication lines between the modular systems and control levels.

Appendix D

Distributed Variables and Python Script

This appendix contains tables of all the variables transmitted and received by the different modules and mid-level layer.

Table D.1: Variables transmitted from the reformer test bench.

Variable Name	Description	Data Type
	Reformer Variables	
"MeOH Temp"	Feed Flow Temperature After Evaporator	float
"Oil Inlet Reform Temp"	Inlet Temperature for Reformer Oil Loop	float
"Oil Outlet Reform Temp"	Outlet Temperature for Reformer Oil Loop	float
"Oil Inlet Evap Temp"	Inlet Temperature for Evaporator Oil Loop	float
"Internal Temp 1"	Internal Reformer Catalyst Temperature 1	float
"Internal Temp 2"	Internal Reformer Catalyst Temperature 2	float
"Internal Temp 3"	Internal Reformer Catalyst Temperature 3	float
"Oil Evap Set Temp"	Setpoint Temperature for Evaporator Oil Loop	integer
"Oil Evap Actual Temp"	Measured Evaporator Oil Loop Temperature	float
"Methanol Flow Set"	Feed Pump Setpoint	integer
"Oil Reform Set Temp"	Setpoint Temperature for Reformer Oil Loop	integer
"Oil Reform Actual Temp"	Measured Reformer Oil Loop Temperature	float
"Lab Timestamp [UNIX]"	Timestamp in UNIX Format for Host	integer
"Control Mode"	Indicator for manual/Auto Control Mode on Host	bool
	Gas Analysis Unit	
"H2 [Vol%]"	Volume Fraction of Hydrogen in Reformate	float
"CO2 [Vol%]"	Volume Fraction of Carbon Dioxide in Reformate	float
"MeOH [ppm]"	Parts per Mill by Volume of Methanol	float
"CO [ppm]"	Parts per Mill by Volume of Carbon Monoxide	float
"GasQuali timestamp [UNIX]"	Timestamp in UNIX Format for Host	integer
	Gas Composition Results	
"T Minimize MeOH"	The Temp Setpoint Applied in Minimize MeOH Mode	integer
"T Minimize CO"	The Temp Setpoint Applied in Minimize CO Mode	integer
"Minimized CO Estimate"	Estimate of the CO in Minimize CO Mode	integer
"Minimized MeOH Estimate"	Estimate of the MeOH in Minimize MeOH Mode	integer
"Applied Toggle"	Indictor for Which Mode is Applied on System	integer
"Estimated MeOH"	Estimated MeOH in Minimize CO Mode	integer
"Estimated CO"	Estimated CO in Minimize MeOH Mode	integer
"Lab Timestamp [Unix]"	Timestamp in UNIX Format for Host	integer

Table D.2: Variables received by the reformer test bench from Mid-level layer

Variable Name	Description	Data Type
Reformer Control Variables Received		
"MeOH Flow Rate [ml/min]"	Control Variable for the Feed Flow Setpoint	integer
"Set Evap Temp"	Control Variable for the Evaporator Temperature	integer
"Set Reformer Temp"	Control Variable for the Reformer Temperature	integer
"Stop System"	Remote System Shutdown	bool
"Start Datalogging"	Activate Internal Datalog on cRIO System	bool
"Evap Heater On/Off"	On/Off Signal for Evaporator Oil Heater	bool
"Reformer Heater On/Off"	On/Off Signal for Reformer Oil Heater	bool
"Timestamp"	Control Signal Timestamp in UNIX	integer
Gas Composition Variables		
"Max CO_MeOH Mode"	Set Max CO in ppm when minimizing MeOH	integer
"Max MeOH_CO Mode"	Set Max MeOH in ppm when minimizing CO	integer
"Control Toggle"	Toggles between "Control Off [0]" "Minimizing MeOH [1]" "Minimizing CO [2]"	integer

Table D.3: Variables transmitted from the fuel cell module.

Variable Name	Description	Data Type
Transmitted From Fuel Cell Module		
"Fuel Cell Power [W]"	Electrical Power Generated From Fuel Cell Stack	float
"FC current [A]"	Fuel Cell Current	float
"FC total voltage [V]"	Fuel Cell Stack Voltage	float
"FC Power ref [W]"	Target Power From EMS Layer	float
"Heat generated [W]"	Heat generated by Fuel Cell Stack	float
"Fuel Cell Efficiency [-]"	Fuel Cell Stack Electrical Efficiency	float
"Flow rate of H_2[mol/s]"	Real-time Estimated Molar Flow rate of Hydrogen	float
"Required Flow rate of H_2[mol/s]"	Required Flow Rate of Hydrogen	float
"Fuel Cell Temperature [K]"	Homogenous Fuel Cell Temperature	float
"Oil Temperature FC inlet [K]"	Inlet Oil Temperature for Fuel Cell Stack	float
"Oil Temperature FC outlet [K]"	Outlet Oil Temperature For Fuel Cell Stack	float
"FC State [-]"	Fuel Cell Module Internal Logic 0 = Off 1 = Warmup 2 = Standby 3 = Operation 4 = Active Cooldown	float
"Timestamp"	Fuel Cell Module Timestamp in Unix	float

Table D.4: Variables exchanged between the EMS layer and the Mid-level layer

Variable Name	Description	Data Type
Transmitted by EMS Layer		
Pref	Target Power Desired From FC system	integer
onoff	On/Off signal 0 = off 1 = on	integer
Heat Demand	Household Heating Demand	integer
Received By EMS layer		
"FC current [A]"	Fuel Cell Current	float
"FC total Voltage [V]"	Fuel Cell Stack Voltage	float
"Hot Water Tank Temperature"	Temperature of Domestic Hot Water Tank	float

D.0.1 Python Data Logging

To facilitate synchronized data logging across all modules in the DTA, a custom Python script was developed. This script listens to multiple communication channels, buffers incoming messages by timestamp, and merges them once all relevant data has been received. The result is a single CSV log that captures the system state and control signals at each time step. The listing below shows the full implementation of this logging routine:

```
1
2
3  # -*- coding: utf-8 -*-
4  """
5  Created on Tue May 27 11:15:24 2025
6
7  @author: malte
8  """
9
10
11 import json
12 import pandas as pd
13 import *Redacted*
14 from datetime import datetime
15 import os
16
17
18 ALL_COLUMNS = [
19     "H2 [Vol%]","CO2 [Vol%]","MeOH [vpm]","CO [vpm]","GasQuali timestamp [
       UNIX]",
20     "MeOH Temp","Oil Inlet Reform Temp","Oil Inlet Evap Temp","Oil Outlet
       Reform Temp",
21     "Internal Temp 1","Internal Temp 2","Internal Temp 3","Oil Evap Set Temp"
       ,
22     "Oil Evap Actual Temp","Methanol Flow Set","Oil Reform Set Temp","Oil
       Reforn Actual Temp",
23     "Lab Timestamp [UNIX]","Control Mode","T Minimize MeOH","T Minimize CO",
24     "Minimized CO Estimate","Minimized MeOH Estimate","Applied Toggle","
       Estimated MeOH ",
25     "Estimated CO","OnOff FC","Operation State","Power Ref [W]","Heat Demand
       [W]",
26     "Shut Off FC Model","Timestamp [UNIX]","Ref Temp Ready","FC Temp Ready",
```

```
    "Max CO_MeOH Mode","Max MeOH_CO Mode","Comp_Control","Required MeOH flowrate [ml/min]",
    "Fuel Cell Temperature","Fuel Cell Power [W]","FC current [A]","FC total voltage [V]",
    "FC Power ref [W]","Heat Pump load [W]","Heat generated [W]",
    "Fuel Cell Efficiency [-]","Flowrate of Hydrogen [mol/s]",
    "Required Flowrate of Hydrogen [mol/s]","Oil Temperature FC inlet [K]",
    "Oil Temperature FC outlet [K]","Hot Water Tank Temperature [K]","FC state [-]",
    "Timestamp","Log Timestamp"
]

# Communication settings
BROKER_ADDRESS = *Redacted*
TOPIC_1 = "HYTEC4_1012/GasQuality"
TOPIC_2 = "HYTEC4_1012/Reformer_Data"
TOPIC_3 = "HYTEC4_1012/MinimizeResults"
TOPIC_4 = "HYTEC4_1012/MidLevel"
TOPIC_5 = "HYTEC4_1012/FC_Model_out"
SAVE_FOLDER = *Redacted*
CSV_FILENAME = "BonusTest3.csv"
CSV_FILE = os.path.join(SAVE_FOLDER, CSV_FILENAME)

# Buffers
buffer_topic1 = {}
buffer_topic2 = {}
buffer_topic3 = {}
buffer_topic4 = {}
buffer_topic5 = {}



def log_to_csv(data: dict):
    df = pd.DataFrame([data])
    file_exists = os.path.isfile(CSV_FILE)

    # Write header
    if not file_exists:
        empty_df = pd.DataFrame(columns=ALL_COLUMNS)
        empty_df.to_csv(CSV_FILE, mode='w', header=True, index=False)

    df.to_csv(CSV_FILE, mode='a', header=False, index=False)
    print(f"Logged at {data['Log Timestamp']}")
# Parse JSON
def parse_json_payload(raw_payload: bytes) -> dict:
    raw = raw_payload.decode(errors='ignore').strip()
    try:


        if raw.startswith('{') and raw.endswith('}'):
            return json.loads(raw)
        else:
            first = raw.find('{')
            last = raw.rfind('}') + 1
            return json.loads(raw[first:last])
    except json.JSONDecodeError as e:
        print(f"JSON error: {e} | Raw: {raw}")
        return None
```

```
# Messages
def on_message(client, userdata, msg):
    global buffer_topic1, buffer_topic2, buffer_topic3, buffer_topic4,
    buffer_topic5

    payload = parse_json_payload(msg.payload)
    if payload is None:
        return

    try:
        timestamp = None

        if msg.topic == TOPIC_1:
            timestamp = round(payload.get("GasQuali timestamp [UNIX]"))
            if timestamp:
                buffer_topic1[timestamp] = payload

        elif msg.topic == TOPIC_2:
            timestamp = round(payload.get("Lab Timestamp [UNIX]"))
            if timestamp:
                buffer_topic2[timestamp] = payload

        elif msg.topic == TOPIC_3:
            timestamp = round(payload.get("Lab Timestamp [UNIX]"))
            if timestamp:
                buffer_topic3[timestamp] = payload

        elif msg.topic == TOPIC_4:
            timestamp = round(payload.get("Timestamp [UNIX]"))
            if timestamp:
                buffer_topic4[timestamp] = payload

        elif msg.topic == TOPIC_5:
            timestamp = round(payload.get("Timestamp"))
            if timestamp:
                buffer_topic5[timestamp] = payload

        #find a common timestamp
        common_timestamps = (
            set(buffer_topic1) &
            set(buffer_topic2) &
            set(buffer_topic3) &
            set(buffer_topic4) &
            set(buffer_topic5)
        )

        for ts in sorted(common_timestamps):
            combined = {
                **buffer_topic1.pop(ts),
                **buffer_topic2.pop(ts),
                **buffer_topic3.pop(ts),
                **buffer_topic4.pop(ts),
                **buffer_topic5.pop(ts),
                "Log Timestamp": datetime.utcnow().isoformat()
            }
            log_to_csv(combined)
            return

```

```
139     except Exception as e:
140         print(f"Error processing message: {e}")
141 
142 # Server setup
143 client =*Redacteded*
144 client.on_message = on_message
145 client.connect(*Redacteded*)
146 client.subscribe([
147     (TOPIC_1, 0),
148     (TOPIC_2, 0),
149     (TOPIC_3, 0),
150     (TOPIC_4, 0),
151     (TOPIC_5, 0)
152 ])
153 
154 # Start the loop
155 print("logging started...")
156 client.loop_forever()
```

Listing D.1: Python script for logging reformer test bench data to CSV. Sensitive details redacted.